University of California
Santa Barbara

Experimental and Computational Exploration of Structure-Property Relationships in Perovskite-Derived Functional Materials

A dissertation submitted in partial satisfaction
of the requirements for the degree
Doctor of Philosophy
in
Materials

by

Emily Elizabeth Morgan

Committee in charge:

Professor Ram Seshadri, Chair
Professor Raphaële Clément
Professor Michael Chabinyc
Professor Anthony K. Cheetham

September 2023

The Dissertation of Emily Elizabeth Morgan is approved.

Professor Raphaële Clément

Professor Michael Chabinyc

Professor Anthony K. Cheetham

Professor Ram Seshadri, Committee Chair

July 2023

Experimental and Computational Exploration of Structure-Property Relationships in Perovskite-Derived Functional Materials

by

Emily Elizabeth Morgan

To my wonderful family and friends for their generosity and support.

Acknowledgements

I would like to take this opportunity to express my heartfelt gratitude towards my mentors who have been instrumental in my ability to complete my Ph.D. Their guidance, support, and encouragement throughout my time at UCSB have been invaluable, and I could not have made it to this point without them. First, I'd like to acknowledge my primary advisor, Professor Ram Seshadri. Ram has not only provided exceptional scientific guidance, but has also helped me to remain optimistic in the face of a pandemic and other challenges. I'd also like to thank him for prioritizing my professional development and investing many hours to help me with figures, posters, and presentations. I may have complained about it at the time, but he has taught me how to present my work clearly and with confidence and style. Although he is not formally my advisor, I also want to acknowledge Professor Tony Cheetham. I am extremely grateful for his willingness to sit down with me and critically examine diffraction patterns and spectra. His advice on writing has also pushed me to carefully consider how I communicate my research. Finally, I'd also like to thank my other committee members: Professor Michael Chabinyc and Professor Raphaële Clément. Whether it was troubleshooting equipment issues or providing guidance on data interpretation, Michael has always been willing to take time to help me. Raphaële has also been extremely generous with her time and has given me important feedback on my spectroscopy and computational work.

The work described in this dissertation also would not be possible without the hard work of the MRL staff and all the facility managers at UCSB. Thank you to Sylvia and Mary for help with logistics and purchasing, and to Dotti, Julie, and Frank for running outstanding outreach programs. Additionally, a big thanks to Fuzzy, Amanda, Rachel B., Youli, Rachel S., Tom, Jerry, and Jaya for keeping the computational and experimental facilities running smoothly.

Additionally, I want to thank my the collaborators and group members who have taught me so much about materials research. First, I would like to acknowledge Lingling and Pratap for getting me started with my first projects in the Seshadri group. They were both great mentors, and it's been amazing to see them start successful faculty careers (and even meet some of their graduate students!) Special thanks also to Sam and Justin for getting me started with DFT calculations. I never expected computation to be such a big part of my Ph.D., and I couldn't have done it without them. Finally, I'd like to express my gratitude for my collaborators at Northwestern, particularly Mercouri for his scientific insights and Shobhana for her enthusiasm and optical expertise.

Last but not least, I want to acknowledge all of my family and friends for supporting me through this process. I want to thank all of my running friends, especially Yuzki, Justin, and Emily F. Whether we were running Camino Cielo or just around Campus Point I've loved exploring Santa Barbara with you guys. Also, thanks to Gregg for being my buddy on the perovskites project, and to Arava for being a great role-model and collaborator. Of course, I have to thank Tofu and Goji for making me laugh every day. Thanks also to Evan for supporting me since the very beginning of our Ph. D. journey. I'm so excited for our next adventure together in the Bay Area. Finally, I'd especially like to thank my parents for always putting my education first and encouraging my love of science. From working on science fair projects to helping me move multiple times to pursue my research interests, you have been supportive every step of the way, and no words can express my gratitude.

Curriculum Vitæ

Emily Elizabeth Morgan

Education

Sep 2019 – Jul 2023 Ph.D. in Materials (expected)
University of California, Santa Barbara
Advisor: Professor Ram Seshadri

Aug 2015 – Dec 2018 B.A. in Chemistry, Minor in Mathematics
Washington University in St. Louis

Publications

12. **Morgan, E. E.**, Panuganti, S., Kent, G. T., Zohar, A., Brumberg, A., Mikhailovsky, A., Kanatzidis, M. G., Schaller, R. D., Cheetham, A. K., and Seshadri, R. "Understanding the Near-IR Luminescence of Molybdenum and Tungsten Oxyhalides," *In preparation.*
11. **Morgan, E. E.**,* Zohar, A.,* Lipkin, S., Monserrat, B., Vaidyanathan, S., Loeffler, D., Zhang, R., Schierle-Arndt, K., Cheetham, A. K., and Seshadri, R. "Screening Aluminum-Based Compounds as Low-κ Dielectrics for High-Frequency Applications," *Submitted to Chem. Mater.* *These authors contributed equally to this work.
10. **Morgan, E. E.**, Kent, G. T., Zohar, A., O'Dea, A., Wu, G., Cheetham, A. K., and Seshadri, R. "Inorganic and Hybrid Vacancy-Ordered Double Perovskites A_2WCl_6," *Chem. Mater.*
9. Kent, G. T., **Morgan, E. E.**, Albanese, K.R., Kallistova, A., Brumberg, A., Kautzsch, L., Wu, G., Vishnoi, P., Seshadri, R, and Cheetham, A. K. (2023) "Elusive Double Perovskite Iodides: Structural, Optical, and Magnetic Properties," *Angew. Chem. Int. Ed.*, 62: e2023060.
8. Chen, C., **Morgan, E. E.**, Liu, Y., Seshadri, R, and Mao, L. (2022) ""Breathing" Organic Cation to Stabilize Multiple Structures in Low-Dimensional Ge-, Sn-, and Pb-Based Hybrid Iodide Perovskites," *Inorg. Chem. Front.*, 9: 4892–4898.
7. Mao, L., **Morgan, E. E.**, Li, A., Kennard, R. K., Hong, M. J., Liu, Y., Dahlman, C. J., Labram, J. G., Chabinyc, M. L., and Seshadri, R. (2022) "Layered Hybrid Lead Iodide Perovskites with Short Interlayer Distances," *ACS Energy Lett.*, 7: 2801–2806.
6. Kennard, R. K., Dahlman, C. J., **Morgan, E. E.**, Wu, G., Chung, J., Cotts, B. L., Mikhailovsky, A., Mao, L., Kincaid, J., DeCrescent, R. A., Stone, K. H., Panuganti, S., Venkatesan, N. R., Mohtashami, Y., Assadi, S., Kanatzidis, M., Salleao, A.,

Schuller, J. A., Seshadri, R., and Chabinyc, M. L. (2022) “Enhancing and Extinguishing the Different Emission Features of Two-Dimensional $(EA_{1-x}FA_x)_4Pb_3Br_{10}$,” *Adv. Opt. Mater.*, 10: 2200547.

5. **Morgan, E. E.**, Evans, H., Pilar, K., Brown, C., Clément, R., Maezono, R., Seshadri, R., Monserrat, B., and Cheetham, A. K. (2022) “Lattice Dynamics in the NASICON $NaZr_2(PO_4)_3$ Solid Electrolyte From Temperature-Dependent Neutron Diffraction, NMR, and Ab Initio Computational Studies,” *Chem. Mater*, 34: 4029–4038.
4. Wang, S., **Morgan, E. E.**, Panuganti, S., Mao, L., Vishnoi, P., Wu, G., Liu, Q., Manatzidis, M. G., Schaller, R., and Seshadri, R. (2022) "Ligand Control of Structural Diversity in Luminescent Hybrid Copper (I) Iodides," *Chem. Mater.*, 34: 3206–3216.
3. Spanopoulos, I., Hader, I., Ke, W., Guo, P., Mozur, E., **Morgan, E. E.**, Wang, S., Zheng, D., Padgaonkar, S., Mamjunatha Readdy, G. N., Weiss, E., Hersam, M., Seshadri, R., Schaller, R., and Kanatzidis, M. G. (2021) "Tunable Broad Light Emission for 3D "Hollow" Bromide Perovskites Through Defect Engineering," *J. Am. Chem. Soc.*, 143: 7069–7080.
2. Wang, S., **Morgan, E. E.**, Vishnoi, R., Mao, L., Teicher, S. M. L., Wu, G., Liu, Q., Cheetham, A. K., and Seshadri, R. (2020) "Tunable Luminescence in Hybrid Cu(I) and Ag(I) Iodides," *Inorg. Chem.*, 59: 15487–15494.
1. **Morgan, E. E.**, Teicher, S. M. L., Wu, G., Mao, L., and Seshadri, R. (2020) "Tunable Perovskite-Derived Bismuth Halides: $Cs_3Bi_2(Cl_{1-x}I_x)_9$," *Inorg. Chem*, 59: 3387–3393.

Abstract

Experimental and Computational Exploration of Structure-Property Relationships in Perovskite-Derived Functional Materials

by

Emily Elizabeth Morgan

Over the past 100 years, the perovskite structure-type has become ubiquitous in materials science. Although the conventional perovskite structure is simple, it can accommodate many different combinations of ions, producing a wide range of functional materials. Additionally, even ions that cannot form a conventional perovskite can form perovskite-derived structures such as 2D layered perovskites, double perovskites, or ordered-vacancy perovskites. In order to tailor these materials to specific applications, it is critical to develop an understanding of how the chemical makeup and crystal structures of these materials impact their properties. Additionally, the role of different synthetic approaches cannot be overlooked. In this work, I will discuss work connecting structure with properties in several perovskite-derived systems, with a focus on three different applications. Specifically, I will emphasize the use of both experimental and computational techniques to understand the specific origins of the material properties of interest.

First, I will discuss a series of compounds with the overall formula $Cs_3Bi_2(Cl_{1-x}I_x)_9$. Interestingly, the compositions with a mixture of Cl and I take on a 2D ordered-vacancy perovskite structure which is distinct from the structures formed by the end members. Additionally, when synthesizing these compounds by solution-process methods, the products are unexpectedly iodine-rich compared to the initial stoichiometry of the re-

action. The origin of the driving force for I incorporation and effect on optoelectronic properties was studied by experiment and computation, and appears to be closely connected to the formation of the 2D structure-type.

Next, I introduce vacancy-ordered perovskite structures based on W and Mo. First, I discuss the air-free and anhydrous synthesis and characterization of compounds with the composition A_2WCl_6. These compounds show unusual temperature-dependent magnetism which suggests a need for a better theoretical understanding of d^2 magnetic ions. Additionally, I compare my materials with those reported in the literature which were synthesized by hydrothermal methods. The hydrothermal compounds have the formula $Cs_2MO_xX_{6-x}$, where *M* is Mo or W and *X* is Cl or Br. These compounds show exceptional near-IR luminescence, and the origin of this emission has been examined in detail.

Finally, I discuss a screening process for the identification of materials with low dielectric constants (κ). Computational estimates suggested that the compound $Al(HCOO)_3$, which has the ReO_3 structure-type, should have a favorable dielectric constant. However, experiments revealed that the true dielectric constant is larger than predicted. Explanations for the discrepancy between theory and experiment are discussed in order to further improve our guidelines for the identification of low-κ materials.

Contents

List of Figures

List of Tables

Chapter 1

Introduction

1.1 Perovskite-derived structures

The term "perovskite" originated in 1839 with the discovery of $CaTiO_3$, and the structure was first described in 1926 by Victor Goldschmidt. [1] Since then, this structure-type has become well-known and extensively-researched for giving rise to a number of functional materials. Much of the current interest in halide perovskites, which are the primary focus of this work, originates from their intriguing optoelectronic characteristics, with the best-known example being $CH_3NH_3PbI_3$ ($MAPbI_3$). Conventionally in these materials, the *A*-site is a large monovalent cation such as Cs^+ or $CH_3NH_3{}^+$ (MA), the *B*-site is a metal in the 2+ oxidation state, and the *X* site is a halide anion. These ions are arranged to form a network of BX_6 corner-sharing octahedra, where the *A*-site cations fill the cages created by each group of 4 octahedra. The prototypical structure, shown in Figure 1.1, is cubic, but these materials are prone to distortions which lead to room-temperature structures with lower symmetry.

The hybrid halide perovskites, in which the *A*-site is an organic cation, such as MA,

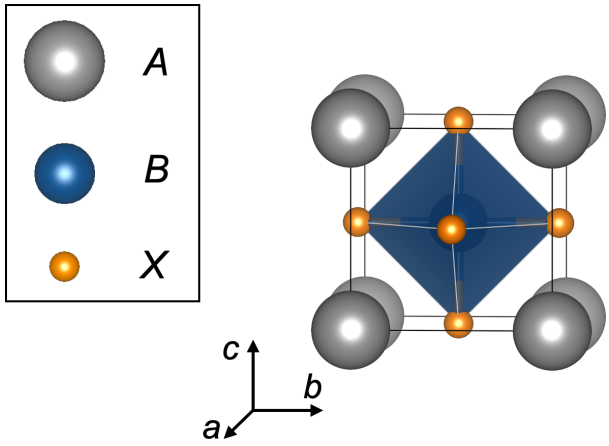

Figure 1.1: Crystal structure of the prototypical cubic perovskite.

were first reported by Weber in 1978. [2] However, for almost 30 years they were studied only for fundamental science reasons with no clear industrial applications. [3, 4] Research on these compounds accelerated when, in 2009, the first report was published on the use of $MAPbI_3$ and $MAPbBr_3$ as light-absorbing layers for photovoltaics. [5] Although the initial efficiency of these devices was low, this was a particularly exciting discovery because it suggested the possibility of producing cheap, flexible, and lightweight solar cells. Over the past 15 years, these materials have been extensively researched and optimized, with perovskite cells now achieving over 25% efficiency, and perovskite-Si tandem cells achieving over 30% efficiency. [6]

Due to the surge of interest in $MAPbI_3$ and related compounds, halide perovskites have now been studied both experimentally and computationally for many applications related to their tunable composition and optoelectronic properties, including photovoltaics, sensing, light-emission, gas storage, and photo-catalysis. [7] In this work, I will discuss materials which have been proposed for a number of these applications, including light absorption and emission and dielectric properties. Although these studies were in many ways inspired by the traditional 3D-connected structures like $MAPbI_3$, I will emphasize structures which do not have the conventional 3D perovskite struc-

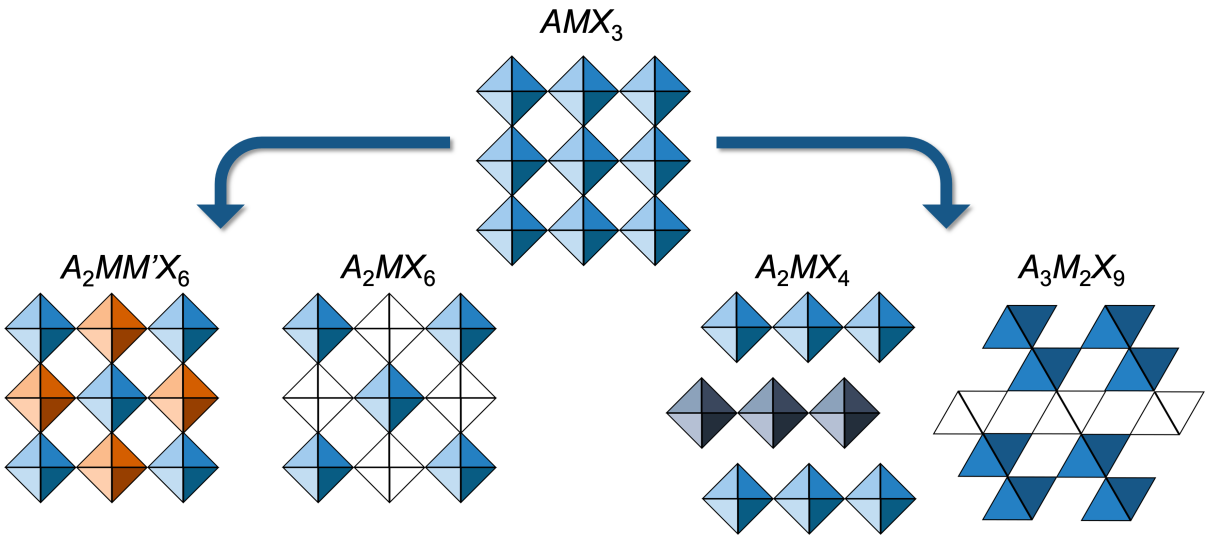

Figure 1.2: Schematic representation of some of the perovskite-derived structures discussed in this work. Adapted from the work of Vishnoi *et. al.* [8]

ture, but are instead perovskite-derived. Therefore, here I will give a brief summary of the requirements to form a perovskite structure, as well as the criteria for forming other structures related to perovskites. An overview of some of the perovskite-derived structures discussed in this work can be found in Figure 1.2.

One attractive aspect of the traditional perovskite crystal structure is that it is possible to predict which ions will form this structure using only geometric requirements based upon the radii of the ions. The well-known Goldschmidt tolerance factor for perovskite-formation is presented in Equation 1.1. [1] Here, r_A is the radius of the *A*-site cation, r_B is the radius of the *B*-site cation, and r_X is the radius of the *X*-site anion. The ideal value for the tolerance factor should be between 0.8 and 1.0. In addition to the tolerance factor, there is also the radius ratio requirement, which says that the ratio between r_B and r_X must be greater than $\sqrt{2} - 1$. Compositions that are close to the stability limits dictated by these equations will form either distorted perovskites or entirely different phases. Ionic radii can usually be obtained from the work of Shannon [9, 10], or in the case of organic cations, the work of Kieslich [11, 12], and the

combinations of ions which can form the ABX_3 structure can be predicted.

$$TF = \frac{r_A + r_X}{\sqrt{2}(r_B + r_X)} \tag{1.1}$$

By changing the stoichiometry or chemical composition of the conventional perovskite, a diverse range of perovskite-derived structures can be obtained. These include ReO_3-type structures, double perovskites, vacancy-ordered double perovskites, and 2D-layered perovskites. The ReO_3 structure-type can be viewed as an even simpler version of the perovskite, where the *A*-site cation has been removed. Here, the *B*-site can be a variety of transition metals, often in a 3+ or 6+ oxidation state. In the inorganic ReO_3 materials, the anion can be an single atom, such as O^{2-} or F^- or a polyatomic anion, such as OH^- or CN^-. Additionally, there are several examples of metal-organic framework (MOF) materials which have the ReO_3 structure-type. The simplest example of this are the metal formates, which have the general formula $M(HCOO)_3$, where *M* is Al, Fe, Ga, or In. [13] ReO_3 materials have been studied for many applications, including energy harvesting and storage, catalysis, and gas storage or separation. However, in this work I will examine the material $Al(HCOO)_3$, whose structure is shown in Figure 1.3, for an application that has not been considered until now: as a low-κ dielectric material. I will show that while $Al(HCOO)_3$ has all of the qualities of a "good" low-κ material in theory, its performance in experiment is less promising. The reason for this behavior is explored computationally and likely arises from the types of vibrations available to atoms in this structure.

Another variation on the traditional perovskite structure is the double perovskite, where the structure is formed by having two alternating *B*-site ions with oxidation states of 1+ and 3+. These two *B*-sites can be chemically distinct, as in the case of

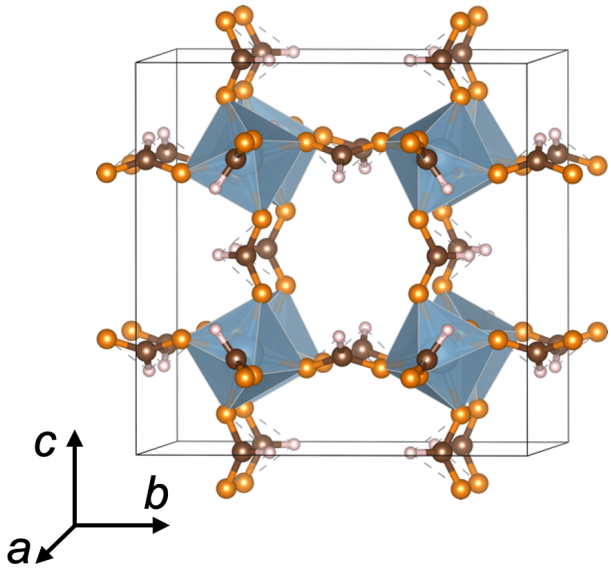

Figure 1.3: Crystal structure of $Al(HCOO)_3$.

$Cs_2AgBiBr_6$, or have the same element in two different oxidation states, as in the case of $Cs_2Au^{I}Au^{III}Cl_6$. [14] While there are many reported fluorides and chlorides for this structure-type, there are relatively few bromides and iodides. Recent work in our group has revealed that this is largely due to the fact that ions which are large enough to stabilize the iodide double perovskites are often very air-sensitive, making characterization of these phases challenging. [15] In spite of this, we have successfully synthesized and characterized a few examples of this class of compounds. [16] As in the case of the conventional perovskite, these materials have been studied since the early 1900s; however, recent research interest has been largely driven by the goal of identifying materials with optical properties similar to $MAPbI_3$ but with improved stability. While there has been somewhat limited success in achieving this goal, research in this area has identified several other interesting functional materials with potential applications in sensing and light emission. [17]

In addition to double perovskites with two distinct *B*-site ions, there is another class of materials in which the second *B*-site is vacant. Known as the K_2PtCl_6 structure, or

vacancy-ordered double perovskite, these materials contain isolated $[BX_6]^{2-}$ octahedra, where the *B*-site is a metal in the 4+ oxidation state. The best known compounds of this type are Cs_2SnI_6 and Cs_2TeI_6 due to their interesting optoelectronic properties, but there are many combinations of ions which can form this structure-type. [18, 19] These compounds are particularly interesting to study because they represent an intermediate between 0D molecular complexes, such as those studied in solution-state inorganic chemistry, and the conventional 3D perovskites. [14] Therefore, many of their properties can be systematically manipulated through an understanding of simple molecular-orbital diagrams. In this work, I will describe work on the compounds A_2MoX_6 and A_2WX_6. In contrast to some of the other vacancy-ordered systems referenced here, there remains a poor understanding of these compounds in the literature, with different sources reporting experimental observations which are not easily explained or conflicting information about material properties. Some of these reports are especially notable because they claim that these compounds show unexpected properties, such as near-IR luminescence [20] and topological surface states. [21] Therefore, I have attempted to clarify both the structure and properties of the A_2WCl_6 compounds, and I highlight the features which distinguish them from the related oxyhalide compounds such as $Cs_2WO_xCl_{6-x}$. Figure 1.4 demonstrates the differences in crystal structures and composition for these two types of compounds. In the case of the molybdenum compounds, I show that there seem to be no reliable reports of compounds with the formula Cs_2MoCl_6. Instead, all reported syntheses lead to compounds with the formula $Cs_2MoO_xCl_{6-x}$. However, these oxygen-containing species do show notable near-IR luminescence which will be an important area for future study.

The final class of perovskite-derived materials that I will briefly discuss here are the 2D layered perovskites. Inorganic layered oxide perovskites have long been studied,

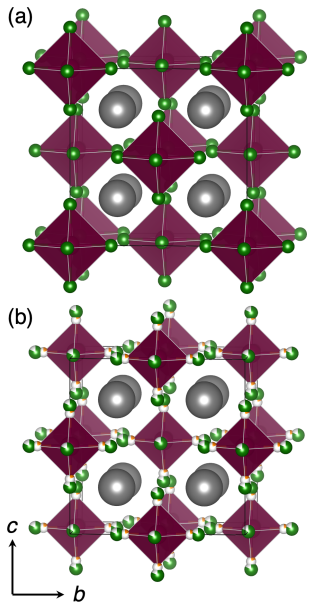

Figure 1.4: Crystal structures of (a) Cs_2WCl_6 and (b) $Cs_2WO_xCl_{6-x}$

but following the discovery of high-temperature superconductivity in the cuprates, [22] there was a renewed interest in the structure and properties of these layered materials. This led to the first reports of 2D hybrid organic-inorganic perovskites in the 1980s and 90s. [23–25] The two most commonly-studied categories of the 2D layered perovskites are the Ruddlesden–Popper and Dion–Jacobson phases, which have the compositions $A'_2A_{n-1}B_nX_{3n+1}$ and $A'A_{n-1}B_nX_{3n+1}$, respectively, where n refers to the number of layers of BX_6 octahedra in each inorganic "slab". In these structures, generally a small organic cation such as MA serves as the *A*-site cation within the inorganic layers (for the case of $n \geq 2$), while a larger organic cation, such as butylammonium, will serve as the *A*' "spacer" cation in between the layers. Similarly to the 3D structures, these compounds are semiconducting with interesting phase transitions and structure-property relationships. [26, 27] However, in contrast to the 3D structures, the properties of the layered perovskites are strongly anisotropic due to the insulating organic cations in between each inorganic layer. Additionally, as a result of quantum-confinement, the optoelec-

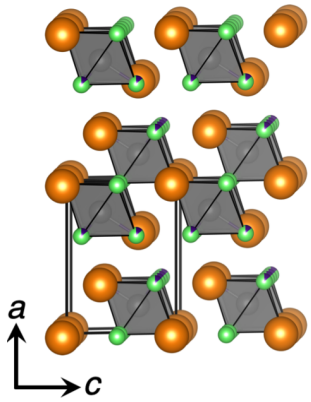

Figure 1.5: Crystal structure of $Cs_3Bi_2(Cl_{1-x}I_x)_9$.

tronic properties of these compounds can be tuned by selecting the value of n. Finally, many of the 2D phases show improved stability compared to the 3D structures, and there are a much greater variety of cations which can form the 2D structures, making this a rich area of study. [28] It is also possible to further manipulate the composition of the 2D perovskites to produce layered double perovskites, allowing for further manipulation of optical and magnetic properties. [29]

Work in our group has primarily investigated the structure and optoelectronic properties of the Pb-, Bi-, Sn-, and Ge-based versions of the layered hybrid halide perovskites. More specifically, we have shown how different synthesis routes can tune the optical properties of these compounds [30] and how the selection of organic cations can template interesting structural motifs. [31, 32] These studies will not be discussed in detail in this work, but they provide good examples of how small changes in the structure of these compounds can be used to manipulate their properties. In this document, I will focus on compounds with the composition of $Cs_3Bi_2(Cl_{1-x}I_x)_9$. The structure of this compound, shown in Figure 1.5, is interesting because it is an example of an all-inorganic layered halide perovskite in which the Cs^+ cations are both within and between the layers of BiX_6 octahedra. However, this series of compounds does

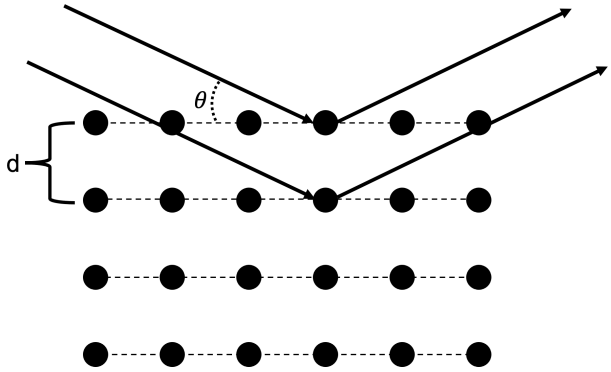

Figure 1.6: Schematic representation of the geometric criteria for constructive interference, as described by Bragg's Law.

not have the typical stoichiometry of other layered halide perovskites because it has ordered vacancies of Bi atoms, giving the structure a "corrugated" appearance. While these compounds do not have suitable properties to serve as solar materials, they provide an interesting case study for how DFT and experiment can be used to understand the roles of structure and composition in material properties.

1.2 Diffraction techniques

Given that this work primarily focuses on material characterization through a number of experimental and computational methods, it is important to address the basic principles of these techniques and the motivation for using them. The first, and probably most-commonly used, technique is diffraction, which is used to probe long-range order in crystalline materials. In this thesis, I will discuss crystal structures which have been determined using a variety of diffraction techniques, including lab powder X-ray diffraction (XRD), synchrotron XRD, single-crystal XRD, and neutron diffraction. Although each of these techniques follows the same basic principles, each has its own advantages and drawbacks, which will be discussed here.

All diffraction-based techniques are fundamentally based on Bragg's Law, which is shown in Equation 1.2. This equation gives the condition for constructive interference for a beam with a wavelength of λ incident upon a crystalline lattice. Here, d is the distance between planes of atoms, θ is the angle between the incident beam and the plane of atoms, and n is an integer, as shown in Figure 1.6. Additionally, for a successful diffraction experiment, the wavelength of the incident beam must be of a similar magnitude to the spacings between atoms in order to observe diffraction. For each combination of d and θ where this condition is satisfied, there will be constructive interference, and therefore a peak in the intensity of the diffracted beam will be measured. When this condition is not satisfied, then destructive interference will occur and no intensity will be measured. It is important to note here that in this work I only discuss diffraction using elastic scattering, where λ is constant. For the lab-based X-ray diffraction discussed here, the wavelengths used are Cu Kα (λ = 1.5406 Å) for powders and Mo Kα (λ = 0.7093 Å) for single crystals. For synchrotron X-ray diffraction experiments, the wavelength of radiation used at 11-BM can vary between 0.34 and 1 Å, but the data in this thesis were collected with λ = 0.458933 Å. Similarly, for neutron sources, neutrons of different wavelengths may be available, but here the wavelength was 1.540 Å.

$$n\lambda = 2dsin(\theta) \tag{1.2}$$

In a powder experiment, it is assumed that the sample is made up of many randomly-oriented crystallites, where the size of these crystallites should be much smaller than the size of the overall sample. Whether the radiation is from a lab source, synchrotron, or neutron source, the results of a diffraction experiment are visualized as a plot of counts vs. 2θ or Q, where $Q = \frac{4\pi sin(\theta)}{\lambda} = \frac{2\pi}{d}$. Although 2θ is the most common axis

used in plotting software, Q is useful because it allows for comparison of diffraction patterns obtained with different wavelengths of radiation. The location and intensity of peaks in diffraction experiments is determined by the structure factor, which is shown in Equation 1.3. In this equation, f is the scattering factor and x, y, and z are the coordinates for the j^{th} atom, while (hkl) refers to a reciprocal lattice point. This equation tells us that the locations of the peaks in a diffraction pattern will be determined by the size and symmetry of the unit cell, while the peak intensities will be determined by the identity of the atoms. Using this equation, it is possible to take powder diffraction data and fit the peak intensities and locations to a structural model using either Pawley, [33] Le Bail, [34] or Rietveld analysis [35] in a software package such as TOPAS. [36] An example of a pXRD pattern and a Rietveld refinement of the data is shown in Figure 1.7. The major difference here is that in a Pawley or Le Bail fit, only the size and symmetry of the unit cell are modeled, while in a Rietveld fit it is possible to determine atomic positions and identities. Fitting software can also be used to account for instrument parameters, particle size and strain effects, and other types of defects which cause deviations from ideal crystallinity. Often a useful strategy is to first perform a Pawley or Le Bail refinement to verify the spacegroup and determine the lattice parameters and an appropriate peak shape. After those parameters have been refined, they can be kept constant in a Rietveld analysis. Additionally, a number of resources are available in the literature which provide guidance for the use and interpretation of these refinement methods. [37, 38]

$$F_{hkl} = \sum_{j=1}^{N} f_j e^{[-2\pi i(hx_j + ky_j + lz_j)]} \tag{1.3}$$

As the name implies, in a single-crystal experiment, the sample is a single crystal, usually with a size on the micron scale. In this experiment, the sample itself must be

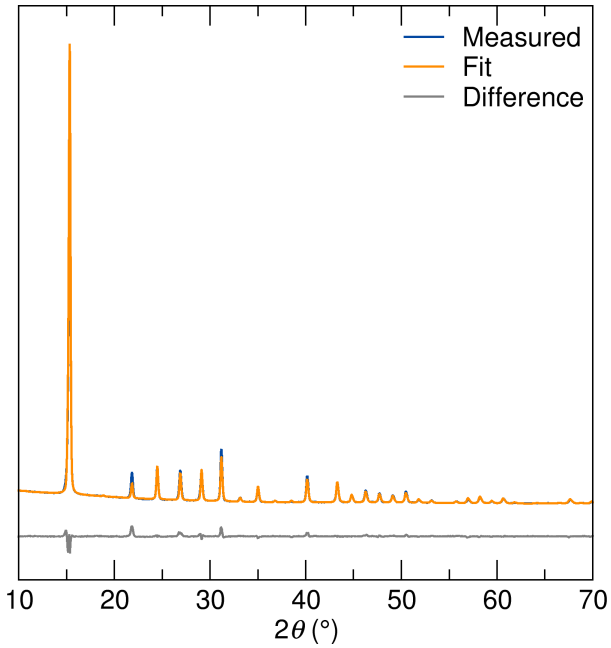

Figure 1.7: Example lab pXRD pattern and associated Rietveld refinement for $Al(HCOO)_3$.

rotated with respect to the X-ray source and detector in order to probe all the atomic planes. In this case, the resulting data is a series of images which show the diffraction intensity at various points in reciprocal space. Software is then used to process these images to form a 3D "map" of electron density which can be used to determine the structure of the crystal. The single crystal refinements discussed in this thesis were performed using the GSAS [39] and SHELXTL softwares and were done by Dr. Lingling Mao, Dr. Guang Wu, and Dr. Greggory Kent.

To conclude this section, I will provide a brief discussion of the advantages and disadvantages of the various diffraction techniques presented here. Laboratory powder X-ray diffraction is the most commonly-used technique due to the simplicity of the experiment. While lab XRD is often used simply for phase matching or identification and assessing the purity of a sample, it is also possible to use the data for Pawley or Rietveld refinements in order to gain insights into sample structure and composition.

For example, in Chapter 2, Rietveld analysis of lab pXRD data is used to show that samples were phase-pure and to correlate changes in composition with changes in the lattice parameter of the compounds. However, in this study the lab XRD data was not of sufficient quality in order to directly refine the site occupancies in the structure. Instead, the occupancies were inferred using the lattice parameters and other experimental techniques. In order to directly determine the composition for these compounds, synchrotron data would have been preferable.

In a synchrotron XRD experiment, the main disadvantage is that time and planning are required to send samples to a synchrotron source, such as 11-BM at Argonne National Lab. Another complication is that highly air- or water-sensitive samples may decompose during shipping or measurement, as the polyimide capillaries used as sample holders are permeable to air over extended time periods. However, there are also numerous advantages to conducting synchrotron experiments. The primary advantages are the high flux and collimation of the X-ray source, the tunability of the X-ray wavelength, and the ability to select from a wide range of temperatures for each experiment. As a result, data with high signal-to-noise and resolution can be obtained quickly over a large Q range at a synchrotron. Additionally, more sophisticated experiments can be performed where the wavelength of radiation is varied in order to give information about the location of various elements in the crystal structure. [40] This higher-quality data makes it possible to perform more detailed refinements, including the determination of site occupancies and atomic displacement parameters (ADPs), which can give important insights into the structure and composition of materials.

Neutron diffraction is generally considered a complementary technique to synchrotron diffraction, and it can be performed either at a nuclear reactor or spallation source. The utility of neutron diffraction data is exemplified here by the study of

$NaZr_2(PO_4)_3$ in Appendix A, where variable temperature neutron diffraction was used to determine lattice parameters, atomic positions, and anisotropic ADPs with high precision. In neutron diffraction, the basic principles of the technique are similar to XRD; however, while X-rays interact with the electrons surrounding each atom, neutrons interact with the atomic nuclei. Therefore, while the scattering strength of an atom in XRD is proportional to its atomic number, in neutron diffraction this is not the case. Instead, the scattering strength of various elements appears almost random throughout the periodic table, which makes this technique especially suitable for probing some low-atomic-number nuclei. A related phenomenon is that in neutron diffraction, the scattering intensity does not have the same Q dependence as in X-ray diffraction, where scattering decreases quickly at higher Q. Therefore, in neutron diffraction it is possible to obtain high quality data over a larger Q range. [40] This was particularly important in the diffraction work and refinements presented here (performed by Dr. Hayden Evans), as it allowed us to determine the atomic positions and ADPs of atoms with fairly low atomic numbers. For this set of experiments, the only disadvantage to neutron diffraction was that a large mass of high-purity sample was required. Additional complications in neutron diffraction can also arise if a sample contains elements which either absorb neutrons strongly or have very little neutron scattering.

Finally, we can consider the advantages of single-crystal X-ray diffraction, which is an especially important technique in the field of hybrid halide perovskites. The main advantage of single crystal diffraction is that it allows the structure of the material to be determined even if little information is known initially about its symmetry and structure. This is especially important for the halide perovskites which are lower in symmetry and therefore have complicated powder diffraction patterns. In these cases, it can be challenging to determine the crystal structure from powder diffraction with-

out an initial model. Additionally, as long as the sample is of high quality, single-crystal diffraction allows the determination of symmetry, lattice parameters, atomic positions, occupancies, and ADPs with small uncertainties. Single crystal diffraction was particularly important for the contents of Chapters 2, 3, and 4, where it was important to precisely determine the occupancies of certain atomic positions in order to know the overall composition of the compounds of interest. For this technique, the most challenging aspect is to obtain crystals which are of suitable quality. For many halide perovskites, good quality crystals can be obtained from hydrothermal synthesis in acid solutions. However, if the desired compound is not compatible with these conditions, then it is necessary to experiment with different temperatures and solvents to produce a good sample. Additionally, for compounds not soluble in organic solvents, it is also possible to grow crystals using a solid-state vapor transport method. [16]

In conclusion, diffraction is one of the most routine and important tools for determining the structure and composition of a material. While all of the techniques here share the same underlying physical principles, each has its own distinct advantages and disadvantages. For example, for many of the inorganic perovskites discussed here, powder XRD, either in the lab or at a synchrotron, is often sufficient. However, for some perovskites, such as those discussed in Chapters 3 and 4, as well as many hybrid halides, single-crystal XRD can provide the most straightforward method for structure determination. Finally, in some specific cases where large amounts of sample are available, neutron diffraction can serve as a complementary technique to provide information that may not be accessible using X-ray methods.

1.3 Spectroscopic techniques

In addition to diffraction, the other most important experiments discussed in this thesis are spectroscopy-based. As in diffraction, spectroscopy gives us access to information about the structure, composition, and sometimes dynamics in a compound. However, rather than probing the physical location of atoms, spectroscopy probes the electronic and vibronic energy levels available in atoms of interest. In this thesis, some relevant techniques are X-ray spectroscopy, Raman spectroscopy, UV-vis and photoluminescence measurements, and nuclear magnetic resonance (NMR) spectroscopy.

The first two techniques I will present are X-ray fluorescence (XRF) spectroscopy and X-ray photoelectron spectroscopy (XPS). Both of these techniques are often used to provide compositional information, but use different physical mechanisms and have distinct advantages. In XRF, the sample is exposed to high-energy X-rays which have sufficient energy to eject core electrons from the sample. When these electrons are ejected, higher-energy electrons within the sample will release energy in order to move to the lower-energy state that was left empty by the ejected electrons. The energy that is released (also in the form of X-rays) is detected by the instrument. Since each element has a characteristic electronic configuration, each will be associated with different patterns in the energies of the radiation emitted. Therefore, by measuring the intensity of the radiation emitted at different energies, the composition of the sample can be inferred. When using this technique, there are a number of important factors to keep in mind in order to get reliable results. The first aspect to consider is that most instruments have both “quantitative” and “qualitative” modes. The first is what is often used in industrial settings and requires measuring a number of samples with known compositions in order to establish a calibration curve for highly accurate analysis. The second mode is used either to validate whether an element is present in a sample, or in an ex-

perimental setting where there are no reference samples available. In the "qualitative" mode, it is still possible to obtain accurate compositions, but this mode is primarily useful in cases where a comparison between similar samples is desired. Furthermore, in this mode it is very important to ensure that the energy of the radiation that you plan to measure for a given element does not overlap with that of another element present. Finally, sample composition should ideally be verified by making multiple measurements of the same composition and by using XRF in combination with other experimental techniques.

Similarly to XRF, XPS also involves exposing the sample to X-rays which eject electrons from the sample. However, rather than measuring the radiation emitted by the sample, in XPS the ejected electrons themselves are measured, as illustrated in Figure 1.8. Using the principle of the photoelectric effect, the measured kinetic energy of the electrons can then be used to determine the binding energy of those electrons. This binding energy is directly determined by the element and orbital where the electron originated. Therefore, by monitoring the number of electrons with specific binding energies, the composition of a compound can be determined. Additionally, using high-resolution XPS spectra, different oxidation states and bonding environments can be identified. This detailed information gives XPS certain advantages over XRF; however, XPS data also requires more detailed modeling, as shown in Figure 1.9, and requires samples to be measured in an ultra-high vacuum environment, making these experiments more time-consuming than XRF. XPS is also a highly surface-sensitive technique. Therefore, compositional analysis results can be skewed by a contaminated or non-homogeneous surface. In summary, both XRF and XPS can give information about the composition of samples. However, the choice of technique is based on the type of information desired as well as the number and types of samples to be measured.

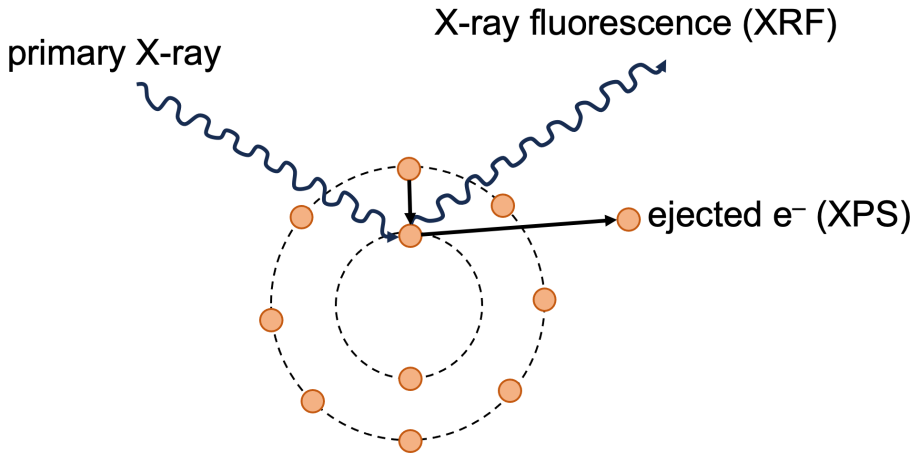

Figure 1.8: Illustration showing the difference between the measurements performed in XRF (radiation detection) and XPS (electron kinetic energy detection).

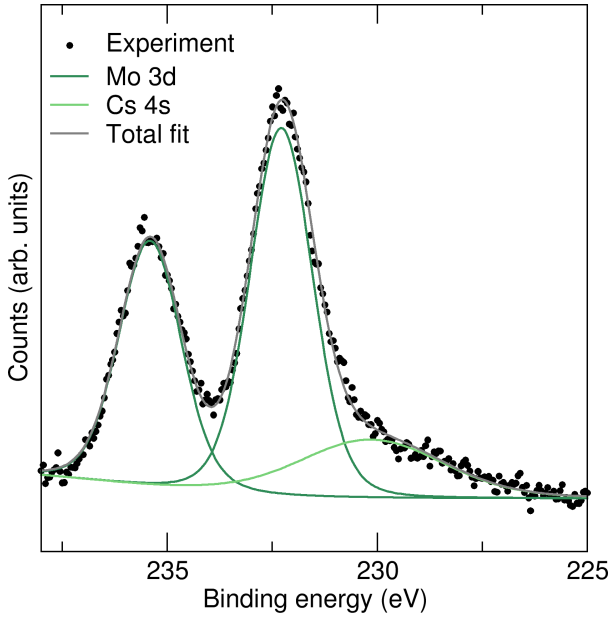

Figure 1.9: Example high-resolution XPS spectrum of $Cs_2MoO_xCl_{6-x}$ and associated modeling of the Mo $3d$ and Cs $4s$ peaks.

The next experimental technique I will introduce is Raman scattering, which is used to probe the vibrations of atoms within a crystal structure. This technique is particularly useful because it can be used to probe bonding in many different types of samples. Additionally, as discussed in Chapter 4, it is possible to perform variable temperature measurements which allow for the detection of phase transitions or other changes in the dynamics of a sample. Raman scattering is an inelastic process in which the sample is exposed to monochromatic light (generally a laser source in the visible range). In most cases, light is elastically scattered by the sample, meaning that no energy is absorbed by the sample. However, in some cases, energy will be absorbed by the sample, so that the light that is re-emitted and detected by the instrument has a slightly different energy than the incident light. The difference in the energies is known as the Raman shift and corresponds to the energy of a vibrational mode. For a given sample, there may be many different vibrational modes possible, each of which will have their own Raman shift, leading to peaks at different energy values in the spectrum. The vibrational modes that can be detected in a Raman experiment are those which lead to a change in the polarizability of the structure. Therefore, symmetry analyses can be used to predict the number of Raman-active modes. In structures that are relatively simple, like the vacancy-ordered perovskite, the number of peaks that are expected in the Raman spectrum can be predicted by a simple group-theoretical analysis. In the case of more complex structures, the Bilbao Crystallographic Server's "Spectral Active Modes" (SAM) tool [41–43] can be helpful for prediction of Raman spectra. Furthermore, DFT-based calculations can provide more detailed information about peak intensities and locations. In summary, Raman spectroscopy can give detailed information about bonding in many different types of materials, especially when accompanied by the use of computational tools and comparison with the structures of known materials.

In addition to clarifying the structure and composition of a material, spectroscopy can also tell us about its electronic properties. The most common experiment to determine the electronic transitions in a compound is UV-vis spectroscopy. For samples that are in a solution or thin-film, these measurements can be performed in a transmission geometry, where light passes through the sample, and the intensity of the transmitted light is compared to the intensity of the incident light. In these experiments, the source is a white-light source, and the wavelength of the incident light is selected by a monochromator. For wavelengths of light that correspond to the energy of an electronic transition in the sample, the sample will absorb light, leading to a decrease in the intensity of the transmitted light. For solution-state samples, transmittance versus wavelength data can be converted to absorbance versus wavelength using the Beer-Lambert Law. In solid-state samples, the situation is more complex, because most experiments are performed in a reflectance geometry, where the material of interest is embedded in an inert matrix such as barium sulfate. In this type of experiment, the reflectance is measured as a function of wavelength and referenced against a sample which contains only the matrix material and the sample holder. In order to convert the measured reflectance data to absorbance, the Kubelka-Munk transformation [44] is often used. This equation was originally developed to describe the absorbance of pigments in paints, but due to its simplicity it has become the standard method for interpreting reflectance data. A typical application of these measurements is to determine the bandgap of a material, as discussed in Chapter 2, but it can also be used to identify other electronic transitions. In order to obtain accurate results from solid-state measurements, it is important to ensure that sample preparation and data processing are done in a consistent manner across samples. Additionally, to account for the effects of dispersing the sample in the matrix material, it is often a good idea to prepare samples with different concentrations of the material diluted in the matrix.

A related technique to UV-vis spectroscopy is fluorimetry and other photoluminescence measurements. Generally, UV-vis spectra will be collected first to identify at which energies a material will absorb light. Next, in a fluorimetry experiment, the material is excited with those wavelengths of interest, while detecting re-emitted light at different wavelengths. Similarly to the UV-vis experiment, for solid-state samples this measurement must be done in a reflectance geometry. Additionally, if a material is known to emit light of certain energies, the excitation energy can be tuned to systematically determine which absorption transitions produce specific features in the emission. These experiments are especially common in the hybrid halide perovskites, where materials often absorb and emit light in the visible range. In the case of the oxyhalides described in Chapters 3 and 4, the materials absorb in the visible range but emit in the near-IR. Therefore, the majority of experiments described used a laser source and CCD detector. The use of a laser is also advantageous because it allows for the collection of time-resolved data. In these experiments, rather than continuously exciting the sample, a pulsed excitation is used, and the intensity of emission is monitored over time. By modeling this data with an exponential decay function, the emission lifetime can be determined, which can help to clarify the mechanism of emission.

The final experimental method that I will introduce in this section is NMR spectroscopy. In its most basic form, NMR involves the investigation of the environment surrounding nuclei of interest by determining the relative shielding effects of the electrons on the nuclei, as well as coupling interactions (namely the dipolar and J couplings, and in some cases quadrupolar coupling). Samples are placed in an external magnetic field, the nuclear spins are excited using radio-frequency (RF) radiation, and then the NMR signal is measured over a period of time. This time-domain signal, called the free-induction decay (FID), is converted to a frequency-domain spectrum by Fourier

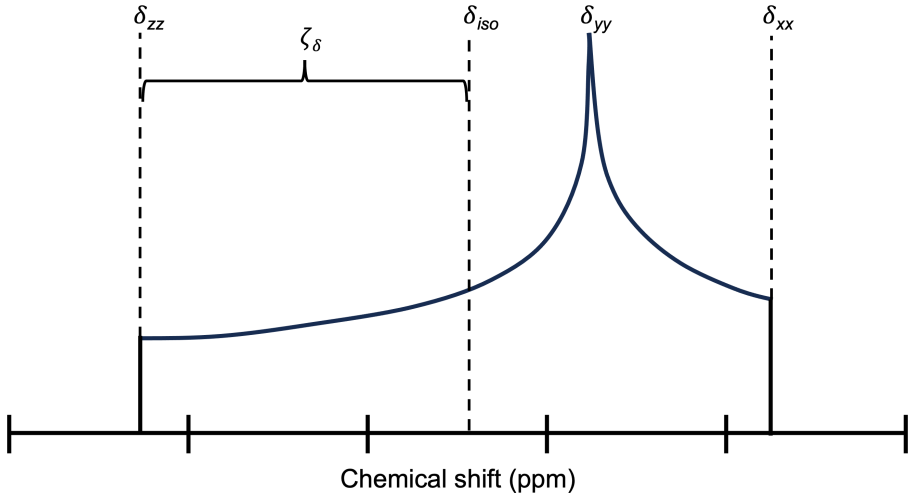

Figure 1.10: Example of a solid-state NMR spectrum demonstrating the components of the chemical shift tensor. Figure adapted from Reference [46].

transform. This yields a spectrum of peaks corresponding to different chemical environments at different frequencies. Conventionally, the frequency axis is then converted to a chemical shift axis with units of ppm so that spectra obtained on different instruments can be compared. By providing information about the environment around the nuclei, NMR experiments can give information about bonding, the distance between nuclei, the symmetry of a particular site on a crystal lattice, and the types of atomic motion within materials. [45]

$$\delta = \frac{\sigma_{ref} - \sigma_{sample}}{1 - \sigma_{ref}} \approx \sigma_{ref} - \sigma_{sample} \tag{1.4}$$

The most commonly reported NMR parameters are the isotropic chemical shielding or chemical shifts, where the chemical shielding/shift is represented by a second rank tensor. The isotropic chemical shielding/shift is given by the average of the three components of the diagonalized tensor and the conversion between chemical shift and shielding is given by Equation 1.4. In a solution-state experiment, the components of the chemical shift tensor are averaged by the rapid motion of molecules in solution,

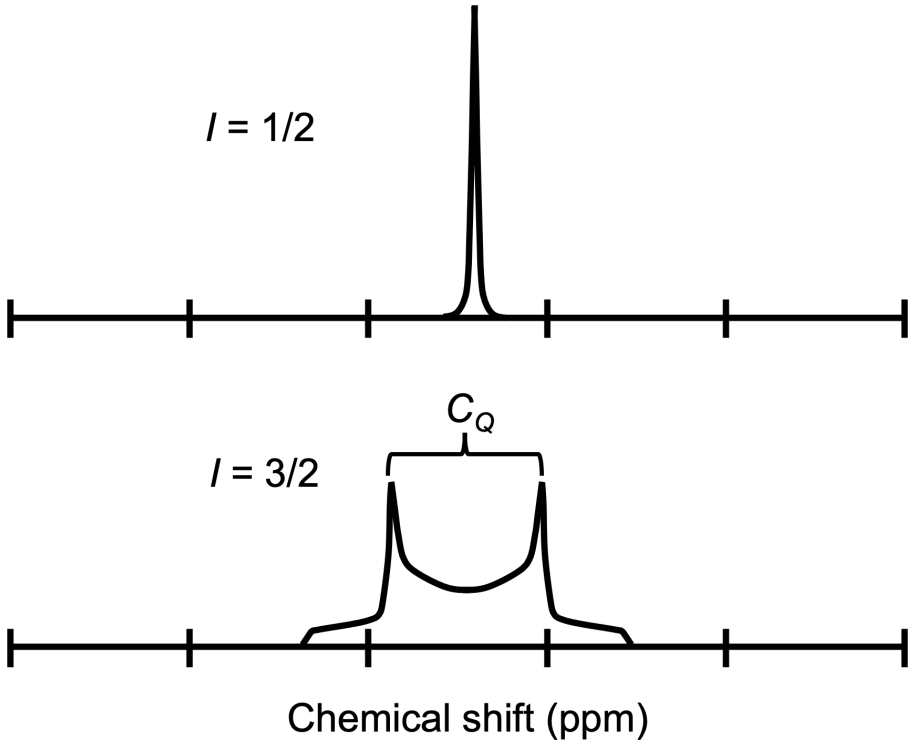

Figure 1.11: Example NMR spectra highlighting the differences in peak shape for spin-1/2 and spin-3/2 nuclei. Figure adapted from Reference [45].

so only the isotropic chemical shift is reported. In a static solid-state experiment, the motion of atoms is restricted, which results in a powder lineshape such as that shown in Figure 1.10 which reflects the anisotropy of interactions in the material. The position and appearance of this lineshape can provide information about the components of the chemical shift tensor, which can then be used to determine the chemical shift anisotropy (CSA, ζ_δ) and isotropic chemical shift. In most solid-state NMR experiments; however, magic-angle spinning is used to average out the anisotropic interactions in the sample, and therefore this work will focus on the isotropic chemical shielding and shift values.

Additionally, for any nuclei with a nuclear spin greater than 1/2, there will be an interaction between the quadrupolar moment of the nucleus and the electric field gradient (EFG) around the nucleus. In solid-state NMR, even under magic-angle spinning, the quadrupolar interaction cannot be completely averaged out. This results in

a lineshape which differs from the typical single peak observed for a spin-1/2 nucleus, illustrated in Figure 1.11. Similar to the chemical shielding, the quadrupolar interaction is described by a second-rank tensor, which when diagonalized, has components $|V_{ZZ}| > |V_{YY}| > |V_{XX}|$. These components are used to define the quadrupolar coupling constant (C_Q) and asymmetry parameter (η_Q), as shown in Eqns. 1.5 and 1.6, where eQ is defined as the quadrupolar moment of the nucleus. [47] The values for these parameters determine the width and shape of the quadrupolar lineshape and are generally determined by fitting spectra in a software package such as Topspin.

$$C_Q = \frac{eQV_{ZZ}}{h} \tag{1.5}$$

$$\eta_Q = \frac{V_{XX} - V_{YY}}{V_{ZZ}} \tag{1.6}$$

Although there are other important interactions in NMR experiments, such as the dipolar and J couplings, the measurements in Appendix A focus on the values of the isotropic chemical shift and the quadrupolar coupling constant in a solid-state sample. The chemical shift is usually used to evaluate the bonding environment around the nuclei of interest. In solution-state experiments, the correlation between specific chemical shift ranges and bonding environments is well-known, facilitating interpretation of spectra. However, in solid-state experiments, the interpretation is often less clear, making DFT calculations of chemical shielding values an important technique. These calculations will be discussed in subsequent sections. In contrast, the quadrupolar coupling constant is sometimes more easy to interpret than the chemical shift. The quadrupolar coupling directly corresponds to the asymmetry of the site surrounding the nuclei of interest, such that highly symmetric sites show a low value of C_Q, while

asymmetric sites have a large value. By probing how this value changes with temperature, changes in a crystal structure or dynamics can be determined. Finally, by comparing experimental values of these parameters with those calculated by DFT, the validity of different structural models can be investigated.

1.4 Magnetic measurements

Although much of this thesis does not deal directly with magnetic properties, magnetic measurements were key to our understanding of the molybdenum- and tungsten-based perovskites in Chapters 3 and 4. Therefore, here I provide a brief overview of concepts in magnetism, magnetic measurement, and common equations which are used to model magnetic behavior.

In this work, all magnetic measurements were performed using a superconducting quantum interference device (SQUID) in a Quantum Design MPMS 3 instrument. Within this device, a sample is passed through a number of superconducting coils which are coupled to the SQUID. Via the Josephson effect, the output voltage of the SQUID is directly related to the magnetic moment of the sample passing through the coils. This signal is then further amplified and processed to give the sample magnetization, which is recorded by the data collection software. [48] In a typical experiment, the magnetic field (H) is kept constant and the temperature (T) is changed while measuring the magnetization (M). We can also calculate an additional quantity, the magnetic susceptibility (χ), which is defined as M/H. Alternatively, T can be held constant while sweeping H and measuring M. In this work I will primarily discuss measurements of the first type, which can help us to understand the composition of a material as well as any phase transitions that may be present.

Magnetism arises from the spin of electrons, and in the context of this thesis, because all the materials are semiconducting or insulating, we will assume that electron spins can be visualized as being localized to a particular atom. This is distinct from the models that are used to understand magnetism in metallic systems. Depending on how many electrons there are in a system and their interactions with one another, there are a number of ways that we can classify magnetism in materials. The first distinction which can be made here is whether or not a system contains unpaired electrons. In the case where all electrons are paired, the compound is described as being diamagnetic. Examples of some diamagnetic compounds described in this thesis are $Cs_3Bi_2Cl_9$ or $NaZr_2(PO_4)_3$. In reality, all compounds exhibit some amount of diamagnetism, but because this effect is weak compared to other types of magnetic behavior, it is not the dominant response observed in a magnetic measurement unless all electrons are paired. Diamagnets repel a magnetic field, therefore the experimentally-measured susceptibility will be negative. In the case where there are unpaired electrons, there are a few possibilities for how these electrons will be oriented. At high temperatures (what constitutes a high temperature is highly material-dependent), materials with unpaired electrons are paramagnetic, indicating that the spins are not aligned in any particular direction. However, when a magnetic field is applied, the spins will tend to align with the field, giving a positive value for the susceptibility. As the material is cooled, the spins can become ordered in a number of possible orientations. The two most common cases are where all spins are aligned in the same direction (ferromagnetism), or where neighboring spins are aligned in opposite directions (anti-ferromagnetism). Other groundstates are also possible, but they will not be discussed in detail here, as all the compounds discussed in this work remain paramagnetic for all temperatures measured.

$$\chi = \frac{C}{T - \theta_{CW}} \tag{1.7}$$

Magnetic measurements can provide insight into the composition of a material and what type of magnetic interactions may be present. This is often done by applying the Curie-Weiss law, shown in Equation 3.3. Here, χ is the susceptibility determined from the magnetization measured at each temperature point and normalized by the mass of the sample and the molar mass of the compound, such that the units are emu mol^{-1} Oe^{-1}. T is the temperature in K, C is the Curie constant, and θ_{CW} is the Curie-Weiss temperature. It is important to note that this formula should only be applied to susceptibility data in the paramagnetic regime where χ^{-1} is linear with T (significantly above the temperature range of any magnetic transitions). Additionally, as previously mentioned, all materials also show a diamagnetic response, so often a diamagnetic correction factor, χ_0, is included in Curie-Weiss fitting. The best practice for fitting susceptibility data to determine χ_0, C, and θ_{CW} is to fit χ^{-1} using Equation 1.8. [49] From the fit to this equation, the values of C and θ_{CW} can be extracted. The sign of θ_{CW} indicates whether the dominant interactions in the material are ferromagnetic (positive values) or anti-ferromagnetic (negative values). Additionally, the magnitude of this parameter indicates the strength of the interactions. The value of C is related to the effective magnetic moment per magnetic ion in units of Bohr magnetons by Equation 1.9. The value of the moment calculated using C can be compared to the expected moment based on the number of unpaired electrons in the system using Equation 1.10, where J represents the total angular momentum and g_J is the electron g factor (usually assumed to be 2). If there is a large discrepancy between the calculated moment from C and the expected moment, then it may indicate that the composition of the material is not what is expected, or that there are other interactions that the Curie-Weiss law

does not account for (spin-orbit coupling is a common example).

$$\chi^{-1} = \frac{T - \theta_{CW}}{\chi_0(T - \theta_{CW}) + C} \tag{1.8}$$

$$\mu_{eff} = \sqrt{8C} \tag{1.9}$$

$$\mu_{exp} = g_J\sqrt{J(J+1)} \tag{1.10}$$

Another important analysis method for M vs. T data for some compounds is to fit the data to the appropriate Kotani equation. More specifically, these equations can only be applied for metal ions in an ideal octahedral field where the ions are sufficiently distant from one another. [50] These requirements make the vacancy-ordered perovskites a suitable series of compounds in which to apply these equations, as they tend to have ideal octahedra which are separated from one another by the *A*-site cations. The Kotani equations are models for how the magnetic moment of various transition metal ions should vary with temperature, depending on the number of d electrons and the strength of spin-orbit coupling for the ion. In order to apply these equations, the susceptibility at each temperature is converted to an effective moment, and these values are plotted against k_BT/ξ, where ξ is a measure of the strength of spin-orbit coupling. The results are then compared with a plot of the appropriate Kotani equation against k_BT/ξ, and ξ can be varied to obtain a good match between experiment and theory. Similarly to a Curie-Weiss analysis, if there are large discrepancies between experimental data and the appropriate Kotani model, then the metal ions may have a different oxidation state or coordination environment than that which was assumed.

1.5 Density functional theory techniques

Several of the studies described in this thesis rely on density functional theory (DFT) calculations, which allow us to computationally probe the influence of different aspects of a crystal structure on properties. For example, in Chapters 2 and 5, DFT calculations were used to illustrate how changes in composition or atomic positions can change a material's bandgap or dielectric constant. Additionally, DFT calculations can help us to disentangle the effects of competing influences on material properties in a way which can be challenging to do in experiment. In DFT calculations, both the local environments of individual atoms and the bulk properties can be investigated using a variety of software packages such as the Vienna Ab-initio Simulation Package (VASP) [51–53] or the Cambridge Serial Total Energy Package (CASTEP). [54] These calculations rely on the theorems of Hohenberg and Kohn, which state that (1) the ground-state energy of a system is a unique functional of the electron density, and (2) the electron density that corresponds to the minimum value of this functional represents the true electron density of the system. [55] This fundamental relationship allows for the calculation of electronic, magnetic, and mechanical properties of many materials. In the following section, I will introduce the important terminology and concepts which underlie the use of common DFT software packages. Specifically, I will focus on plane-wave DFT packages, which are used for calculations on extended solids.

Using the Hohenberg and Kohn theorems described above, Kohn and Sham developed equations which provide a means to use these theorems to solve for the lowest energy state of an inhomogeneous electron gas. These equations lay the foundation for modern DFT calculations. [56] They show that the energy functional could be written in terms of components with previously derived forms, such as the kinetic energy of the electrons, the coulombic attractions between electrons and nuclei, and the repul-

sions between pairs of electrons, in addition to a component with an unknown form, called the exchange-correlation functional, as shown in Equation 1.11. [57] The first proposed form of the exchange-correlation functional was the local density approximation (LDA), which is dependent on the density of the electron gas at each point in space. More complex functionals were later implemented, such as the Perdew, Burke, and Ernzerhof (PBE) functional, which depends both on the electron density and its spatial gradient. [58] Most of the calculations presented in this work rely on the PBE functional, as it provides a good balance of accuracy and computational efficiency.

$$\{\frac{1}{2}\overrightarrow{\nabla}^2 + V_H[n_0(r)] + V_{EXT}(r) + V_{XC}[n_0(r)]\}\phi_i(r) = \varepsilon_i\phi_i(r) \tag{1.11}$$

In addition to the derivation of sufficiently accurate exchange-correlation functionals, several other key advances are key to the DFT calculations presented here. The first was the question of how to represent the Kohn-Sham orbitals in the type of extended crystalline solids that are generally of interest to materials scientists. Using Bloch's Theorem, as shown in Equation 1.12 and 1.13, provided a solution. [57] Orbitals used to solve the Kohn-Sham equations, ϕ, can be represented using a series of planewaves with energies up to some cutoff energy determined by the user.

$$\phi_j(r) = \sum_k e^{-ikr}u_{j,k}(r) \tag{1.12}$$

$$u_{j.k}(r) = \sum_G c_{j,k}Ge^{-iGr} \tag{1.13}$$

This planewave expansion a provided way of representing the electron wavefunctions within a DFT calculation; however, in order to represent the wavefunctions of

electrons close to the nucleus, extremely large planewave energy cutoffs are necessary. Calculations including these electrons were thus very computationally expensive, prompting the use of pseudopotentials rather than all-electron wavefunctions.[59–63] Under this approximation, the electrons are defined as either core or valence, and the core electrons are assigned to a fixed configuration where they are described by smooth pseudo wave functions. Valence electrons are then defined using a nodeless pseudo-wave function, and the interaction between core and valence electrons is represented by the pseudopotential.[57] An additional development in this approach was the use of ultasoft pseudopotentials [64], which allow even lower energy cutoffs to be used. A final key innovation that made certain DFT calculations possible was the projector augmented wave (PAW) [65, 66] transformation. The PAW method provides a way of transforming the pseudopotentials used in the electronic energy minimization calculations back to all-electron wavefunctions, so that properties that depend on the core electrons can be calculated.

Following the development of these techniques, as well as computing advances that make DFT calculations feasible within a reasonable length of time, it has become fairly routine to perform DFT calculations on a variety of compounds. A standard DFT calculation will begin with setting up the input files for the calculation, which specify the identity of the atoms and their location in the structure, the PAW pseudopotentials used to describe the electronic structure of those atoms, the way the structure should be described in reciprocal space, and the desired output of the calculation. The simplest type of calculation is the electronic minimization calculation, which allows us to converge on the electronic groundstate of the material of interest. In this process, an initial "guess" for the charge density is supplied, and that guess is used to determine an effective potential and to construct a Hamiltonian to solve the Kohn-Sham equations.

By solving the equation, a new charge density is determined, and a new Hamiltonian is constructed. This process, known as a self-consistency cycle, is continuously repeated until the energy of the new charge density is sufficiently similar to that of the old one. Once this criterion for the energy difference is met, the calculation has reached convergence and will terminate.

Once the electronic groundstate has been found, the Hohenberg and Kohn theorems tell us that we can use this information to access many other properties of the compound of interest. Here, I outline a few standard calculations which appear in the text of this thesis. The first is the structural relaxation, in which, starting from an initial model of the crystal structure, atoms are allowed to move in order to reduce the overall energy of the structure. In these calculations, after the electronic energy of the system is converged, the atomic positions are changed slightly, and a new series of self-consistency cycles is initiated. After these cycles are finished, the energy of the new structure is compared to that of the old structure, and the process begins again. As in the electronic energy minimization, the structural energy minimization involves specifying a convergence criterion for when the energies of the new and old structures are sufficiently similar. This technique has many uses, including evaluating the validity of structural models from diffraction studies, or investigating potential phase transitions and structural deformations. Additionally, structural relaxations can be constrained to preserve certain features of the original structure, including symmetry, lattice parameters, and unit cell volume. These types of constraints are especially helpful in facilitating comparisons with experimental data. For example, in Appendix A, structural relaxations were performed on the $NaZr_2(PO_4)_3$ crystal structures, and NMR calculations were performed on the relaxed structures to compare with experimental values. Similarly, in Chapter 5, structural relaxations were performed to determine if

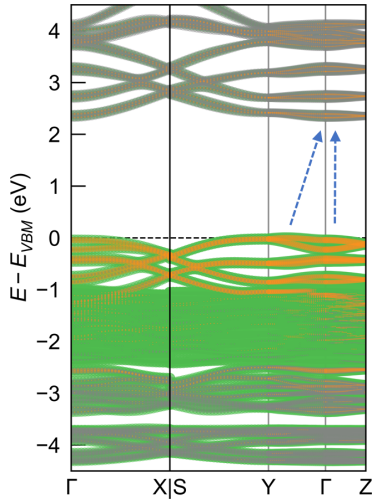

Figure 1.12: Example of a DFT-calculated bandstructure for $Cs_3Bi_2Cl_9$ with arrows illustrating the calculated bandgap for the material. Figure adapted from Reference [67]

they could give better agreement with experimentally-measured dielectric constants.

Another series of calculations which are commonly used in the study of halide perovskites are band structure calculations. For these calculations, it is necessary to already have a converged charge density from the self-consistent calculations outlined above. This charge density is then used to calculate the energy levels available to electrons at certain points of interest in reciprocal space, as shown in Figure 1.12. These points and the path taken between them are generally determined by the symmetry of the crystal structure. For semiconducting materials, like most halide perovskites, we are interested in understanding the behavior near the valence band maximum (VBM) (the highest occupied states) and the conduction band minimum (CBM) (the lowest unoccupied states). Some properties that we may be interested in are the energy difference between the VBM and CBM or the curvature of the bands around the VBM and CBM, as this will give us information about the bandgap of the material and the electron and hole effective masses. One well-known issue is that DFT calculations using the PBE functional tend to underestimate the bandgap of the material, and the magni-

tude of the error varies significantly depending on the system. [68] It is still possible to make qualitative comparisons of the bandgaps between similar compounds, but it is still often desirable to have a more quantitatively accurate bandgap estimate to compare with experimental results. Two common methods to resolve this issue are the Δ-sol method [68] and the use of hybrid functionals. The Δ-sol method uses a GGA functional, such as PBE, but estimates the bandgap by calculating the energy required to create an unbound electron-hole pair in the system of interest. This method is computationally cheap, but does rely on a number of assumptions and approximations. In a hybrid functional, some amount of exact exchange to account for electron correlation is included in the functional, where the magnitude and form of this exchange depends on the functional used. Common examples include the HSE and B3LYP functionals. This method can provide improvements in a number of predicted properties for semiconductors; however, the drawback is that they are significantly more computationally expensive. Therefore, if calculations on many systems are desired, it is often more practical to use the Δ-sol method, while a hybrid functional may be used to perform more detailed calculations on a single system.

A related technique is the density of states (DOS) calculation. Similarly to the band structure calculation, this requires an already-converged charge density and tells us about the electronic states available in the material and their energy with respect to the Fermi level. However, rather than showing how these energy levels vary in reciprocal space, the DOS calculation is used to show the relative number of states available at each energy, and often the orbital character of these states. An example of this is shown in Figure 1.13. In the halide perovskites, these calculations are useful in helping us determine which atoms in the crystal structure are influencing the VBM and CBM, which in turn can provide insight into how the optoelectronic properties of a material

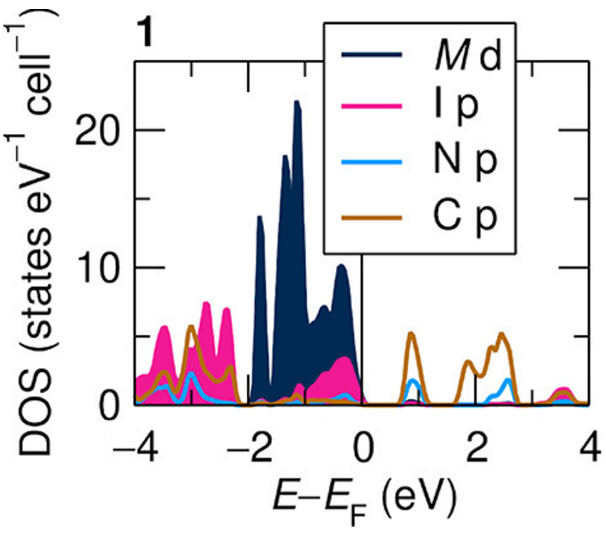

Figure 1.13: Example of a DFT-calculated DOS for Cu_2I_2(1,5 – naphthyridine) with orbital projections. Figure adapted from Reference [69]

might be manipulated. In these calculations as well, the use of the PBE functional can lead to inaccuracies in the DOS for semiconductors due to the error in the calculated bandgap. Another common issue seen in standard orbital-projected DOS calculations is charge spilling, which is when the software cannot accurately assign the charge density to a given atom and/or orbital. This issue can be at least party resolved through the use of the LOBSTER software package [70–73], which can also give access to information about whether a state arises from bonding or anti-bonding interactions. This software was used in Chapter 2 to help clarify the influence of iodine site preference on the bandgap of various compositions. The primary disadvantages of this type of calculation is a slightly increased computational cost and the fact that LOBSTER is not compatible with calculations that involve spin-orbit coupling. Therefore, it is not always suitable for use on calculations on the lead halide systems, as spin-orbit coupling has a strong influence on the nature of the VBM and CBM in these systems.

The final set of calculations that I will address here are those that involve determining a material's response to an external stimulus. These calculations, such as NMR

or dielectric response calculations, are more complex than a standard DFT calculation, because they require more than simply finding the electronic groundstate of a structure. For example, in an NMR calculation, the goal is to determine the chemical shielding and electric field gradient (EFG) tensors for various atoms in the structure, which describe the response of those atoms to radiofrequency (RF) radiation under an applied magnetic field. While the EFG tensor can be determined by the ground-state charge density, the calculation of the shielding tensor requires the calculation of the induced magnetic field, which is given by the Biot-Savart law in Equation 1.14. More specifically, an expression for the first order current, $\mathbf{j}^{(1)}(\mathbf{r}')$, must be derived. [47] In the VASP and CASTEP software packages, the standard approach to this calculation is known as the gauge-including projector augmented wave (GIPAW) method. The key achievement of the GIPAW method was to build on the previously-discussed PAW method to derive a Hamiltonian and expression for $\mathbf{j}^{(1)}$ that correctly incorporated the use of pseudopotentials and maintained translational invariance. [74] By meeting all of these requirements, the GIPAW method provides both accuracy and reasonable computational cost. This method was used extensively in Appendix A to aid in the interpretation of NMR spectra for $NaZr_2(PO_4)_3$. While it can be useful for many systems, a major shortcoming of the GIPAW method is that it does not incorporate the effects of temperature. In order to accurately include the effects of atomic motions at various temperatures, more advanced calculations are required, such as Monte Carlo simulations, [75] molecular dynamics, [76] or phonon mode calculations. [77]

$$\mathbf{B}_{in}(\mathbf{r}) = \frac{1}{c}\int d^3r' \mathbf{j}^{(1)}(\mathbf{r}') \times \frac{\mathbf{r}-\mathbf{r}'}{|\mathbf{r}-\mathbf{r}'|^3} \tag{1.14}$$

In the case of dielectric property calculations, the goal is to determine the response of the charge density to an applied electric field. This problem is computationally chal-

lenging for a number of reasons. The first is that there are both ionic and electronic contributions to the dielectric response. The ionic contribution arises from the movement of the atoms themselves, while the electronic contribution is due to the polarization of the electron cloud around each atom. Additionally, each of these responses has its own frequency-dependence due to the differing timescales of nuclear and electron motion. For frequencies that are similar to the timescale of these motions, resonance will enhance the contribution of that motion. Similarly, for frequencies that are of a significantly faster timescale, the contribution from that motion will approach zero. In Chapter 5 of this work, dielectric response calculations were limited to determination of the static dielectric constant, so frequency-dependence is not incorporated. These calculations follow the work of Gajdoš *et. al.*, [78, 79] and the reported results are based on the calculated macroscopic dielectric tensor. Similarly to other calculations discussed here, the dielectric response calculation often suffers from errors related to inaccuracies in the bandgap prediction or the fact that temperature effects are neglected. However, there have been advances in reducing these errors using hybrid functionals and phonon calculations. [80, 81]

In summary, this section has introduced a number of key concepts and terminology which are essential to understanding routine DFT calculations like many of those presented in this thesis. DFT allows us to develop an understanding of materials simply by knowing its structure and composition, making it an important tool in many disciplines within materials science. These calculations have been key both in providing a fundamental understanding of bonding and electronic structure in materials of interest, as well as in facilitating interpretation of experimental data, as will be demonstrated in the following chapters.

Chapter 2

Tunable Perovskite-Derived Bismuth Halides: $Cs_3Bi_2(Cl_{1-x}I_x)_9$

Bismuth-based perovskites are of interest as safer alternatives to lead-based optoelectronic materials, with several prior studies reporting on the compounds $Cs_3Bi_2Cl_9$, $Cs_3Bi_2I_9$, and $Cs_3Bi_2Cl_3I_6$. Here we examine a range of compounds of the formula $Cs_3Bi_2(Cl_{1-x}I_x)_9$, where x takes values from 0.09 to 0.52. Powder and single crystal X-ray diffraction were used to determine that all of these compounds adopt the layered vacancy-ordered perovskite structure observed for $Cs_3Bi_2Cl_3I_6$, which is also the high-temperature phase of $Cs_3Bi_2Cl_9$. We find that even with very small I incorporation, the structure is switched to that of $Cs_3Bi_2Cl_3I_6$ with I atoms displaying a distinct preference for the capping sites on the BiX_6 octahedra. Optical absorption spectroscopy was employed to study the evolution of optical properties of these materials, and this is complemented by density functional theory electronic structure calculations. Three

The contents of this chapter have substantially appeared in Reference [67]. Reproduced with permission from: E. E. Morgan, S. M. L. Teicher, G. Wu, L. Mao, and R. Seshadri, Tunable Perovskite-Derived Bismuth Halides: $Cs_3Bi_2(Cl_{1-x}I_x)_9$ *Inorg. Chem.* 59 (2020) 3387–3393.

main absorption features were observed for these compounds, and with increasing x the lowest-energy features are red-shifted.

2.1 Introduction

In the past decade, significant improvements have been made in the efficiency of halide perovskite-based solar cells, [82] where the most efficient devices have been made using lead-containing perovskites, which have the general chemical formula $A\mathrm{Pb}X_3$. [6] Here, A denotes a monovalent cation, which is generally either a large inorganic cation such as Cs^+, or a small organic cation, such as methylammonium or formamidinium, and X denotes a halide, usually Cl^-, Br^-, or I^-. Lead-halide perovskites containing at mixture of different A site cations [83] and X site anions [84] have provided tunability of particular interest to researchers. As these materials now display efficiencies comparable to those seen in commercially-available silicon-based cells, it is likely that they will play a significant role in the future of solar energy. [82]

Despite the promise of lead-halide perovskites, there is substantial concern as to whether they can be implemented on a large scale due to the toxicity associated with lead-based compounds. Although significant lead emissions are already associated with conventional industrial processes, [85] potentially high levels of lead exposure could occur as a result of the manufacturing or improper disposal of lead-perovskite solar cells. [86] While there may be methods to circumvent these issues, many researchers have sought lead-free perovskites that may be able to match the exciting optoelectronic properties associated with lead-halide perovskites. Metals such as tin, germanium, antimony, and bismuth have been proposed as potential substitutes for lead; however, there have not been any reports of lead-free perovskites that have comparable perfor-

mance to the lead-halide system. [87]

Among these metals, Bi is viewed as one of the most promising alternatives to lead, because Bi^{3+} has the same electronic structure as Pb^{2+}, can form the perovskite structure, has low toxicity, and is air-stable. [88] Accordingly, Bi-based perovskites have been studied with a variety of combinations of *A*-site cations and *X*-site anion, and in a range of forms, including thin films, nanocrystals, and bulk crystals. [89, 90] Previous experimental and computational work on materials such as BiI_3 [91] and $A_3Bi_2I_9$ (A = K, Rb, Cs) [92] has concluded that these materials have properties that make them promising for photovoltaic applications. Furthermore, Park *et al.* proposed the compounds $Cs_3Bi_2I_9$, $MA_3Bi_2I_9$, and $MA_3Bi_2I_{9-x}Cl_x$ as photovoltaic materials with low toxicity, with $Cs_3Bi_2I_9$ exhibiting a power conversion efficiency of greater than 1%. [88] Subsequently, $Cs_3Bi_2I_9$ nanocrystals have been extensively studied for their photovoltaic properties, [93, 94] and $MA_3Bi_2I_9$ thin films have achieved improved efficiencies of 3.17%. [95]

While these Bi compounds are bulk 3D crystals, the connectivity of the BiX_6 octahedra often yields an electronic structure with effectively limited dimensionality. In their work, Xiao *et al.* demonstrate that in order for lead-free perovskites to match the efficiencies observed in the *A*PbX_3 compounds, they must exhibit higher electronic dimensionality. [96] Thus, in order to improve the performance of materials such as $Cs_3Bi_2Cl_9$ and $Cs_3Bi_2I_9$, it is of interest to find ways to convert these structures, which feature 1D and 0D connectivity, respectively, to 2D connectivity. One example of this is the compound $Cs_3Bi_2I_6Cl_3$, which has a 2D layered structure, an absorption edge of 2.07 eV, and a direct band gap. [97]

In this work, we expand the family of compounds with the formula $Cs_3Bi_2(Cl_{1-x}I_x)_9$, where x ranges from 0.09 to 0.52 through solution synthesis. The compounds were

characterized by X-ray fluorescence spectroscopy, single-crystal and powder X-ray diffraction, UV-vis spectroscopy, and electronic structure calculations, and compared to the end-member compounds. We find that adding small amounts of I to $Cs_3Bi_2Cl_9$ causes a large change in both the structure and electronic properties of the material, and that adding successively greater amounts of I allows systematic tuning of the optical absorption edge within the visible region of the optical spectrum. Interestingly, the structures adopted by members of the solid solution described here are not the stable structures of either of the end-members, $Cs_3Bi_2Cl_9$ or $Cs_3Bi_2I_9$. Density-functional theory-based electronic structure calculations provide insights into the causes for the dramatic changes in the optical absorption onset upon I substitution.

2.2 Experimental Methods

2.2.1 Synthesis

All reagents were purchased from Sigma Aldrich or Fisher Scientific and were used without further purification or modification.

$Cs_3Bi_2Cl_9$ was prepared by adding 1 mmol Bi_2O_3 to 4 mL of HCl (37 wt% in H_2O). The mixture was heated and stirred at 100 °C for 2 min to fully dissolve the Bi_2O_3. 3 mmol CsCl was added to the solution, and the mixture was heated and stirred for an additional 5 min. After cooling, colorless crystals were isolated and dried by vacuum filtration.

$Cs_3Bi_2I_9$ was prepared by adding 1 mmol Bi_2O_3 to mixture of 4 mL HI (57 wt% in H_2O) and 0.15 mL H_3PO_2 (50 wt% in H_2O). The mixture was heated and stirred at 100 °C for 2 min to fully dissolve the Bi_2O_3. 3 mmol CsCl was added to the solution,

and the mixture was heated and stirred for an additional 5 min. After cooling, dark red crystals were isolated and dried by vacuum filtration.

$Cs_3Bi_2Cl_{9-x}I_x$ samples were prepared by first preparing mixtures containing various proportions of HCl (37 wt% in H_2O) and HI (57 wt% in H_2O) by adding volumes of HI varying from 0.05 mL to 0.50 mL, to 4 mL HCl. 1 mmol Bi_2O_3 was added to each acid solution. The mixtures were heated and stirred at 100 °C for 2 min to fully dissolve the Bi_2O_3. 3 mmol CsCl was added to each solution, and the mixture were heated and stirred for an additional 15 min. After cooling, crystals which ranged in color from yellow to reddish-orange were isolated and dried by vacuum filtration.

2.2.2 X-ray diffraction

Powder X-ray diffraction (PXRD) measurements were performed on a Panalytical Empyrean powder diffractometer in reflection mode with a Cu-Kα radiation source. Rietveld analysis was performed to estimate lattice parameters using the TOPAS software package. [36]

Single-crystal X-Ray diffraction (SC-XRD) data was collected for $Cs_3Bi_2Cl_9$ and one $Cs_3Bi_2Cl_{9-x}I_x$ sample on a Bruker KAPPA APEX II diffractometer with an APEX II CCD detector, TRIUMPH monochromator, and Mo-Kα radiation source (λ = 0.71073 Å). The crystal structure was solved by Dr. Lingling Mao using direct methods and refined by full-matrix least squares on F2 using the OLEX2 program package. [98] Crystal structures were visualized using the VESTA software package. [99]

2.2.3 X-ray fluorescence spectroscopy

X-ray fluorescence (XRF) data were collected using a Rigaku ZSX Primus IV XRF spectrometer, which was used to determine the relative mass % of Cl and I present in each sample. The program used was set up to detect Cs, Bi, Cl, and I using the Cs-Kα, Bi-Lα, Cl-Kα, and I-Kα lines with a scanning time of 15 sec and a fixed angle measurement time of 15 sec for each element. Multiple measurements, each with a scan diameter of 0.5 mm, were made for each compound, and the results were averaged to determine the composition of each compound.

2.2.4 UV-vis spectroscopy

Absorbance spectra were obtained by measuring diffuse reflectance on a Shimadzu UV3600 UV-Vis-NIR spectrometer equipped with an integrating sphere. Reflectance was converted to absorbance using the Kubelka-Munk transformation. [44]

2.2.5 Density functional theory calculations

All electronic structure calculations were performed using density functional theory (DFT)[55, 56] as implemented in the Vienna Ab initio Simulation Package v5.4.4 [51–53] by Dr. Samuel Teicher. Calculations used the VASP-recommended PAW potentials [66, 100] and the PBE [58] and HSE06[101] functionals with energy convergence better than 10^{-6} eV.

We used structural parameters from $Cs_3Bi_2Cl_9$ single crystal diffraction for the 0D-connectivity space group 62 structure. For the 2D-connectivity structures in space group 164, we performed calculations using the structure refined from single-crystal

X-ray for $Cs_3Bi_2I_{0.8}Cl_{8.2}$ as well as using lattice parameters linearly-interpolated between hypothetical 0% and 100% iodine incorporation structures based on the trends from powder X-ray diffraction Rietveld fits (see Figure 2.3). We employed a plane-wave energy cut-off of 500 eV and used the automatic k-mesh generation scheme with the length parameter, l, set to 20 and 30 for PBE and HSE06 calculations, respectively ($l = 30$ corresponds to a k-mesh of $4 \times 4 \times 2$ for the group space 62 structure and a mesh between $5 \times 5 \times 3$ and $4 \times 4 \times 3$ for the group 164 structures). Band structure calculations were performed using a density of 30 and 16 k-points per branch for the PBE and HSE06 calculations, respectively. Using these parameters, the band gaps appear to be converged much better than 0.1 eV in all cases. Crystal orbital Hamilton bonding analysis was performed in the LOBSTER software package. [70–73]

2.3 Results and Discussion

Single crystals of $Cs_3Bi_2Cl_9$ and of a compound whose composition was established to be $Cs_3Bi_2Cl_{8.16}I_{0.84}$ were obtained directly from the reaction mixtures, and their structures as determined from single-crystal X-ray diffraction at room temperature are shown in Figure 2.1. The conditions for single crystal data collection and select crystallographic parameters are summarized in Table 2.1. Additional images of the crystals and crystallographic details can be found in Appendix C. The structure of $Cs_3Bi_2Cl_9$ matched the reported structure which is found at temperatures up to $T = 646$ K. The structure is orthorhombic, in the $Pnma$ space group and can be visualized as 1D chains of clusters of $BiCl_6$ octahedra (Figure 2.1 (a,b)). While this structure has corner-connected $BiCl_6$ octahedra reminiscent of a perovskite, the *A* sites do appear to describe the topology of a simple cubic lattice. Therefore, the structure $Cs_3Bi_2Cl_9$ is not

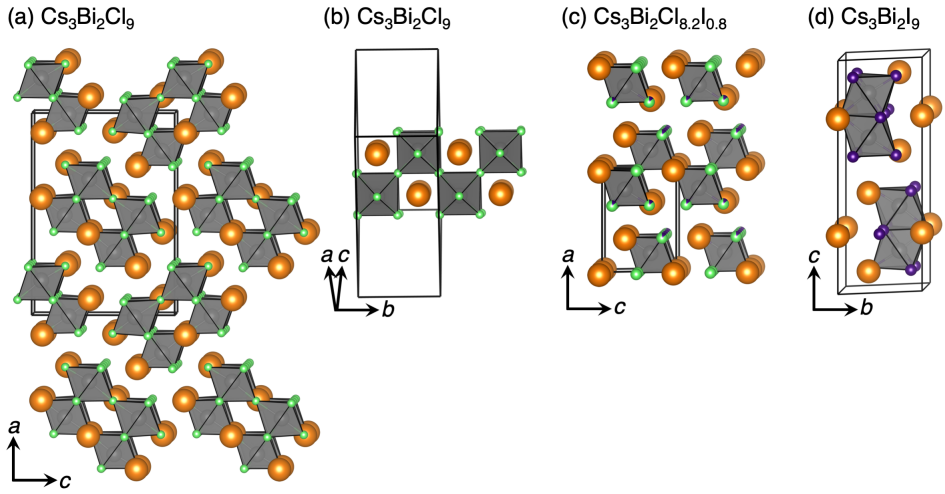

Figure 2.1: (a) One-dimensional crystal structure of $Cs_3Bi_2Cl_9$ ($Pnma$, S.G. #62) viewed down the 1D chains of $BiCl_6$ octahedra. (b) The same structure of $Cs_3Bi_2Cl_9$ emphasizing one of the chains of $BiCl_6$ octahedra. (c) Two-dimensional vacancy-ordered perovskite structure of $Cs_3Bi_2Cl_{8.16}I_{0.84}$ ($P\bar{3}m1$, S.G. #164) viewed down the b axis, depicting the 2D sheets of $BiCl_6$ octahedra. (d) Zero-dimensional structure of $Cs_3Bi_2I_9$ ($P6_3/mmc$, S.G. #194) showing the condensed, face-shared double octahedra of $Bi_2I_9^{3-}$. Single-crystal X-ray diffraction and refinements performed by Dr. Lingling Mao.

Empirical formula	$Cs_3Bi_2Cl_9$	$Cs_3Bi_2Cl_{8.16}I_{0.84}$
Form. wt. ($g\,mol^{-1}$)	1135.74	1212.61
Crystal habit and color	Rods, colorless	Hexagonal plates, yellow
Crystal system	Orthorhombic	Trigonal
Space group	$Pnma$ (No. 62)	$P\bar{3}m1$ (No. 164)
Temperature (K)	300	299
Wavelength (Å)	0.71073	0.71073
a (Å)	18.644(5)	7.7587(6)
b (Å)	7.6182(19)	7.7587(6)
c (Å)	13.186(4)	9.5183(8)
α (°)	90	90
β (°)	90	90
γ (°)	90	120
Volume ($Å^3$)	1872.8(8)	496.21(9)
Density (calc.) ($g\,cm^{-3}$)	4.028	4.058
θ range (°)	3.276 to 28.327	2.140 to 30.550
Completeness to θ = 25.242°	99.5%	100%
Reflections collected	8746	3782
Data / restraints / parameters	2497 / 0 / 76	616 / 0 / 20
Goodness-of-fit	1.100	1.097
Final R indices [$I > 2\sigma(I)$]	R_{obs} = 0.0319 wR_{obs} = 0.0658	R_{obs} = 0.0261 wR_{obs} = 0.0678

Table 2.1: Single-crystal X-ray diffraction refinement data and results for $Cs_3Bi_2Cl_9$ and $Cs_3Bi_2Cl_{8.16}I_{0.84}$. Single-crystal X-ray diffraction and refinements performed by Dr. Lingling Mao.

technically a perovskite. Similarly, Figure 2.1(d) displays the other end member of the series, $Cs_3Bi_2I_9$, which is also not perovskite-derived since the BiI_6 form as face-sharing pairs.

The compound $Cs_3Bi_2Cl_{8.16}I_{0.84}$ crystalizes in the trigonal space group $P\bar{3}m1$ and adopts a structure than be described by an ordered vacancy (□) ordering on the perovskite $A_3B_2\square X_9$ that results in layers of vacancies separated by double-layers of BiX_6 octahedra. The structure is very similar to that of β-$Cs_3Bi_2Cl_9$, but with a unit cell that is 3.8% smaller than what is reported, due to the fact that the structure of β-$Cs_3Bi_2Cl_9$ was reported at 723 K. [102] The 2D structure described here is also adopted by $Cs_3Sb_2I_9$ [103] and $Rb_3Bi_2I_9$. [92] In this structure, the BiX_6 octahedra are corner-sharing and form corrugated 2D layers (Figure 2.1 (c)). The broad family of $A_3B_2\square X_9$ structures have been previously described [104] as adopting 0D, 1D, and 2D variants, related by the order-disorder framework developed by Dornberger-Schiff and Grenn-Niemann. [105]

In their characterization of the structure of $Cs_3Bi_2I_6Cl_3$, which has a similar structure, McCall *et.al.* found that the I atoms preferred to occupy the capping positions on the octahedra in the structure, while the Cl atoms occupy the bridging positions between the octahedra. [97] In the refinement of the structure presented here for $Cs_3Bi_2Cl_{8.16}I_{0.84}$, we observe a similar tendency, with corner-sharing sites between octahedra occupied exclusively by Cl, and a mixture of I and Cl atoms in the other sites. This site preference may provide a driving force for the incorporation of I into the structure, as the structure tries to maximize the amount of I in the capping sites. The origin of this site preference is revisited in the discussion of the electronic structure.

The composition of the different $Cs_3Bi_2Cl_{9-x}I_x$ compounds in the series were determined using X-ray fluorescence, and the results are displayed in Figure 2.2. As ex-

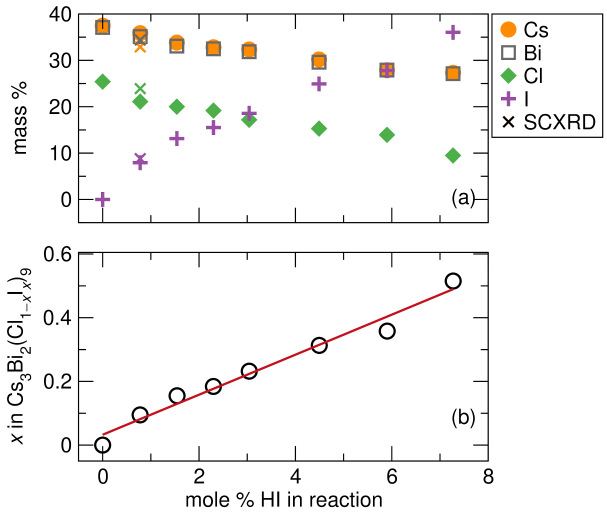

Figure 2.2: (a) Compositions of the title compounds as determined by X-ray fluorescence (XRF) as a function of the percentage of HI in the reaction mixture. For the solid solution compound $Cs_3Bi_2Cl_{8.16}I_{0.84}$, the composition obtained from single crystal X-ray diffraction (SCXRD) refinement is indicated in appropriate location. (b) Values of x in $Cs_3Bi_2(Cl_{1-x}I_x)_9$ plotted against the proportion of HI in the reaction mixture.

pected, it was observed that the mass % of Cl and I vary linearly with the percentage of HI in the reaction mixture. Interestingly, it should be noted that in the plot of I occupancy *vs* % HI in the reaction, the slope of the linear fit is close to 6% I/1% HI, demonstrating that the occupancy of the *X* sites is not the same as the ratio of I to Cl in the reaction mixture. For example, when the reaction mixture contained 7.27% HI, the product had an I occupancy of 52 %. It is clear from these results that there is a large driving force for the incorporation of I into the structure, which likely originates from the previously-discussed site preference for I and Cl.

Figure 2.3 displays the evolution of powder X-ray diffraction patterns of the different compounds in the solid solution that crystallize in the 2D vacancy-ordered perovskite structure in space group $P\bar{3}m1$. The overlaid Rietveld fits suggest that all of the samples are single phase within the detection limits established by laboratory x-ray diffraction data. In the case of the end-member compounds, powder patterns for

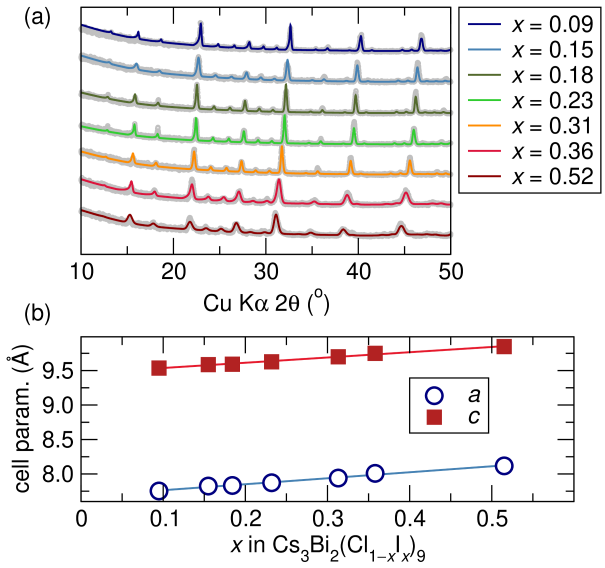

Figure 2.3: (a) Evolution of X-ray diffraction patterns of the compounds $Cs_3Bi_2(Cl_{1-x}I_x)_9$ with the single-phase Rietveld fits to the 2D vacancy-ordered perovskite structure overlaid. Rietveld analysis confirms the absence of extraneous peaks that would suggest secondary phase. (b) Evolution of the cell parameters with x of $Cs_3Bi_2(Cl_{1-x}I_x)_9$.

$Cs_3Bi_2Cl_9$ and $Cs_3Bi_2I_9$ (not displayed) matched those of previously reported structures for α-$Cs_3Bi_2Cl_9$ and bulk $Cs_3Bi_2I_9$. In addition to a shift to lower 2θ values with increasing I content, the peaks also exhibit broadening with increasing amounts of I, as shown in Figure 2.3. This broadening is attributed to the decreasing size of the crystallites as the amount of I in the sample increases.

Diffuse reflectance spectra transformed using the Kubelka-Munk method into absorbance for each compound is shown in Figure 2.4. As expected from the appearance of compounds, the absorption edge shifts to lower energies with increasing I occupancy. Additionally, the absorbance peak widens with increasing I. From the absorbance data, the absorbance edge for each compound was calculated and is presented as a function of the composition in Figure 2.4(b). A large decrease in the energy of the first absorption edge is noted immediately upon I incorporation, corresponding to the change from the 1D structure to the 2D structure. As more I is incorporated into the lattice, the

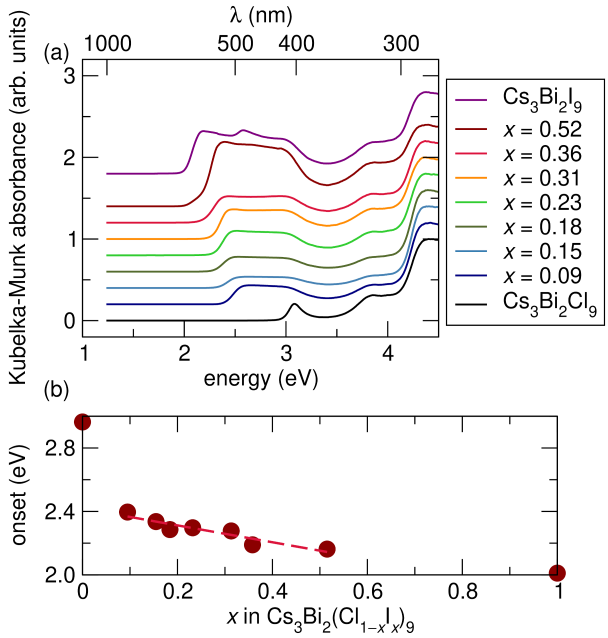

Figure 2.4: (a) Kubelka-Munk transformed optical absorption data on powders of $Cs_3Bi_2(Cl_{1-x}I_x)_9$. (b) Absorption onset as a function of x.

energy of the absorption edge decreases nearly linearly with the increasing I occupancy.

The optical absorption data suggests that the structure and composition of these compounds have distinct influences on their optical properties. Therefore, density functional theory-based calculations were carried out in order to gain a better understanding of the relative roles of roles of structural connectivity and I substitution on the measured band gaps. Figure 2.5 presents the calculated band gaps of compounds with the 2D vacancy-ordered perovskite structure. This includes hypothetical compositions of $Cs_3Bi_2Cl_9$, $Cs_3Bi_2I_9$, $Cs_3Bi_2Cl_3I_6$, in which I sits on the $6i$ capping Wyckoff site and Cl sits on the $3e$ site, and $Cs_3Bi_2Cl_6I_3$, in which Cl and I occupation is reversed to the $6i$ and $3e$ sites, respectively. The treatment of these four structures provides qualitative understanding of the role of I site occupation without breaking space group symmetry and needing to consider more complex supercell calculations. In addition to stoichiometric changes, there is significant lattice expansion with increased I concentration. In

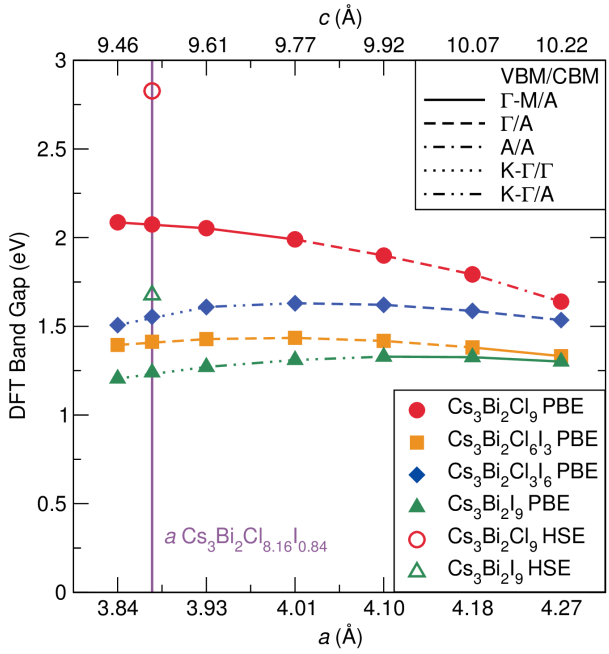

Figure 2.5: DFT band gaps of compounds in the vacancy-ordered 2D perovskite structure in space group $P\bar{3}m1$. We compare simulations of compounds $Cs_3Bi_2Cl_9$, $Cs_3Bi_2Cl_6I_3$, $Cs_3Bi_2Cl_3I_6$, and $Cs_3Bi_2I_9$ structures with varying iodine filling and varying lattice parameter. In addition, we have repeated all the calculations using the lattice parameters of $Cs_3Bi_2Cl_{8.16}I_{0.84}$ determined by single crystal X-ray diffraction (Note: the c/a ratio for $Cs_3Bi_2Cl_{8.16}I_{0.84}$ is slightly different from that determined by powder Rietveld refinement, so the c axis is not valid for these data points; the adjustment is very minor, however). All simulations incorporated spin-orbit coupling. DFT calculations performed by Dr. Samuel Teicher.

order to account this effect, we have performed calculations for all four structures at lattice parameters corresponding to 0 %, 20 %, 40 %, 60 %, 80 %, and 100 % I substitution based on the linear lattice parameter trends of the powder Rietveld fits (Figure 2.3) as well as the lattice parameters of single crystal $Cs_3Bi_2Cl_{8.16}I_{0.84}$.

Transitions of the valence band maximum (VBM) and conduction band minimum (CBM) in Figure 2.5 are displayed using dashed lines. We find that across this solid solution, as in other perovskite systems with relatively flat conduction bands, [106] a great number of direct and indirect transitions can be favored based on subtle changes in bonding. Second, the fact that both $Cs_3Bi_2Cl_9$ and $Cs_3Bi_2I_9$ in the vacancy-ordered perovskite structure adopts a Γ-M/A gap in at their preferred lattice parameters suggests that the dominant transitions in the real material should be close to Γ-M/A.

When comparing with the calculated bandgap (PBE) for the 1D chain ($Pnma$) structure of $Cs_3Bi_2Cl_9$ structure of 2.32 eV (Figure 2.6), the band gap of $Cs_3Bi_2Cl_9$ in the hypothetical 100% Cl $P\bar{3}m1$ structure is 2.09 eV. The difference here is significant, but not as large as the absorption onset energy decrease between the first two data points of Figure 2.4(b) (≈ 0.5 eV). This suggests that structural transformation to the 2D-connectivity alone is not sufficient to recreate the band gap trend. Similarly the lattice parameter trend alone also cannot explain the large reduction in the experimental band gap. While the bandgap of $Cs_3Bi_2Cl_9$ decreases by about 0.3 eV upon compression to the theoretical lattice parameter of the $Cs_3Bi_2I_9$ structure, the trend does not hold for any the structures with I. The full I structure has a much smaller band gap than that of the full Cl structure and the magnitude of this reduction is consistent with the large drop seen in experiment. This is not surprising because of the relatively large size of I orbitals compared to Cl orbitals and the expectation that there will therefore be larger band dispersion in the I compound. The HSE band gaps, which are expected

to quantitatively match the measured values more closely than the PBE values, further confirm this intuition. The HSE band gap of the full Cl compound is quite close to that of $Cs_3Bi_2Cl_9$ measured in experiment, and the 2.8 ev to 1.7 eV band gap range between Cl and I compounds is roughly consistent with the range seen in experiment, albeit downshifted by about 0.2 eV from the values of 2.4(b).

A more subtle point is that the band gap of $Cs_3Bi_2Cl_6I_3$ is systematically lower than that of $Cs_3Bi_2Cl_3I_6$. This may seem surprising at first because the latter structure has double the concentration of I. This is due to the different bond distances and bond strengths for $6i$ and $3e$ site occupancy. The value of the integrated crystal orbital Hamilton population (ICOHP) has been found to form an effective computational proxy for bond strength in a wide variety of systems. The more negative the ICOHP, the stronger the bonding. Larger ICOHPs evidence stronger bonding in the full I structures: -3.4 eV and -2.1 eV for Bi-I bonding in $Cs_3Bi_2I_9$ on $6i$ and $3e$ sites, respectively, while for Bi–Cl bonding in $Cs_3Bi_2I_9$ on the same sites these values are -2.5 eV and -1.5 eV (here, we consider the ICOHP in the single crystal structure of $Cs_3Bi_2Cl_{8.16}I_{0.84}$. Moreover, the bonding strength of I on the $6i$ capping site is much greater than I on the $3e$ site or Cl on either site; this may explain the strong preference for I occupation on the $6i$ site. The bonding asymmetry is more broadly reflective of asymmetry in the electron distribution near the bismuth atom. The inset of Figure 2.6 shows the electron localization function of the Bi atom in relation to the octahedral bonding demonstrating a stereochemically-active lone pair that points away from the $6i$ sites and towards the $3e$ sites.

Figure 2.6 shows selected portions of the orbital-projected band structures of $Cs_3Bi_2Cl_9$ in the 2D vacancy-ordered perovskite structure ($P\bar{3}m1$) and the structure with 1D chains ($Pnma$). As expected, the 2D-bonding connectivity structure can be seen to

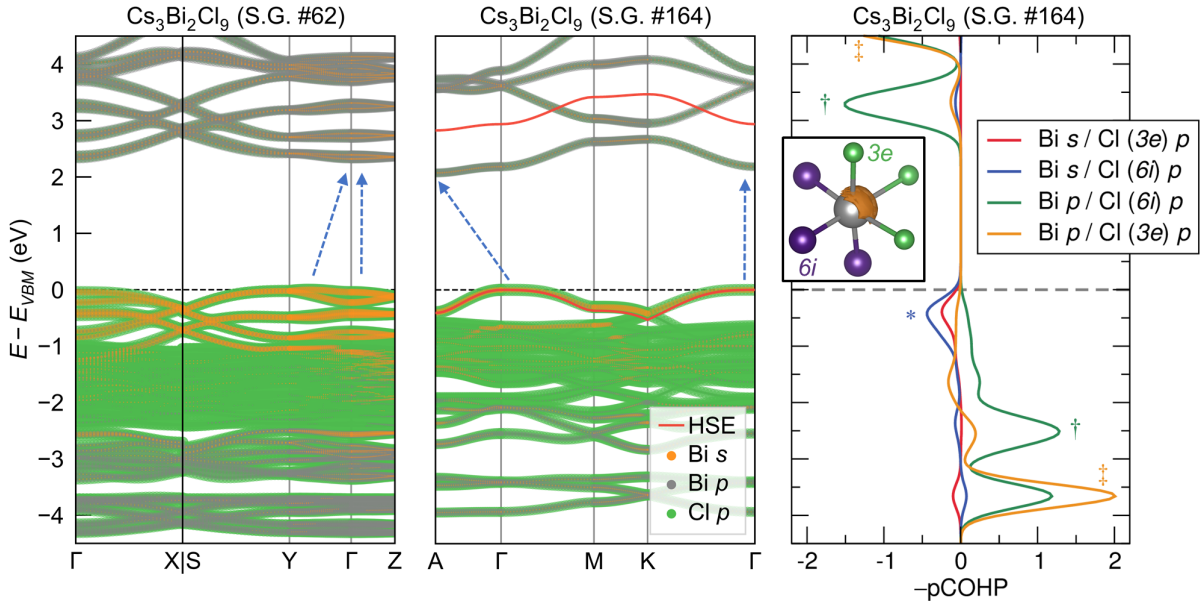

Figure 2.6: Calculated band structures of $Cs_3Bi_2Cl_9$ in the 1D chain structure ($Pnma$, S.G. 62) of $Cs_3Bi_2Cl_9$ and 2D vacancy-ordered perovskite structure ($P\bar{3}m1$, S.G. 164) of $Cs_3Bi_2Cl_{8.16}I_{0.84}$ single-crystal refined structures. The size of the dots represents the relative magnitude of orbital projections. Blue arrows indicate the smallest direct and indirect bandgaps (Γ/Γ;Γ-Y/Γ for the $Pnma$ structure and Γ/Γ;Γ-M/A for the $P\bar{3}m1$ structure). The HSE conduction and valence band are provided for reference on the S.G. 164 band structure. The third panel shows bond-projected COHP pairs for Bi–Cl orbital bonding with Cl on the $3e$ and $6i$ octahedral sites. The inset shows the electron localization function on the Bi atom at a contour of 0.57 electron in relation to the $3e$ and $6i$ sites. Annotations indicate: ($*$) Bi-s/Cl-p antibonding contribution at the VBM, (†) Bi-p-Cl($6i$)-p bonding and antibonding states that contribute to the CBM, and (‡) Bi-p-Cl($3e$)-p bonding and antibonding states that contribute to neither the CBM nor the VBM. DFT calculations performed by Dr. Samuel Teicher.

have larger band dispersions in both the conduction and valence band than the 1D-connectivity $Pnma$ structure. As in many other perovskite systems, electron filling of the Cl/I p orbitals and the loss of electrons by Bi p yields a band structure with dominant Cl/I p contributions in the valence band and dominant Bi p in the conduction band. A large Bi s contribution at the top of the valence band arises due to Bi s / Cl p antibonding interactions. The third panel of Figure 2.6 presents the un-integrated partial COHP of Bi–Cl bonding interactions in the 2D $P\bar{3}m1$ structure. Atoms on both the $6i$ and $3e$ sites contribute to the Bi s / Cl p antibonding interactions($*$) that push the VBM upwards in energy, whereas only atoms on the $6i$ site contribute to the Bi p / Cl p antibonding interaction(†) that pushes the CBM upwards in energy. This explains why the band gap of $Cs_3Bi_2Cl_6I_3$ is lower than that of $Cs_3Bi_2Cl_3I_6$. While placing I on either site increases bonding strength and band dispersion, ultimately closing the band gap, placing I on the non-preferred $3e$ site raises the energy of the Bi s/Cl p antibonding states in the valence band without also raising the energy of antibonding Bi p/Cl p states in the conduction band, closing the band gap much more rapidly.

Overall, the computational results suggests that, in addition to the increased 2D bonding connectivity in the vacancy-ordered perovskite structures, the effect of I incorporation on local bonding is essential to explaining the sharp reduction in band gap seen in experiment. Bonding asymmetry due to the stereochemically-active lone pair on the Bi is likely one reason for the preference for I occupation on the capping sites.

2.4 Conclusion

We have shown that even small I incorporation (small x) in the solid solution $Cs_3Bi_2(Cl_{1-x}I_x)_9$ switches the structure from lower dimensional structures to the vacancy-

ordered perovskite-type in the trigonal space group $P\bar{3}m1$. Associated with this substitution are dramatic changes in the optical properties, which can be further tuned with increasing I incorporation. Density functional theory-based electronic structure calculations point to the importance of the electronic changes induced by the orbital states of I over the changes in the structural dimensionality as dominating the changes in the optical absorption properties. They also point to the potential origin of the site-preference tendency of I^- that results in the structure being switched from 1D to perovskite-derived 2D upon I^- incorporation and that provides a driving force for I^- incorporation into the structure.

Chapter 3

Hybrid and Inorganic Vacancy-Ordered Double Perovskites A_2WCl_6

We report hybrid and all-inorganic, vacancy-ordered double perovskites of d^2 W^{4+} with the formulae A_2WCl_6 (A = $CH_3NH_3^+$, Rb^+, and Cs^+). These compounds, which are reddish in color, can be distinguished from structurally similar compounds obtained by hydrothermal methods on the basis of structure, spectroscopic, and magnetic properties. The latter are green and incorporate oxygen, with actual formulae $Cs_2WO_xCl_{6-x}$ and distinct optical absorption and emission behavior. The local-moment magnetism of the pure red d^2 compounds reported here do not correspond to the appropriate Kotani model, suggesting as-yet undiscovered physics in these systems.

The contents of this chapter have substantially appeared in Reference [107]. Reproduced with permission from: E. E. Morgan, G. T. Kent, A. Zohar, A. O'Dea, G. Wu, A. K. Cheetham and R. Seshadri, Hybrid and Inorganic Vacancy-Ordered Double Perovskites A_2WCl_6. Copyright 2023 American Chemical Society

3.1 Introduction

The K_2PtCl_6 structure type — more familiarly referred to as the vacancy-ordered double perovskite — was first identified in 1834, [14, 108] with the crystal structure established by Dickinson [109] in 1922. In recent years, compounds with this crystal structure have emerged as promising materials for optoelectronic applications. The structure type is defined by the formula A_2MX_6, where A is a monovalent cation such as Cs^+ or $CH_3NH_3^+$ (MA), M is a metal in the $4+$ oxidation state, and X is a halide anion. As implied by the name, the structure of these compounds can be visualized as a double perovskite in which the second M' site is vacant, resulting in isolated MX_6^{2-} octahedra bound electrostatically by A-site cations. [18, 110] Despite the lack of continuous cation–anion–cation connectivity, the iodide compounds display disperse bands as a consequence of the extended and polarizable orbitals on the anion. [110–112] Therefore, recent interest in these compounds has been driven by the potential use of Cs_2SnI_6 [110] and Cs_2TeI_6 [111, 113] as photovoltaic materials. Additionally, computational studies have explored the electronic structures of many members of the vacancy-ordered family and revealed structure-property relationships that can be used to select compounds with the most promising optoelectronic characteristics. [114–117]

Many early transition metal oxides prefer metal–metal bonding as a means of dealing with unpaired d electrons [118] which makes magnetic compounds with d^1, d^2, *etc.* configurations elusive. In the structure type described here, transition metal ions are forced to be somewhat distant, obviating metal–metal bonding, and permitting magnetism to manifest. Consequently, vacancy-ordered double perovskites based on transition metals have been used as model systems to study magnetism. For example, compounds such as Cs_2NbX_6 and Cs_2TaX_6 have revealed the influence of the X-site on magnetic properties, [119] and Cs_2TaCl_6 shows particularly interesting low-temperature

magnetism. [120, 121] Recently, some of us have reported a family of compounds with the general composition A_2RuX_6 [8, 122] where the identity of the *A*-site and *X*-site can be used to tune the effective strength of spin-orbit coupling in these compounds, as determined by fitting magnetic data to models proposed by Kotani.[50] Given the interesting trends revealed in these prior works, we wished to understand if similar behavior is seen in compounds with the overall formula A_2WX_6. It was also of interest to determine whether hybrid halide compounds of magnetic d^2 W^{4+} could be obtained.

There are a few reports of A_2WX_6 compounds where A = K, Rb, Cs, Ba, or Tl and X = Cl or Br. A solid-state synthesis from the alkali chloride salts and WCl_6 yielded reddish powders of A_2WCl_6. [123] Additionally, a single crystal structure study of Cs_2WCl_6 confirmed the red color and vacancy-ordered structure of this compound, but no further characterization was reported. [124] Interestingly, a more recent report has suggested that Cs_2WCl_6 and Cs_2MoCl_6 can be obtained from hydrothermal synthesis in HCl and describes both as forming green crystals displaying bright near-IR emission. [20]

Given that the reported properties of Cs_2WCl_6 appear to vary significantly depending on the synthesis method, we sought to synthesize the A_2WX_6 compounds and determine their compositions, structures, and properties. We find that they can be most easily prepared by combining the appropriate *A*-cation salt and WCl_4 under anaerobic and anhydrous conditions. This set of compounds shows trends in their optical properties that are similar to what was observed in other vacancy-ordered systems. [122] Additionally, we have found that magnetism in these compounds deviates from the Kotani model; however, the reasons for this behavior remain unclear. Finally, we demonstrate that these A_2WX_6 compounds, which do not show strong optical emission, are compositionally distinct from the compounds produced by hydrothermal synthesis,

which do. This difference in composition is central to explaining the different observed optical properties.

3.2 Experimental Methods

3.2.1 Synthesis

All reagents were purchased from Fisher Scientific or Sigma Aldrich. With the exception of solvents, all other materials were used without further purification or modification. In the case of solvents, diethyl ether (Et_2O) and acetonitrile (MeCN) were dried using a Vacuum Atmospheres DRI-SOLV Solvent Purification system and stored over 3 Å molecular sieves prior to use. All handling of air-sensitive reagents and products was performed under anaerobic and anhydrous conditions in a nitrogen-filled glovebox.

A_2WCl_6 compounds were synthesized by combining 0.25 mmol of the appropriate *A*-cation salt (CsCl, RbCl, or CH_3NH_3Cl (MACl)) and 0.125 mmol of WCl_4 in 5 mL of acetonitrile and stirring. In the case of MA_2WCl_6, the solution changes color to a dark reddish-purple after a few hours, and the reaction is complete after stirring for 24 hours. The majority of the product forms as a microcrystalline powder; however, single crystals can be collected from the solid deposited on the sides of the vial during stirring. The powder can be washed with diethyl ether and isolated by filtration. In the case of Cs_2WCl_6 and Rb_2WCl_6, the reaction is complete after stirring for 5 days (due to the low solubility of the salts in acetonitrile). Cs_2WCl_6 is a dark orange and Rb_2WCl_6 is reddish-purple. The products form as very fine powders and no single crystals could be obtained. The powders were isolated by washing with diethyl ether and carefully decanting away the liquid phase to isolate the solid.

For the sake of comparison with the literature, we also attempted to synthesize Cs_2WCl_6 from a solvothermal synthesis in acid. In this case, the synthesis followed a modified version of the literature report.[20] 0.25 mmol of CsCl was combined with 0.125 mmol of WCl_4 and 3 mL of concentrated hydrochloric acid in a hydrothermal vessel. The vessel was heated to 160 °C for 2 days, followed by slow cooling to room temperature for 24 hours, producing bright green crystals. Single crystal X-ray diffraction reveals that the composition of these crystals is $Cs_2WO_{1.08}Cl_{4.92}$.

3.2.2 Single-crystal X-ray diffraction

Single-crystal X-ray diffraction data was collected on a KAPPA APEX II diffractometer with an APEX II CCD detector, TRIUMPH monochromator, and Mo-Kα radiation source (λ = 0.71073 Å). For moisture-sensitive samples, nitrogen was blown over the sample during data collection using an Oxford nitrogen gas cryostream system. Data collection was performed at 298 K for MA_2WCl_6 and 100 K for $Cs_2WO_{1.08}Cl_{4.92}$. Data collection and cell parameter determination were conducted using the SMART program. Integration of the data frames and final cell parameter refinement were performed using SAINT software. Absorption corrections of the data were carried out using the multi-scan method SADABS. Structure solution and refinement were performed using SHELXTL. All crystal structures are visualized using the VESTA software package. [99] Further crystallographic details can be found in Appendix D.

3.2.3 Synchrotron X-ray diffraction

High-resolution synchrotron powder X-ray diffraction data were collected at beamline 11-BM at the Advanced Photon Source at Argonne National Laboratory. The pow-

der X-ray diffraction data were analyzed using the TOPAS software suite. [36] Initial Pawley refinements [33] were performed to determine lattice parameters and peak shapes. Subsequently, Rietveld refinements were performed to determine background, zero-point error, atomic positions, and isotropic ADPs. In the case of Cs_2WCl_6, the sample contained some residual CsCl from the reaction mixture, so CsCl was included as a second phase in the refinement.

3.2.4 X-ray photoelectron spectroscopy

X-ray photoelectron spectroscopy measurements were performed using a Thermo Fisher Escalab Xi+ XPS system with a monochromated aluminum anode (1486.7 eV). Powder samples were pressed onto carbon tape and were transferred to the instrument using a homemade air-free sample holder. Since all measured samples were semiconducting, charge compensation was applied and all spectra were referenced to the C 1*s* peak of carbon at 284.5 eV. Data fitting was performed using the CasaXPS software package. For fitting of the tungsten high-resolution spectra, several constraints were imposed. The 4*f* 5/2 peak was required to have 3/4 of the area of the 7/2 peak and the same FWHM. Additionally, the two pairs of 5/2 and 7/2 peaks were required to have the same separation in binding energy.

3.2.5 Raman spectroscopy and photoluminescence measurements

Raman spectroscopy and photoluminescence measurements were performed at room temperature using a Horiba Jobin Yvon T64000 open-frame confocal microscope operating at a wavelength of 488 nm with triple monochromator and LN2-cooled CCD array detector. Filters were used to reduce the laser to 25% of its original intensity to prevent

beam damage to the samples. For air-sensitive samples, the powders were loaded into a homemade air-free cell with a fused silica window (Corning glass) inside a glovebox. Spectra were calibrated by referencing the spectrum of monocrystalline silicon, which has a peak at 521 cm^{-1}. Additionally, the spectrum of silicon inside the air-free cell was used to confirm that the use of the cell only contributes very minor peaks or changes to the baseline.

3.2.6 UV-vis spectroscopy

Absorbance spectra were obtained by measuring diffuse reflectance on a Shimadzu UV3600 UV-Vis-NIR spectrometer equipped with an integrating sphere. Samples were diluted in barium sulfate. Air-sensitive samples were transferred to the sample holder inside of the glovebox and a glass coverslip was attached to the front of the sample holder to minimize air exposure. Reflectance was converted to absorbance using the Kubelka-Munk transformation. [44]

3.2.7 Magnetic measurements and data processing

Magnetic measurements were performed on a Quantum Design MPMS3 Squid instrument. DC measurements were performed in VSM mode. Approximately 10 mg of sample was deposited inside plastic capsules purchased from Quantum Design, which was mounted in a brass sample rod. Magnetization vs temperature measurements were performed at fields of 500 Oe and 7 T between 1.8 K and 300 K. To calculate the temperature-dependent effective moment for each sample, the magnetization was converted to susceptibility (χ). For the Kotani fitting, a diamagnetic correction factor equal to $(\text{molar mass}/2) \times 10^{-6}$ was added to the susceptibility values. The effective moment

at each temperature was calculated as $2.827\sqrt{\chi T}$. For the Kotani fitting, Equations 3.1 and 3.2 for the effective moments were used for the d^1 and d^2 cases, respectively. In these equations, $x = \frac{A}{kT}$ where A represents the strength of spin-orbit coupling in cm^{-1}, k is the Boltzmann constant, and T is the temperature. For the Curie-Weiss fitting, the $1/\chi$ data was fit using Equation 3.3, where χ_0 is the diamagnetic correction to the susceptibility, T is the temperature, C is the Curie constant, and θ_{CW} is the Weiss temperature.

$$n_{eff}^2 = \frac{8 + (3x - 8)e^{\frac{-3}{2}x}}{x(2 + e^{\frac{-3}{2}x})} \tag{3.1}$$

$$n_{eff}^2 = \frac{3\{\frac{5}{2}x + 15 + (\frac{x}{2} + 9)e^{-x} - 24e^{\frac{-3}{2}x}\}}{x(5 + 3e^{-x} + e^{\frac{-3}{2}x})} \tag{3.2}$$

$$\chi^{-1} = \frac{T - \theta_{CW}}{\chi_0(T - \theta_{CW}) + C} \tag{3.3}$$

3.3 Results and Discussion

The compounds MA_2WCl_6, Rb_2WCl_6, and Cs_2WCl_6 were prepared by combining a stoichiometric ratio of the *A*-cation chloride salt and WCl_4 in anhydrous acetonitrile and stirring for several days at room temperature, as described in the Experimental Methods. Due to the air- and moisture-sensitivity of these compounds, they were prepared and stored in a nitrogen-filled glovebox. In the case of MA_2WCl_6, maroon single crystals could be obtained directly from the reaction mixture. For Rb_2WCl_6 and Cs_2WCl_6, the compounds were insoluble in organic solvents and precipitated as fine reddish-orange and purple powders, respectively.

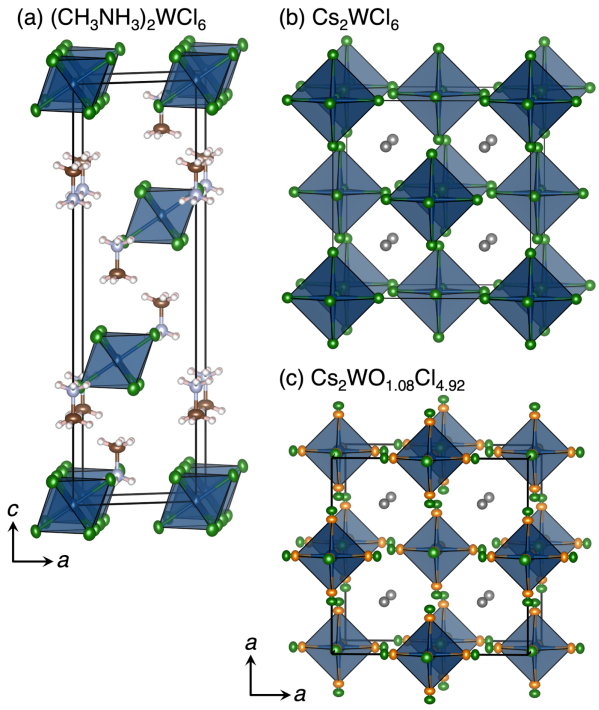

Figure 3.1: (a) Single crystal structure of MA_2WCl_6 with thermal displacement ellipsoids depicted at 50 % probabilty. (b) Structure of Cs_2WCl_6 as determined from synchrotron XRD. (c) Single crystal structure of $Cs_2WO_{1.08}Cl_{4.92}$ with thermal displacement ellipsoids depicted at 50 %. Single-crystal X-ray diffraction and refinements performed by Dr. Guang Wu and Dr. Greggory Kent.

The crystal structures of MA_2WCl_6 and Cs_2WCl_6 as determined from single-crystal X-ray diffraction (XRD) and synchrotron XRD, respectively, are shown in Figure 3.1. The compound MA_2WCl_6 crystallizes in the trigonal space group $R\bar{3}m$. Notably, we believe this to be the first true hybrid vacancy-ordered halide perovskite structure based on tungsten. This compound is structurally analogous to MA_2RuCl_6, [8] and similarly to this compound, the octahedra are very regular, despite not being constrained by symmetry. The unique bond angles are 90.44° and 89.56° and W–Cl bond distances are all 2.3782(18) Å. The structure type is stabilized by hydrogen bonding, with a minimum N···Cl distance of 3.447(8) Å. The alignment of the methylammonium cations in this structure maximizes their hydrogen bonding interactions of the NH_3^+ group with the Cl^- anions. Due to the larger size of tungsten, its unit cell is slightly larger than that of the ruthenium analogue, with a = 7.1125(14) Å and c = 21.975(6) Å. Synchrotron X-ray diffraction data, showing that the single-crystal structure is consistent with the structure of the bulk powder, is shown in Appendix D.

The compounds Rb_2WCl_6 and Cs_2WCl_6 were difficult to recrystallize due to low solubility in organic solvents, so the structures were determined by synchrotron X-ray diffraction of the powders, shown in Figure 3.2(a) and (b). For these compounds, which both crystallize in the space group $Fm\bar{3}m$, we found that their structures are similar, but not identical, to what has been reported in the literature. [124] Pawley and Rietveld refinements indicate that Rb_2WCl_6 has a cubic cell parameter of 10.02(1) Å, and Cs_2WCl_6 has a cell parameter of 10.326(2) Å. The lattice parameter for Cs_2WCl_6 is larger than the previously-reported value of 10.245(1) Å determined from single crystal diffraction,[124] and the value of 10.27 Å estimated from powder Debye X-ray photographs. [123] One potential explanation for this discrepancy is simply the different diffraction techniques used in the structure determinations. A second possibility is

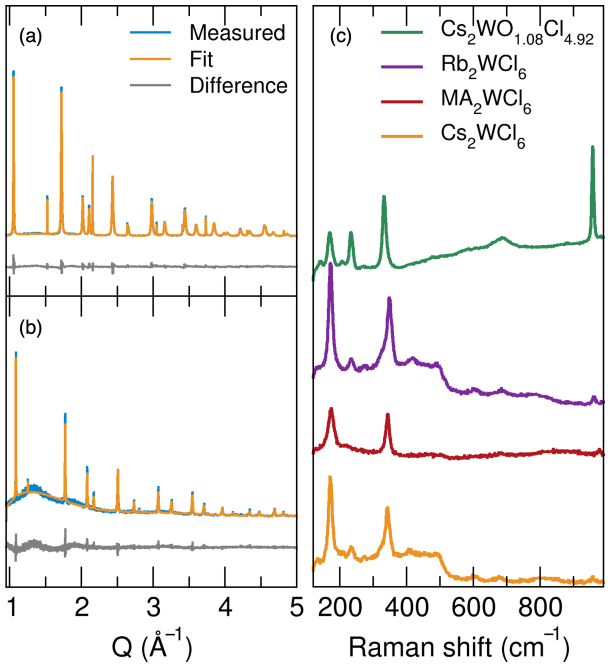

Figure 3.2: 11-BM synchrotron X-ray diffraction data, fit, and difference for (a) Cs_2WCl_6, $R_{wp} = 7.27\,\%$, $R_p = 5.97\,\%$ and (b) Rb_2WCl_6 $R_{wp} = 8.92\,\%$, $R_p = 7.26\,\%$. The broad hump in the diffraction pattern between $Q = 1.0\,\text{Å}^{-1}$ and $2.0\,\text{Å}^{-1}$ is due to the kapton sample holder. (c) Raman spectra for A_2WCl_6 compounds and $Cs_2WO_{1.08}Cl_{4.92}$.

that the differences in cell parameters could reflect differences in composition due to the use of different synthetic strategies.

To further explore the relationship between the synthesis method and the properties of the A_2WCl_6 compounds, we attempted to synthesize Cs_2WCl_6 using a hydrothermal method reported in the literature. [20] This synthesis produces bright green cuboctahedral crystals, and a single-crystal XRD refinement for these crystals gives a cell parameter of 10.23(2) Å. Furthermore, this compound is stable under ambient conditions, which contrasts with the air- and moisture-sensitivity of the other synthesized A_2WX_6 compounds. Suspecting that there must be a difference in composition between the hydrothermal product and the compounds prepared under inert conditions, we performed Raman spectroscopy, the results of which are shown in Figure 3.2(c). In the case of the hydrothermal compound, we observe strong peaks at 171 cm^{-1}, 235 cm^{-1}, 334 cm^{-1}, and 960 cm^{-1}. These are similar to the values reported previously for this hydrothermal product. [20] Considering the spectrum of the Cs_2WCl_6 prepared under dry and anaerobic conditions, we can see similar features at lower wavenumbers, with strong peaks at 169 cm^{-1}, 235 cm^{-1}, and 345 cm^{-1}, and only a very small peak at 960 cm^{-1}. Similarly, for Rb_2WCl_6, there are strong peaks at 173 cm^{-1}, 236 cm^{-1}, and 348 cm^{-1}, and a weak peak at 960 cm^{-1}. MA_2WCl_6 has strong peaks at 174 cm^{-1} and 344 cm^{-1} and a small peak at 975 cm^{-1}. Based on symmetry considerations, the $Fm\bar{3}m$ structure should have only three Raman-active modes and the $R\bar{3}m$ structure should have two modes. [41–43] Furthermore, previous literature on tungsten compounds suggests that the peak at 960 cm^{-1} should be attributed to the W=O bond in a $WOCl_5^{2-}$ distorted octahedron, while the three intense lower energy peaks are due to the motions of the W−Cl bonds. [125] Overall, the Raman spectra suggest that the hydrothermal sample contains a large number of W=O bonds, while the samples

prepared under inert conditions contain very few.

Based upon our analysis of the Raman spectra, we developed a new structural model of the hydrothermal compound, which is shown in Figure 3.1(c). In this model, an oxygen position was added to the structure in between the W and Cl positions such that the W–O bond distance is 1.90(8) Å and the W–Cl bond distance is 2.369(7) Å. The occupancies of the O and Cl positions were then refined and constrained to add up to one, based on the assumption that each W atom should have six-fold coordination. Using this model, we have determined the composition of the hydrothermal product to be $Cs_2WO_{1.08}Cl_{4.92}$. We believe this to be a reliable estimate, as the estimated standard deviation on the oxygen content in the formula unit is 0.07 (i.e. 1.08(7)). This suggests that the majority of octahedra in the structure will have a composition of $[WOCl_5]^{2-}$, but that there may also be some with a composition of $[WO_2Cl_4]^{2-}$. The presence of oxygen in this compound also explains observations that the hydrothermal product tends to have a smaller cell parameters, due to the higher oxidation state of W in the oxyhalide octahedra and the short W–O bonds. We also note that a similar compound was previously reported with a composition of Cs_2WOCl_5; [125] however, a full single-crystal structure solution has not been obtained until now. After examining a number of samples prepared using this hydrothermal method, we have found that the oxygen content, as determined by this type of refinement, can vary between 1 and 1.5 oxygen per formula unit. In addition to the Raman data and cell parameter trends, a clear justification for the use of our model is that if the structure is refined with the incorrect composition of Cs_2WCl_6 the *R*-factor is 3.53%, while the *R*-factor for $Cs_2WO_{1.08}Cl_{4.92}$ is 2.54%. This result is consistent with previous findings that a $M{=}O$ bond can closely resemble a $M{-}Cl$ bond in single crystal diffraction and refinements of disordered compounds, [126] and in this case leads to a large reduction in *R*-factor.

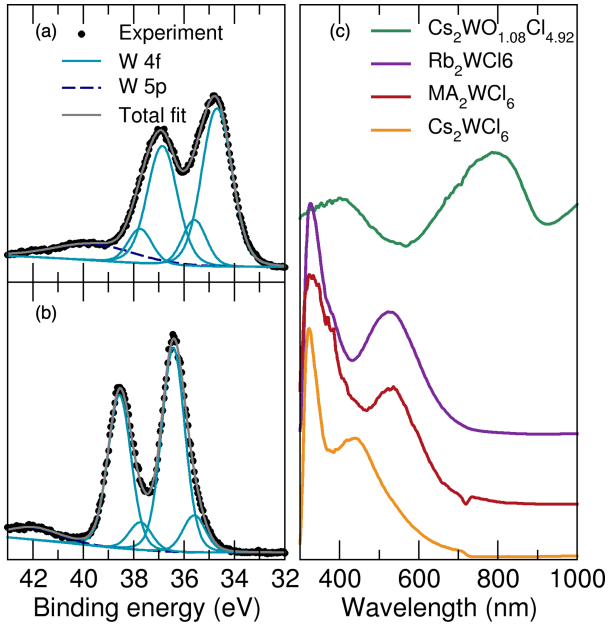

Figure 3.3: XPS spectra for the W $4f$ and $5p$ regions of (a) Cs_2WCl_6 and (b) $Cs_2WO_{1.08}Cl_{4.92}$. (c) Kubelka-Munk transformed UV-vis spectra for A_2WCl_6 compounds and $Cs_2WO_{1.08}Cl_{4.92}$.

Given the fact that Cs_2WCl_6 and $Cs_2WO_{1.08}Cl_{4.92}$ appear similar in diffraction data, it was important to further evaluate the composition of these samples. High-resolution XPS spectra, shown in Figure 3.3(a) and (b), were examined to determine the oxidation state of W in each sample. Additionally, we compared the XPS survey scans for Cs_2WCl_6 and $Cs_2WO_{1.08}Cl_{4.92}$ (shown in Appendix D) to verify that Cs_2WCl_6 contains a higher proportion of Cl, while $Cs_2WO_{1.08}Cl_{4.92}$ contains more O. All of the W XPS spectra examined showed similar features, with two sets of doublets corresponding to the $4f$ photoelectron peaks, and one peak at higher binding energy corresponding to the $5p$ photoelectron peak. For Cs_2WCl_6, the most intense $4f_{\frac{7}{2}}$ and $4f_{\frac{5}{2}}$ photoelectron peaks, which we attribute to W^{4+}, occur at 34.7 eV and 36.9 eV. These values are similar to those for Rb_2WCl_6 (34.7 eV and 36.9 eV) and MA_2WCl_6 (34.6 eV and 36.8 eV). The W high-resolution spectra for these compounds are displayed in Appendix D. In the case of $Cs_2WO_{1.08}Cl_{4.92}$, the most intense $4f$ peaks, which we attribute to W^{5+}, occur

at 36.4 eV and 38.6 eV. For all the samples, an additional set of W $4f$ photoelectron peaks is present, in which the $4f_{\frac{7}{2}}$ peak is observed at 35.6 eV and the $4f_{\frac{5}{2}}$ at 37.7 eV. Given that these peaks are observed with similar intensities and locations in all compounds, we attribute them to the presence of surface oxidation in the samples. This oxidation may also provide an explanation for the weak peaks at 960 cm^{-1} observed in the Raman spectra of the A_2WX_6 compounds.

The UV-vis absorbance data for the A_2WCl_6 compounds is shown in Figure 3.3(c). As expected from the appearance of the two compounds, the absorbance profiles of MA_2WCl_6 and Rb_2WCl_6 are very similar, with both showing absorbance maxima at 530 nm and 327 nm. Similarly to the analogous ruthenium compounds [122] and previous literature reports [123], the absorption maxima for Cs_2WCl_6 are shifted to higher energy, and occur at 440 nm and 323 nm. This is because the larger Cs^+ cations decrease the interactions between the $[WCl_6]^{2-}$ octahedra, leading to a less-disperse valence band and higher-energy absorption onset for this compound. The lower-energy maxima in all the A_2WCl_6 compounds are attributed to $d-d$ transitions, while the higher-energy features are ligand-to-metal charge transfer (LMCT) transitions. [123] The spectra for the A_2WCl_6 compounds are clearly different from the spectrum of $Cs_2WO_{1.08}Cl_{4.92}$, which shows two broad peaks with maxima at approximately 400 nm and 800 nm. Using the molecular-orbital diagram developed by Gray *et. al.* for the molybdenyl ion, [127, 128] we can assign these features to the d_{xy} to $d_{x^2-y^2}$ and d_{xy} to d_{xz}, d_{yz} transitions, respectively. Here, the $[WOCl_5]^{2-}$ unit is non-centrosymmetric, therefore enhancing the intensity of the $d-d$ transitions compared to those in A_2WCl_6. Additionally, some higher-energy absorption features are visible for wavelengths shorter than 400 nm. These likely correspond to the d_{xy} to d_{z^2} and LMCT transitions.

We also confirmed that $Cs_2WO_{1.08}Cl_{4.92}$ displays intense photoemission with a max-

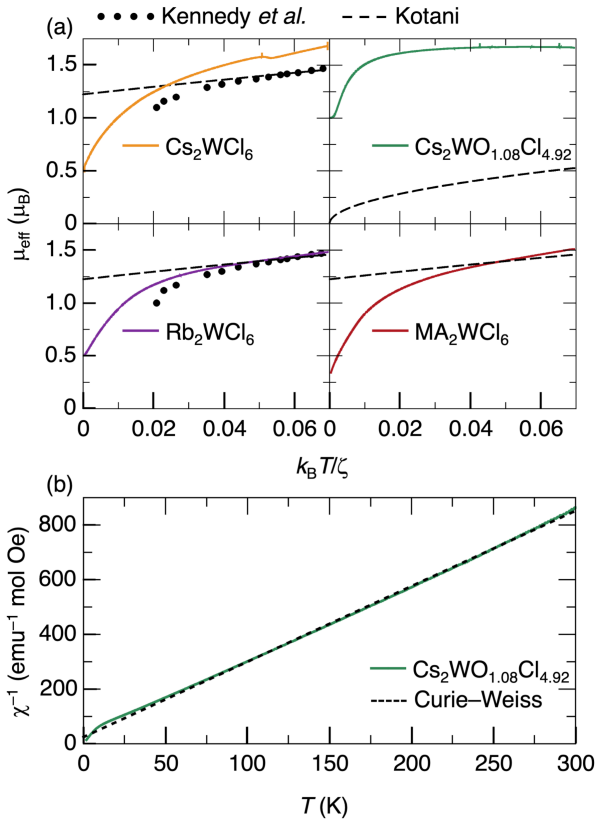

Figure 3.4: (a) Temperature dependence of the effective moment of the A_2WCl_6 compounds and $Cs_2WO_{1.08}Cl_{4.92}$, as well as comparison with previous reports and theory. The spin-orbit coupling parameter ζ is assumed to be 3000 cm^{-1}. (b) Curie-Weiss fit of the magnetic data for $Cs_2WO_{1.08}Cl_{4.92}$. The Weiss temperature is -8.92 K and the effective moment is 1.70 μ_B.

imum around 900 nm under 488 nm laser excitation. In contrast, the A_2WCl_6 compounds do not emit under these conditions. Based on the difference in the optical properties, it is clear that the substitution of O for Cl plays a key role in near-IR emission. Again using the molecular-orbital diagram [127, 128] we suggest that the emission arises from a $d-d$ transition. This explanation for the optical properties differs from that in previous work, which attributes the luminescence to self-trapped excitons which induce a large Stokes shift. [20]

Earlier works on the A_2WCl_6 compounds indicate that their magnetic behavior is not

consistent with the Kotani model, and suggest that this deviation originates from antiferromagnetic interactions. [123] Therefore, it was of interest to determine whether our compounds displayed this same behavior. Figure 3.4 demonstrates that our measurements on Cs_2WCl_6 and Rb_2WCl_6 are similar to this previously-reported data. Additionally, none of the data can be adequately fit to the Kotani model for d^2 ions. [50] This model is used to account for the influence of the orbital angular momentum on the temperature-dependence of the effective magnetic moment for transition metal ions in an octahedral field. By fitting magnetic data to the appropriate Kotani equation, the strength of spin-orbit coupling in a compound can be determined. Here, we have assumed a spin-orbit coupling constant of 3000 cm^{-1}, which is similar to the constant that is predicted for a free W^{4+} ion. [129] However, for any value chosen for the spin-orbit coupling, it is not possible to fit the data, because at low temperatures the observed moment is significantly lower than theoretically predicted. Regardless of spin-orbit coupling constant, all Kotani d^2 ions should converge to a moment of 1.22 μ_B at 0 K, [50] while our A_2WCl_6 compounds all show low-temperature moments of approximately 0.5 μ_B. Therefore, it is reasonable to attribute the discrepancy to antiferromagnetic interactions. However, the closest W–W distance in these structures is 7.088 Å in Rb_2WCl_6, so we do not believe that there could be direct antiferromagnetic exchange between the W atoms. Additionally, we emphasize that the discrepancy between theory and experiment does not appear to be due to the onset of an antiferromagnetic transition, as the curvature of the lines describing the effective moments for theory and experiment are different even at intermediate temperatures. Works on related compounds have hypothesized that antiferromagnetic interactions could be mediated by the delocalization of unpaired electrons onto the chloride ligands; [130] however, further study is required to determine the precise mechanism of this interaction and whether this is the case in these compounds.

For comparison, we also show the magnetic behavior of the $Cs_2WO_{1.08}Cl_{4.92}$ compound and plot it with the Kotani model for a d^1 metal. In this case the discrepancy between theory and experiment is expected, because the $WOCl_5^{2-}$ ion does not have ideal octahedral symmetry. The lowering of symmetry quenches the orbital angular momentum, which should lead to an effective moment that is close to the spin-only value for a single unpaired electron. [130, 131] A Curie-Weiss fit of the magnetic data for this compound, shown in Figure 3.4(b), gives a Weiss temperature of -8.92 K, a Curie constant of 0.362 μ_B^2, and an effective moment of 1.70 μ_B. As expected, this is close to the theoretical moment for a single unpaired electron, which is 1.73 μ_B.Therefore, magnetic data provides another method of differentiating between the pure chloride materials and the oxychlorides

3.4 Conclusion

In summary, the vacancy-ordered double perovskites A_2WCl_6 (A = MA ($CH_3NH_3^+$), Rb, and Cs) and the oxyhalide $Cs_2WO_{1.08}Cl_{4.92}$ have been studied. MA_2WCl_6 constitutes the first report of a hybrid W halide with a perovskite-related structure. We have also shown that Cs_2WCl_6 and $Cs_2WO_{1.08}Cl_{4.92}$ closely resemble one another in diffraction data, but can be distinguished *via* spectroscopy, magnetism, and even by eye. For example, the appearance of an intense peak in the Raman spectrum around 960 cm^{-1} is a clear sign of W=O bonds. $Cs_2WO_{1.08}Cl_{4.92}$ has two broad absorption maxima in the visible range and shows intense photoluminescence in the near-IR regime under 488 nm laser excitation. The incorporation of O into this compound is significant to its optical properties, and we believe that it is the splitting of the *d* orbitals, due to the lower symmetry of the $WOCl_5^{2-}$ ion, that gives rise to the distinct absorption features and bright

emission. Interestingly, the structure and optical properties of similar compounds have previously been studied, [131, 132] and Cs_2NbOF_5 has also been identified as a strong emitter with a large Stokes shift, attributed to a self-trapped state.[133] Therefore, it may be worthwhile to re-examine the optical properties of these related compounds in future works. Additionally, we note that the results reported here for the differences between the compounds Cs_2WCl_6 and $Cs_2WO_{1.08}Cl_{4.92}$ should also apply to the molybdenum-based versions. We have also attempted to synthesize the pure A_2MoCl_6 compounds using a number of methods; however, we find that the oxychlorides will always be preferentially formed. Therefore, we believe that the materials reported as Cs_2MoCl_6 by Liu *et. al* are probably $Cs_2MoO_xCl_{6-x}$ Finally, the magnetic behavior of Rb_2WCl_6 and Cs_2WCl_6 are similar to those reported by Kennedy *et. al.*, [123] but the temperature-dependence of the effective magnetic moment cannot be explained using the Kotani model and remains an open challenge which we plan to explore in future works.

Chapter 4

Understanding the Near-IR Luminescence of Molybdenum and Tungsten Oxyhalides

Materials with near-IR luminescence are highly desirable for applications including communications and biomedical imaging. The most well-known materials with this property rely on careful doping of host lattices with rare-earth elements or transition metals. However, recently, another class of materials with intrinsic near-IR emission has been reported. The compositions of these materials were initially described as Cs_2MoCl_6 and Cs_2WCl_6, but further investigation has revealed them to be $Cs_2MoO_xCl_{6-x}$ and $Cs_2WO_xCl_{6-x}$, where $1 < x < 2$. This difference in composition entails a different coordination environment and oxidation state for the molybdenum and tungsten centers. Therefore, in this work, we reconsider the mechanism for near-IR emission in

At the time of publication, the contents of this chapter were in preparation for submission as E. E. Morgan, S. Panuganti, G. T. Kent, A. Zohar, A. Brumberg, A. Mikhailovsky, M. G. Kanatzidis, R. D. Schaller, A. K. Cheetham, and R. Seshadri, Understanding the Near-IR Luminescence of Molybdenum and Tungsten Oxyhalides.

these materials. We demonstrate that the luminescence is actually due to the unique d-orbital splitting caused by the presence of oxygen in the distorted $[MOX_5]^{2-}$ octahedra. Furthermore, the fine structure in the emission spectra at low temperatures is due to vibronic coupling to the Mo=O and W=O bond stretches. This interpretation of the emission spectra provides an explanation for the temperature-dependence of the luminescence and suggests how this desirable emission can be realized and manipulated.

4.1 Introduction

Vacancy-ordered double perovskites, having the general formula A_2MX_6, where A is a monovalent cation, M is a metal in the 4+ oxidation state, and X is a halide anion, are a popular area of study due to their tunable and desirable optical properties. [14] For example, doping of compounds such as Cs_2ZrCl_6 [134, 135] and Cs_2SnCl_6 [136, 137] gives rise to useful properties such as bright white-light emission and near-IR luminescence. Near-IR luminescence is particularly sought-after because of its potential utility in applications ranging from food inspection and biomedical imaging to communication. Unfortunately, the fact that most near-IR emission is achieved by doping limits the brightness of emission and makes it difficult to predict new compositions for these applications. [138] Therefore, it was novel and somewhat surprising that Cs_2WCl_6 and Cs_2MoCl_6 were reported as materials with bright near-IR emission which did not require doping or other structural modifications. When these compounds are excited in the visible range, they show broad emission between 900 nm and 1300 nm, and these materials are both solution processable and highly stable. Additionally, it was demonstrated that they could be used to make prototype near-IR imaging devices. [20]

Although the initial results presented for Cs_2WCl_6 and Cs_2MoCl_6 were exciting in

terms of performance, there were some aspects of the report that raised questions about the composition of these materials and therefore the mechanism of their luminescence. For example, the reported Raman spectra for these compounds contained more peaks than would be expected for crystals with $Fm\bar{3}m$ symmetry. Additionally, the luminescence was reported to occur through absorption by defect states and several self-trapped excitons with distinct energies. However, the compounds appeared to be highly crystalline and the nature of the defect states and distortions associated with the self-trapped excitons was unclear.

Subsequent work on these compounds by the present authors have revealed that the compounds reported have true compositions of $Cs_2MoO_xCl_{6-x}$ and $Cs_2WO_xCl_{6-x}$, where $1 < x < 2$. These compounds were previously reported in the literature, [125, 130] but their luminescent properties were not known. Additionally, in our previous work focusing on the tungsten-based vacancy-ordered perovskites, we hypothesized that the observed excitation and emission spectra could be explained using a molecular-orbital diagram for the molybdenyl ion. [127, 128] More specifically, the absorption between 400 nm and 500 nm and the emission at 900 nm to 1300 nm appeared to correspond to two distinct *d*-to-*d* transitions in these materials, explaining the large difference in energy between the two. However, at the time, we had not investigated the temperature-dependence of the luminescence or determined the origin of the fine structure observed at low temperatures. Therefore, in this work, we address both of these points in order to provide additional evidence for our hypothesis. We also show that the behavior observed in the chlorides is present in the bromide compositions, suggesting that other oxyhalide compounds may make good near-IR emitters. Additionally, while the identity of the halide anion can be used to tune the absorption of light in these materials, the emission features are strongly influenced by the character of the *M*=O bond. Therefore,

the present work highlights how to manipulate the absorption and emission energies of other potential oxyhalide-based near-IR emitters.

4.2 Experimental Methods

4.2.1 Synthesis of $Cs_2WO_{1.3}Cl_{4.7}$

0.25 mmol of CsCl and 0.125 mmol WCl_4 were combined in 3 mL of concentrated hydrochloric acid in the PTFE liner of a 23 mL Parr hydrothermal vessel. The vessel was heated to 160 °C for 2 days, followed by slow cooling to room temperature. The green crystals were separated from the hydrochloric acid and washed with a small amount of ethanol.

4.2.2 Synthesis of $Cs_2MoO_{1.2}Cl_{4.8}$ and $Cs_2MoO_{1.6}Br_{4.4}$

0.25 mmol of CsCl and 0.125 mmol $MoCl_5$ were combined in 3 mL of concentrated hydrochloric acid (in the case of the oxychloride) or hydrobromic acid (in the case of the oxybromide) in the PTFE liner of a 23 mL Parr hydrothermal vessel. The vessel was heated to 160 °C for 2 days, followed by slow cooling to room temperature. The crystals were separated from the acid and washed with a small amount of ethanol. In the case of the chloride, the crystals were bright green. In the case of the bromide, the crystals were dark red.

4.2.3 Powder X-ray diffraction and Rietveld refinements

Powder X-ray diffraction (PXRD) measurements were performed on a Panalytical Empyrean powder diffractometer in reflection mode with a Cu-Kα radiation source. Structure and phase-purity were confirmed using the TOPAS software package. [36]

4.2.4 Single crystal X-ray diffraction and refinements

Single-crystal X-ray diffraction data was collected on a KAPPA APEX II diffractometer with an APEX II CCD detector, TRIUMPH monochromator, and Mo-Kα radiation source ($\lambda = 0.71073$ Å). Structure refinements were performed by Dr. Greggory Kent in the SHELXTL software package. Crystal structures were visualized using the VESTA software package. [99]

4.2.5 Raman spectroscopy

Raman spectroscopy was performed using a Horiba Jobin Yvon T64000 open-frame confocal microscope operating at a wavelength of 488 nm with monochromator and LN2-cooled CCD array detector. Calibration was confirmed by referencing the spectrum of monocrystalline silicon, which has a peak at 521 cm^{-1}. For variable-temperature measurements, samples were pressed onto copper tape and sealed inside a vacuum chamber, where temperature was controlled using a nitrogen flow with a Lake Shore Cryotronics temperature controller. The sample was allowed to equilibrate at each temperature point for 15 minutes prior to data collection.

4.2.6 UV-vis spectroscopy

Absorbance spectra were obtained by measuring diffuse reflectance on a Shimadzu UV3600 UV-Vis-NIR spectrometer equipped with an integrating sphere. Samples were diluted in barium sulfate. Reflectance was converted to absorbance using the Kubelka-Munk transformation. [44]

4.2.7 Near-IR fluorimetry

Samples were encapsulated in poly(methyl methacrylate) (PMMA) and mounted on a glass slide. A PTI Quantamaster fluorimeter equipped with a near-IR detection system and a 950 nm long-pass filter was used for all measurements. For the excitation scan, the emission at 1000 nm was monitored while scanning the excitation wavelength between 350 nm and 800 nm. The final spectra were obtained by normalizing the raw data by the intensity of the lamp for this spectral range.

4.2.8 Photoluminescence measurements

For the experiments conducted using 400 nm excitation, temperature-dependent and time-resolved photoluminescence experiments were performed using the 800 nm output of a Ti/sapphire amplifier with 2 kHz repetition rate and 35 fs pulse width. Samples were photoexcited with 400 nm front-facing excitation. The incident pulse was generated with a beta barium borate (BBO) crystal for frequency-doubled output of the laser. Temperature-dependent photoluminescence spectra of powder samples were collected in a 4 K closed-cycle cold-finger cryostat under a base pressure of 1×10^{-7} torr. Samples were equilibrated for 5 minutes at each temperature point prior to data

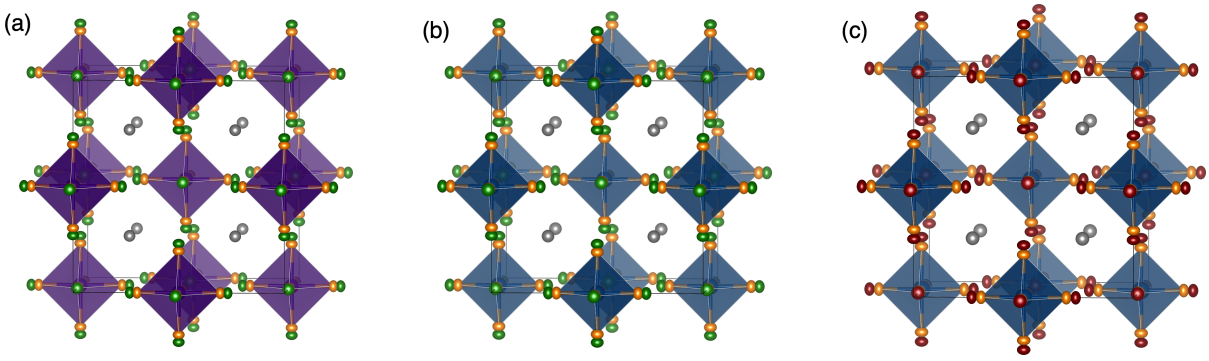

Figure 4.1: Single-crystal XRD structures for (a) $Cs_2WO_{1.3}Cl_{4.7}$ (b) $Cs_2MoO_{1.2}Cl_{4.8}$ (c) $Cs_2MoO_{1.6}Br_{4.4}$. Structures determined by Dr. Greggory Kent.

collection. Spectra were collected using a 100 μW near-IR detector with a range of 800 nm to 1300 nm. Time-resolved photoluminescence lifetimes were collected with time-correlated single photon counting electronics using a CCD detector. The cryostat details for temperature-dependent lifetime measurements are the same as written above.

For analysis of the photoluminescence spectra, the abscissa was converted to units of eV using the standard relation $E = hc/\lambda$. In order to account for the difference between wavelength- and energy-dependent spectra, the ordinate was transformed using Equation 4.1. Gaussian peak-fitting was performed using the Fityk software package. [139]

$$I_E = I_\lambda \lambda^2 (hc)^{-1} \tag{4.1}$$

4.3 Results and Discussion

The crystal structures of the compounds studied are shown in Figure 4.1. These compounds all crystallize in the space group $Fm\bar{3}m$, and their compositions based on single-crystal XRD refinements are $Cs_2WO_{1.32}Cl_{4.68}$, $Cs_2MoO_{1.20}Cl_{4.80}$, and $Cs_2MoO_{1.602}Br_{4.398}$.

Refined composition	$Cs_2WO_{1.32}Cl_{4.68}$	$Cs_2MoO_{1.20}Cl_{4.80}$	$Cs_2MoO_{1.602}Br_{4.398}$
Lattice parameter (Å)	10.208(3)	10.216(5)	10.613(7)
M-*X* bond length (Å)	2.369(5)	2.367(4)	2.516(3)
M-O bond length (Å)	2.01(7)	1.97(6)	2.06(4)
R-factor without oxygen	3.27%	3.14%	7.56%
R-factor with oxygen	2.40%	2.20%	3.13%

Table 4.1: Details of single crystal structures.

For convenience, these compositions will be referred to in the rest of this work as $Cs_2WO_{1.3}Cl_{4.7}$, $Cs_2MoO_{1.2}Cl_{4.8}$, and $Cs_2MoO_{1.6}Br_{4.4}$. It is possible to refine the crystal structures to have the incorrect compositions of Cs_2WCl_6, Cs_2MoCl_6, and Cs_2MoBr_6 and obtain satisfactory *R*-factors. However, when an oxygen position is included in the refinements and the occupancy of the oxygen and halide sites are constrained to add up to one, the improvements in the *R*-factors are significant. For example, in $Cs_2MoO_{1.2}Cl_{4.8}$, the *R*-factor without oxygen is 3.14%, while with oxygen it is 2.20%. Further details can be found in Table 4.1. Phase purity and lattice parameter trends were also validated using powder X-ray diffraction. Additional details of the powder and single crystal diffraction data can be found in Appendix E. An additional important observation about these compounds is that the refined oxygen content can vary sample-to-sample, even when the same synthesis conditions are used. For the chlorides, the refined oxygen coefficient tends to be between 1 and 1.5. For the bromide, there is usually a larger amount of oxygen, generally between 1.5 and 2. We have also attempted to synthesize the tungsten-based oxybromide, but the crystals were of poor quality, making the composition difficult to determine. Therefore this sample was excluded from this study.

Room temperature Raman spectra using an excitation wavelength of 488 nm are shown in Figure 4.2(a) and (b). First considering the spectra for $Cs_2WO_{1.3}Cl_{4.7}$ and $Cs_2MoO_{1.2}Cl_{4.8}$, we find that they are qualitatively quite similar due to similarities

in composition and metal-ligand bond lengths. In these compounds, the majority of the octahedra are expected to have a composition of $[MOCl_5]^{2-}$, which has a point group symmetry of C_{4v}. In this case, group theory predicts that there can be up to 11 Raman-active modes observed, in contrast to the 3 modes expected for O_h symmetry. In the low-frequency region for $Cs_2WO_{1.3}Cl_{4.7}$ there are peaks at 170.5, 233.8, and 333.6 cm^{-1}. In $Cs_2MoO_{1.2}Cl_{4.8}$ similar peaks are located at 173.4, 231.9, and 325.0 cm^{-1}. Based on their similarity to the modes present in other vacancy-ordered systems, these features can be assigned to the bending, asymmetric stretching, and symmetric stretching modes of the $M-Cl$ bonds. In other cases where local octahedral symmetry is broken, such as in *X*-site alloying in Cs_2TeX_6, the additional peaks which correspond to this lowering in symmetry are found between 100 cm^{-1} and 300 cm^{-1}. [140] However, in the case of the compounds studied here, the additional peaks appear at significantly higher energies due to the difference in the strength of the $M=O$ bonds compared to *M-X* bonds. These higher energy peaks are observed at 958.2 cm^{-1} in $Cs_2WO_{1.3}Cl_{4.7}$ and 953.0 cm^{-1} in $Cs_2MoO_{1.2}Cl_{4.8}$ and correspond to the $M=O$ bond stretches.

In contrast to the chloride compositions, the peaks for $Cs_2MoO_{1.6}Br_{4.4}$ are relatively weak and broad in the low-frequency region and there are additional peaks which do not appear in the chloride compositions. This behavior can be attributed to the relatively weaker $Mo-Br$ bonds and the fact that this composition contains more oxygen compared to the chlorides. In $Cs_2MoO_{1.6}Br_{4.4}$ we expect that, in addition to octahedra with the composition $[MoOBr_5]^{2-}$, there will also be more octahedra with of the type $[MoO_2Br_4]^{2-}$ compared to the chloride compositions. Although there is no crystal structure reported for the compound $Cs_2MoO_2Br_4$, literature on related compounds suggests that the two oxygens in the octahedra will be arranged in a *cis* configura-

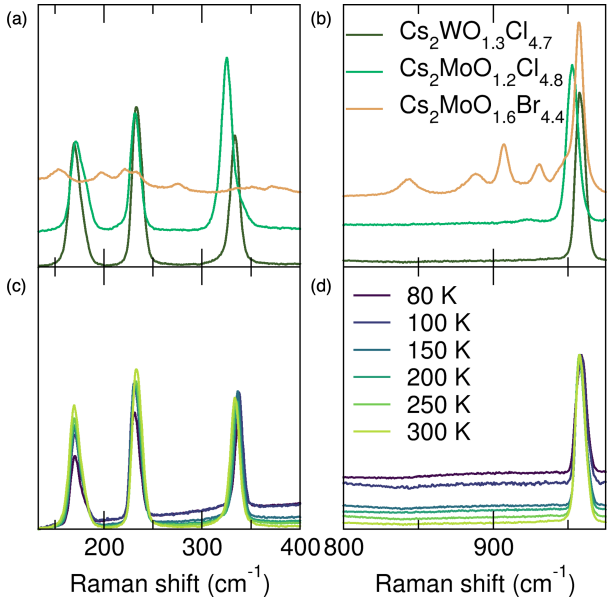

Figure 4.2: (a) Low-frequency region of the room temperature Raman spectra and (b) High-frequency region of the room temperature Raman spectra for $Cs_2WO_{1.3}Cl_{4.7}$, $Cs_2MoO_{1.2}Cl_{4.8}$, and $Cs_2MoO_{1.6}Br_{4.4}$. (c) Low-frequency region of the variable-temperature Raman spectra and (d) High-frequency region of the variable-temperature Raman spectra for $Cs_2WO_{1.3}Cl_{4.7}$.

tion. [141] Therefore, the expected point group for these octahedra is C_{2v}, which can contribute up to 15 additional Raman-active modes, thus explaining why several additional peaks are visible in both the low- and high-frequency regions of the spectrum. The peaks at lower energies, which are weak and broad, should correspond to motions of the Mo−Br bonds, while the peaks at higher energies, which are sharper and more intense correspond to motions of the Mo=O bonds.

We have also examined the variable-temperature Raman spectra between 80 K and 300 K for $Cs_2WO_{1.3}Cl_{4.7}$ in order to check for phase-transitions or other changes in the vibrational spectrum. As shown in Figure 4.2(c) and (d), the Raman spectra show only small changes, indicating that the crystal structure remains nearly the same over this range of temperatures. Closer analysis of the data does reveal some interesting temperature-dependent trends, as shown in Figure 4.3. First considering the lowest

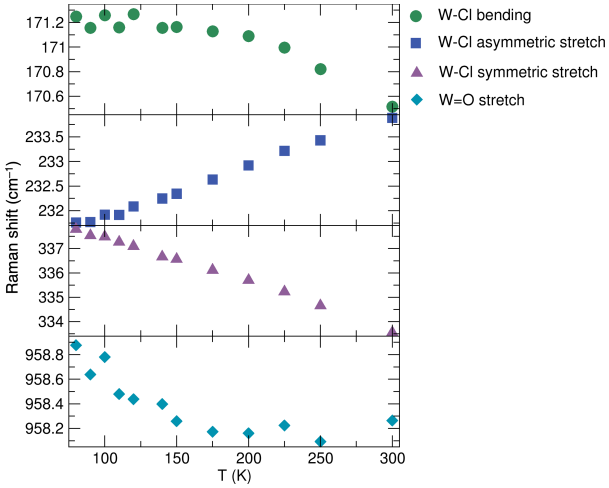

Figure 4.3: Temperature-dependence of the Raman shifts for $Cs_2WO_{1.3}Cl_{4.7}$.

energy peak, which is associated with bending modes of the W−Cl bonds, the position of this peak remains relatively constant until approximately 150 K, after which it begins to decrease in energy. Next, for the peak associated with the asymmetric stretching modes, we find that this peak increases linearly in energy with temperature. In contrast, the energy of the peak for the symmetric stretch decreases linearly with temperature. Finally, for the peak associated with the W=O stretch, the energy of this peak decreases between 80 K and 150 K, and then remains relatively constant at temperatures greater than 150 K. These trends will be discussed in further detail in the context of the variable-temperature optical data.

The absorption spectra for all compounds are shown in Figure 4.4 (a). In order to clarify the origin of absorption features in these compounds, we have reproduced aspects of a molecular-orbital diagram developed by Gray *et. al.* for the $[MOX_5]^{2-}$ ions [127, 128] in Figure 4.4(b). First, we consider the lower energy transition, where the absorption onset appears at approximately 920 nm in the tungsten-based compound and at approximately 930 nm in the molybdenum-based compositions. This absorption was previously-reported to arise from sub-bandgap emission due to defect states

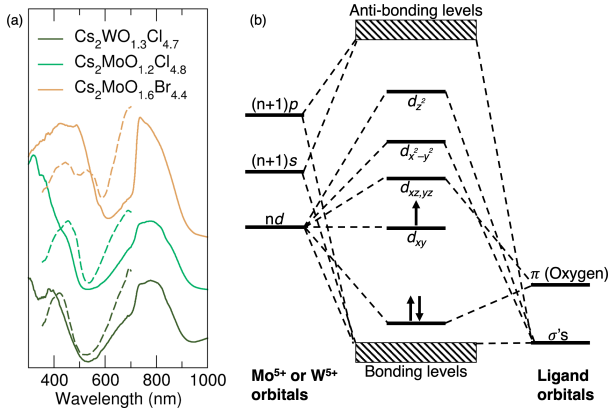

Figure 4.4: (a) UV-vis absorption spectra (solid traces) and fluorimetry excitation scans (dashed traces) for $Cs_2WO_{1.3}Cl_{4.7}$, $Cs_2MoO_{1.2}Cl_{4.8}$, and $Cs_2MoO_{1.6}Br_{4.4}$. (b) Simplified version of the molecular-orbital diagram developed by Gray *et. al.* [127]

[20]; however, considering past work on the spectroscopy of the $[MOX_5]^{2-}$ ions, it is clear that this feature is actually due to a transition from the d_{xy} orbital to the $d_{xz,yz}$ orbitals. The energy of this transition is primarily influenced by the interaction of metal center and the oxygen ligand, which explains why the absorption onset is slightly different for the tungsten- and molybdenum-based compositions. Next, we consider the higher-energy absorption feature, where the absorption onset for the chlorides occurs at approximately 510 nm, while the onset for the bromide occurs at 620 nm. The energies of these absorption features also correspond to the visual appearances of these compounds, where both chlorides are green, while the bromide is a dark red. This feature is attributed to the transition between the d_{xy} and $d_{x^2-y^2}$ orbitals. In this case, the transition energy is determined by the anti-bonding interaction between the metal and halide ligands. Therefore, the bromide, which has weaker metal-halide bonding than the chlorides, absorbs at lower energies. In all of the compounds, there are multiple peaks in the absorption visible at wavelengths shorter than 400 nm. This is because in this energy range it is also possible to begin exciting higher-energy $d-d$ and ligand-to-metal charge transfer transitions.

After establishing the absorption properties of the tungsten and molybdenum oxyhalides, we can begin to investigate the intense near-IR emission in these materials. The first question to be addressed is which transitions in these materials give rise to the near-IR emission (shown in Figure 4.5). As illustrated by the UV-vis spectra and molecular orbital diagram, there are several possible scenarios which could produce near-IR emission. The first is that for excitation wavelengths in the range of 400 nm to 500 nm, an electron could be promoted from d_{xy} to $d_{x^2-y^2}$ and then radiatively decay to the $d_{xz,yz}$ states. The work of Gray *et. al.* suggests that the difference in energy between the $d_{x^2-y^2}$ and $d_{xz,yz}$ states is approximately 1.14 eV (1087 nm), which is similar to the energy of the emission. This scenario is also consistent with the work of Liu *et. al.*, which states that the most intense luminescence was observed using an excitation wavelength of 400 nm for both their tungsten- and molybdenum-based samples. A second possibility is that the emission arises from radiative decay from the $d_{xz,yz}$ states to the d_{xy} ground state. Based on the absorption onsets in the UV-vis spectra, the energy of this transition is between 1.34 eV and 1.50 eV (925 nm to 827 nm). In order to determine which of these transitions is responsible for the emission, near-IR fluorimetry excitation scans were used. Here, the intensity of the emission at 1000 nm was monitored while scanning the excitation wavelength. The results of the fluorimetry experiments suggest that exciting either of the first two $d-d$ transitions can produce near-IR emission; however, the fact that the emission persists and is more intense for lower energy (longer wavelength) excitation suggests that the emission comes from the $d_{xz,yz}$ to d_{xy} transition. In the case of the higher-energy excitation, we hypothesize that the emission comes from initially promoting an electron to the $d_{x^2-y^2}$ state, followed by non-radiative decay to $d_{xz,yz}$, and then followed by radiative decay to the d_{xy} state.

In addition to determining which *d*-to-*d* transitions produce near-IR emission in

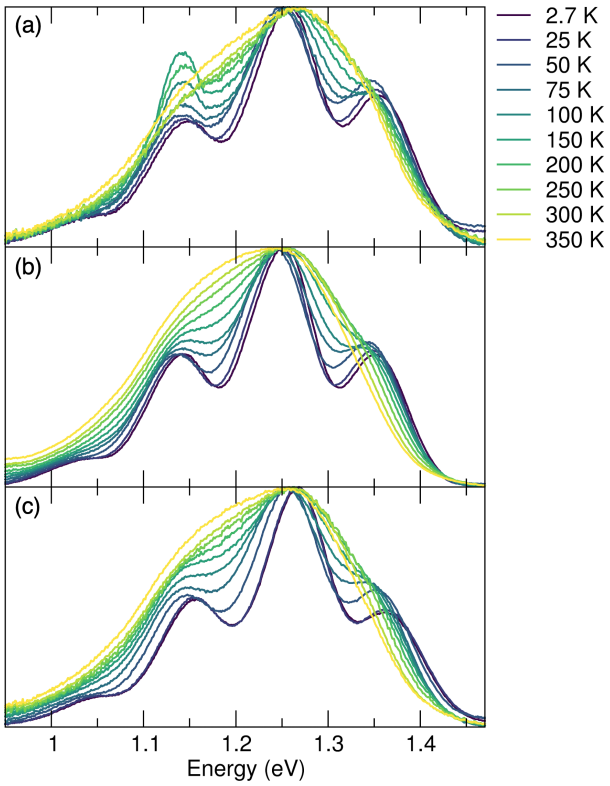

Figure 4.5: Variable-temperature near-IR emission spectra under 400 nm excitation for (a) $Cs_2WO_{1.3}Cl_{4.7}$ (b) $Cs_2MoO_{1.2}Cl_{4.8}$ and (c) $Cs_2MoO_{1.6}Br_{4.4}$. Photoluminescence data collected by Shobhana Panuganti at Northwestern University and Argonne National Lab

these compounds, it is also important to establish why multiple peaks are visible in the emission, which are particularly apparent at low temperatures. In previous reports, the multiple emission features were attributed to the presence of several self-trapped excitons associated with different structural distortions. [20] However, the peaks are at very similar energies in all of the spectra and, at the lowest temperatures, all show a very uniform energy-splitting of approximately 0.11 eV between each peak. Given the different compositions of the compounds explored in this work, it seems highly unlikely that self-trapped excitons associated with structural distortions would follow such a consistent progression in energies in all compounds. Additionally, in the molecular orbital diagram of Gray *et. al.*, there aren't any combination of electronic transitions that would give rise to the observed pattern. Therefore, here we consider a different explanation for this splitting pattern. Specifically, we find that the energy of the splitting in the emission is remarkably similar to the energy of the M=O stretches observed in the Raman spectra of these compounds. For example, at 100 K we find that the splittings between the three most prominent peaks in the emission spectra are 0.113 eV and 0.101 eV, while the energy of the W=O stretch at that temperature is 958.8 cm^{-1} (0.119 eV) in $Cs_2WO_{1.3}Cl_{4.7}$. Therefore, we believe that the fine structure of the emission in these compounds is largely due to vibronic coupling to the M=O stretches, rather than self-trapped excitons. Although the energies are not exactly identical, we attribute the slight discrepancy to the uncertainty associated with fitting multiple peaks under a curve, as well as the possibility of vibronic coupling to other bond-distortions. For example, vibronic coupling in the emission to the Te–X bond motions in the Cs_2TeX_6 compounds has been well-characterized. [142]

Finally, in order to provide a more-complete picture of the luminescence in these compounds, we have investigated the temperature-dependence of the emission life-

times, shown in Figure 4.6. As in the continuous-wave experiments, all data were collected using a 400 nm excitation, as this provided the highest-quality data. In all compounds, the lifetime was measured by measuring the emission at the wavelength corresponding to the most intense emission. First, we find that at low temperatures, all compositions show long emission lifetimes of approximately 45 μs for $Cs_2WO_{1.3}Cl_{4.7}$, 95 μs for $Cs_2MoO_{1.2}Cl_{4.8}$, and 80 μs for $Cs_2MoO_{1.6}Br_{4.4}$. These long lifetimes persist for temperatures between 2.7 K and 25 K In the temperature range between 50 K and 150 K, all compounds show a sharp decline in the emission lifetime, and for temperatures greater than 75 K, the behavior of the emission decay becomes more complex, requiring multiple exponential functions to fit the emission profiles.

In $Cs_2WO_{1.3}Cl_{4.7}$, at 75 K, the two lifetimes are 37 μs and 12 μs, with the relative weights of these components being 36% and 64%. At 100 K, the lifetimes are 32 μs and 8 μs, with component weights of 17% and 83 %. Finally, at 150 K, it is again possible to model the emission decay with a single exponential with a characteristic lifetime of 7 μs. Therefore, in this compound it is possible that for temperatures greater than 150 K, there are either two processes with similar lifetimes, or there is a complete transition from the longer-lifetime process occurring at low temperatures to the shorter-lifetime process at high temperatures.

In the molybdenum-based compounds, the situation is slightly different, as there is a larger temperature range where there is a clear coexistence of long- and short-lifetime processes. In $Cs_2MoO_{1.2}Cl_{4.8}$ and $Cs_2MoO_{1.6}Br_{4.4}$ at 75 K, the long-lifetime component is 65 μs, while the short lifetime components are 26 μs and 18 μs, respectively. In $Cs_2MoO_{1.2}Cl_{4.8}$, fraction of the longer-lifetime component declines more slowly than in the other compounds. It decreases from approximately 50% to 10% between 75 K and 250 K, and remains around 10% for temperatures greater than 250 K. In the case of

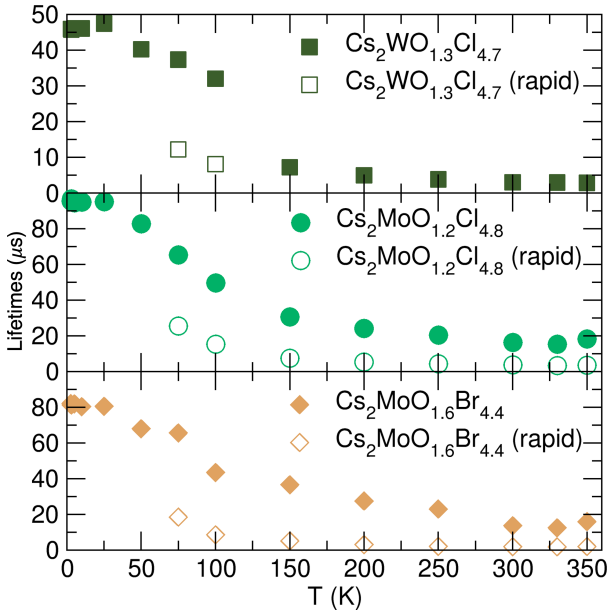

Figure 4.6: Temperature-dependence of the emission lifetimes for $Cs_2WO_{1.3}Cl_{4.7}$, $Cs_2MoO_{1.2}Cl_{4.8}$, and $Cs_2MoO_{1.6}Br_{4.4}$. Time-resolved photoluminescence data collected by Shobhana Panuganti at Northwestern University and Argonne National Lab.

$Cs_2MoO_{1.6}Br_{4.4}$, the fraction of the longer-lifetime component at 75 K is 32%, and the fraction decreases to below 10% at 150 K and below 5% at 250 K.

Overall, between 50 K and 150 K all of the compounds studied here show a transition from emission which is dominated by longer-lifetime processes at low temperatures to relatively shorter-lifetime processes at high temperatures, with the details varying slightly depending on the composition. Similarly to the structure and energy range of the emission, the trends in the lifetimes show that the two molybdenum-based compositions are more similar to one another than they are to the tungsten-based compound, despite the fact that the two chloride compositions appear more visually similar. At this time, it is not apparent if the slight differences in the lifetime trends for $Cs_2MoO_{1.2}Cl_{4.8}$ and $Cs_2MoO_{1.6}Br_{4.4}$ are determined by the presence of Cl versus Br, or if the differences in oxygen content are more influential. Additionally, given that the time-resolved data was only collected at a few selected wavelengths, it is not possi-

ble to definitively determine the nature of these longer and shorter lifetime processes; however, we believe that the trends revealed in the variable-temperature Raman spectroscopy may offer some insight into this point. Given that in $Cs_2WO_{1.3}Cl_{4.7}$ the transition to the short-lifetime process is complete at 150 K and there are changes in the trends in the W–Cl bending and W=O also around 150 K, we hypothesize that changes in the bond dynamics around each metal center may facilitate different emission pathways that lead to the change in lifetimes. Similarly to the other optical phenomena observed here, these changes are most likely driven by changes in the M=O bonds. However, Raman measurements over a more extended temperature range will be necessary to clarify this point.

4.4 Conclusion

In summary, in this work we have shown that the compounds with the formula $Cs_2MO_xX_{6-x}$ (M = Mo or W, X = Cl or Br), which can be synthesized via a hydrothermal method, exhibit intriguing near-IR emission which arises from the presence of oxygen in the $[MOX_5]^{2-}$ octahedra. The composition and structure of these materials can be established using several diffraction and spectroscopic techniques, and the results were used to show that the molecular orbital diagram of Gray *et. al.* can be applied to understand the optical properties of these samples. Both UV-vis absorption spectroscopy and photoluminescence measurements suggest that near-IR emission is due to radiative decay from the $d_{xz,yz}$ to the d_{xy} orbital. However, the emission can be produced by promoting electrons to either the $d_{x^2-y^2}$ or $d_{xz,yz}$ orbitals. Additionally, the broadness of the emission is shown, at low temperatures, to arise from the presence of multiple distinct peaks in the emission. Raman spectroscopy and analysis

of the temperature-dependence of these features show that they are likely due to vibronic coupling to the $M{=}O$ stretches. Finally, time-resolved measurements show that at low temperatures, all compounds show long emission lifetimes on the order of 10s of microseconds. However, between 50 K and 150 K, there is a transition to shorter-lifetime emission which also coincides with subtle shifts in the energies of the Raman-active modes. Future studies involving more Raman experiments and streak-camera time-resolved photoluminescence measurements will help to determine the connection between these observations.

Chapter 5

Aluminum-based materials as low-κ dielectrics

Advances in telecommunications require electronics that operate at ever-increasing frequencies, exemplified by 5G or fifth generation technologies that operate in the GHz regime. At high frequencies, electrical circuits are plagued by so-called RC delays, arising from the time constant $\tau = RC$ for electrical signals which is the product of the resistance R and the capacitance C, respectively, of conductors and their insulating substrates. Beside using high quality, low-R electrical conductors such as high-purity Cu with low surface roughness, small RC delays are achieved by lowering the dielectric constant κ of the materials used in printed circuit board (PCB) substrates. These largely comprise particles of an inorganic material, notably functionalized SiO_2, embedded in a polymer-based matrix. The value of κ of the composite is primarily dictated by κ of the inorganic material. The properties of the inorganic component also impact

At the time of publication the contents of this chapter have been submitted to *Chemistry of Materials* as: E. E. Morgan, A. Zohar, S. Lipkin, B. Monserrat, R. Zhang, S. Vaidyanathan, D. Loeffler, A. K. Cheetham, and R. Seshadri, Aluminum-Based Materials as Low-κ Dielectrics.

other relevant parameters such the quality factor, mechanical strength, and thermal expansion of the substrate. Here we ask whether there are inorganic compounds with dielectric constants (measured at 10 GHz) that are lower than that of SiO_2 that could potentially replace it in electronics. We describe the key characteristics for low-κ materials and develop a framework for screening such compounds by employing some guiding principles, followed by using a combination of empirical estimates and density functional perturbation-theory based calculations. We then report experimental results on two promising, aluminum-based low-κ compounds for high-frequency applications. The first is the cristobalite form of $AlPO_4$. The second is the simplest 3D metal-organic framework, aluminum formate $Al(HCOO)_3$. The measured values of κ at 10 GHz, which are 4.0 for $AlPO_4$ and 3.8 for $Al(HCOO)_3$, compare well with what is measured on SiO_2 particles.

5.1 Introduction

The implementation of fifth-generation (5G) telecommunications technology promises many significant advancements in data networks, including faster, more reliable, and cheaper communication. One barrier to realizing these potential benefits is that current hardware must be optimized for compatibility with the high-frequency ranges used in 5G networks. An example of this can be found in the development of specialized electronics used for multiple-input multiple-output antennae in 5G handsets and base stations. The ideal dielectric material for use in these electronics should possess a low dielectric constant (κ) and low loss at the frequencies of interest, and should allow for effective thermal and thermomechanical management. Critically, the material with the lowest dielectric constant will produce the most efficient antenna, which in turn will

reduce power consumption in devices. [143]

Identification of materials that have all of these necessary characteristics is a challenge for widespread implementation of the 5G technology. Furthermore, the need for low-κ and low-loss materials extends beyond 5G applications to other types of advanced electronics that rely on printed circuit board (PCB) technology. [144, 145] In general, the operational speed of a circuit is limited by its time constant $\tau = RC$, the product of the resistance R and capacitance C. As circuits become smaller, with thinner wires placed closer together, the resistance of the wires and capacitive effects between them increase, causing longer delays. Given that circuit miniaturization is required to produce advanced devices, a critical strategy to lower τ is to reduce capacitive effects by using a PCB material with a low dielectric constant. [146]

In addition to low dielectric constant, there are several other important characteristics for the low-κ material to be used in PCBs. These include: low loss, thermal and chemical stability, hydrophobicity, mechanical strength, low thermal expansion, and acceptable thermal conductivity. [145] In order to meet these requirements, a common solution is to combine a low-κ inorganic component, such as silica particles or fibers, with an organic polymer to produce a composite which takes advantage of the best qualities of both materials. The dielectric properties of these composites can also be enhanced through a number of strategies. For example, more C–C and C–F bonds can be incorporated into the polymer to minimize polarizability and hence κ. [147] Additionally, porosity can be engineered into the composite in order to lower its density and therefore reduce the number of dipoles. [147–149]

There are several ways to reduce the dielectric constant of composites, but each often involves trade-offs with other desirable qualities. For example, the use of a larger volume fraction of the organic component relative to the inorganic component may

lead to a lower dielectric constant for the composite but could produce deleterious thermal expansion effects and poor mechanical properties. Therefore, in order to further reduce the dielectric constant of PCB composites, it is important to identify materials which have the desirable qualities of silica (low loss, mechanical strength, stability, and good thermal management) while also possessing low dielectric constants (defined in this work as being < 4.0 when measured at 10 GHz.)

Several materials have been proposed as alternatives to silica, including $AlPO_4$–BPO_4–SiO_2 ternaries, [146] cordierite, [150–152] and several borates. [153–155] The characteristics of these compounds suggest that compounds with low-atomic number atoms and open frameworks should be prioritized. Furthermore, the search for low-κ materials should be contrasted with efforts to find inorganic high-dielectric constant materials and ferroic materials [156–161] where traditionally second-order Jahn-Teller [162] ions such as Ti^{4+} and lone-pair ions such as Bi^{3+} are used. [163] These works aid in the search for low-κ materials by suggesting which ions are best avoided.

In the present work, we have focused on developing a methodology for the identification of materials with dielectric constants comparable to or lower than that of silica. The main challenges are the large number of parameters that require optimization for a successful low-κ material and the lack of standardization in literature in reporting of dielectric constants. We have found that estimates using the additive formula [164] with empirical values tabulated by Shannon, [165] are suitable for identifying potential low-κ candidates from a large database of materials. First-principles calculations based on density functional perturbation theory (DPFT) then refine the search, and also permit estimates to be made for compounds that are not suited for the Shannon approach. As a result of this screening procedure, we have identified the simple aluminum-based framework structures, $AlPO_4$ and the metal-organic framework $Al(HCOO)_3$ (ALF), as

suitable for low-κ applications. ALF is arguably the simplest example of a metal-organic framework and has both porosity and excellent mechanical properties. It has recently been shown to be effective in a number of important gas separations. [166–168] We have prepared these compounds and discuss different strategies for the measurement of high-frequency dielectric properties of powders. Finally, we compare the case of $AlPO_4$, where DFT gives an accurate estimate of the dielectric constant, to the case of $Al(HCOO)_3$, where a simple DFT calculation does not initially correctly predict the dielectric constant.

5.2 Methods

5.2.1 First-Principles Calculations

Static dielectric constants were estimated using density functional theory (DFT)-based electronic structure calculations as implemented in the Vienna ab initio Simulation Package (VASP). [51–53] All calculations used the PBE functional, [58] PAW pseudopotentials, [66, 100] a plane-wave cutoff energy of 500 eV, and a Monkhorst-Pack grid [169] with a length parameter of 30. For the density functional perturbation theory calculations of the dielectric constant, [78, 79] we report the predicted constant for a polycrystalline sample using Equation 5.1,

$$\kappa = \frac{3\lambda_1\lambda_2\lambda_3}{\lambda_1\lambda_2 + \lambda_1\lambda_3 + \lambda_2\lambda_3} \tag{5.1}$$

where λ_i are the eigenvalues of the total dielectric tensor calculated in VASP. This is the convention used in other high-throughput DFT studies of dielectric constants. [170].

As discussed previously, [171] estimating the dielectric constant of a polycrystalline sample from the tensor components is not trivial except in the case of high symmetry crystal structures, and the formula used here will not always give the same results as other common approaches, such as averaging the eigenvalues.

5.2.2 Synthesis of $Al(HCOO)_3$

A hydrothermal synthesis of $Al(HCOO)_3$ was performed following the literature. [172] 50 mg (0.64 mmol) of $Al(OH)_3$ was combined with 7 mL of concentrated formic acid and stirred for 30 min. The mixture was then transferred to a teflon-lined 23 mL stainless steel digestion vessel and heated at 130 °C for 3 days. Cooling to room temperature yields a white powder, which was isolated by filtration and rinsed with concentrated ethanol. In order to remove the template CO_2 molecule from the cavities of the structure, the powder was heated at 180 °C for 24 hours. [166]

5.2.3 Modification of $AlPO_4$

$AlPO_4$ was purchased from Fisher Scientific; however, the as-received powder was multiphasic. In order to isolate the desired orthorhombic phase, which has the cristobalite structure, the powder was heated to 1300 °C in a furnace and allowed to equilibrate for 1 h. The sample was then removed from the furnace and allowed to cool rapidly in air.

5.2.4 Powder X-ray Diffraction and Rietveld Refinements

Powder X-ray diffraction (PXRD) measurements were performed on a Panalytical Empyrean powder diffractometer in reflection mode with a Cu-Kα radiation source. Rietveld analysis was performed to confirm structure and phase-purity using the TOPAS software package. [36] Crystal structures were visualized using the VESTA software package. [99]

5.2.5 Scanning electron microscopy

The $Al(HCOO)_3$ and $AlPO_4$ powders were placed on double sided carbon tape and inserted into an Apreo C FEG (ThermoFisher) microscope chamber. SEM images were collected using secondary electron (SE) and InLens detectors with 5 keV accelerating voltage and 0.8 nA current.

5.2.6 Infrared Spectroscopy

Fourier transform infrared (FTIR) spectra of powders were obtained using a Nicolet iS10 FTIR equipped with a Smart Diamond ATR accessory in absorption mode.

5.2.7 Pellet Preparation

Two methods of preparing pellet samples for dielectric measurements were employed. The first was a modified version of a literature procedure [173] in which different volume loadings of inorganic particles were introduced into a paraffin wax matrix. We prepared mixtures of different ratios of melted paraffin wax and the inorganic

phase of interest and drop-cast pellets of the mixtures onto polyethylene terephthalate (PET) sheets. The pellets were flattened into thin films (thickness less than 1 mm) suitable for measurement as the mixture cooled by pressing the PET sheets together.

While this first method has been shown to be reliable for measuring the dielectric constant of a variety of materials, [173] it was difficult to obtain pellets of perfectly uniform thickness. Given that the dielectric measurements are very sensitive to even small differences in thickness, it was desirable to test a second set of samples where we could control the thickness more carefully. For this set of samples, the material under investigation was ground together with polytetrafluoroethylene (PTFE) beads in an agate mortar and pestle. After grinding the materials, the mixture was placed into a pellet die with a diameter of 25.4 mm and pressed with forces up to 5 tons. Using helium pycnometry, it was estimated that this process achieves a pellet densification of between 85% and 90%.

5.2.8 Dielectric Property Measurements

A split-post dielectric resonator (SPDR, purchased from Keysight Technologies) was used in conjunction with a Agilent PNA model N5242A vector network analyzer (VNA) for measurements of high-frequency dielectric properties. A complete description of the method can be found in the literature. [174] In summary, two coupling loops induce a continuous electric field in the microwave frequency regime within the plane of the sample. The resonant frequency and quality factor of the SPDR will shift in the presence of a sample, and therefore the sample properties can be determined by measuring the SPDR in the absence and presence of the sample. The resonant frequency can be found with uncertainties on the order of 0.5% to 1% of the measured resonant curve bandwidth. The SPDR has a resonance frequency of 10.159 GHz and can mea-

sure samples up to 0.95 mm thick, where the sample diameter was always equal to or greater than 22 mm. The accuracy of the device was confirmed by measurement of a fused silica reference sample included with the SPDR, which has a measured dielectric constant of 3.824.

The SPDR was calibrated by first performing transmission measurements between the two ports of the VNA in a shorted configuration using flexible SMA cables (to account for losses coming from those cables). The signal was normalized around the resonance frequency 10.159$\pm$0.500 GHz using the calibration setting of the VNA software. Following calibration, the SPDR was connected with the two SMA cables. A reflectance measurement was used to find the resonant frequency. For an empty resonator, the frequency should be similar to the device specification (10.159 GHz). A transmission measurement was recorded at the resonance frequency and the Q value was extracted from the bandwidth at 3 dB beneath the peak of the transmission curve. Next, the sample was inserted to the SPDR and the resonance frequency and Q value were recorded.

The sample thickness was determined by micrometer or SEM cross section. The collected values (resonance frequency, Q, and thickness) were entered into the software to extract the dielectric constant and the energy loss factor following Equation 5.2.

$$\kappa = 1 + \frac{f_o - f_s}{h f_o K_\kappa(\kappa_r, h)} \tag{5.2}$$

where h is the thickness of the sample under test, f_0 is the resonant frequency of the empty SPDR, f_s is the resonant frequency of the SPDR with the sample and K_κ is a function of κ and h determined by the software.

In order to determine the dielectric constant of solid inorganic materials, pellets

were prepared as described in the previous section and their dielectric constants were measured. The data for pellets of various compositions was then fit the the Looyenga mixing model, [175] which is shown in Equation 5.3.

$$\kappa_{mix}^{1/3} = V_m \kappa_m^{1/3} + V_p \kappa_p^{1/3} \tag{5.3}$$

where κ_m and κ_p are the dielectric constants of the organic matrix and inorganic particles, respectively, and V_m and V_p are their volume fractions.

5.3 Results and Discussion

There are several strategies for estimating the dielectric constant of materials, including empirical estimates, [165, 176] machine-learning, [177] and high-throughput DFT. [170] In our work, we have focused on using a combination of physics-based principles to select a set of compounds on which we have carried out empirical estimates and DPFT calculations. The strategy is outlined in Figure 5.1. The first step was to establish a set of criteria for low-κ compounds, based on the literature [164, 178]. These principles are used to screen the Inorganic Crystal Structure Database (ICSD) [179] to identify candidate materials. The criteria are that materials must be (i) insulating, (ii) stable under ambient conditions and (relatively) easy to synthesize, (iii) primarily comprise small (low-atomic-number) and high-charge atoms, (iv) crystallize in structures with extended connectivity (no molecular structures or salts), and (v) be relatively low-density (structures with corner-sharing polyhedra are prioritized over those with edge- or face-sharing). Finally, disperse bands are contraindicated for low dielectric constants at high frequencies, suggesting that highly covalent 3D networks

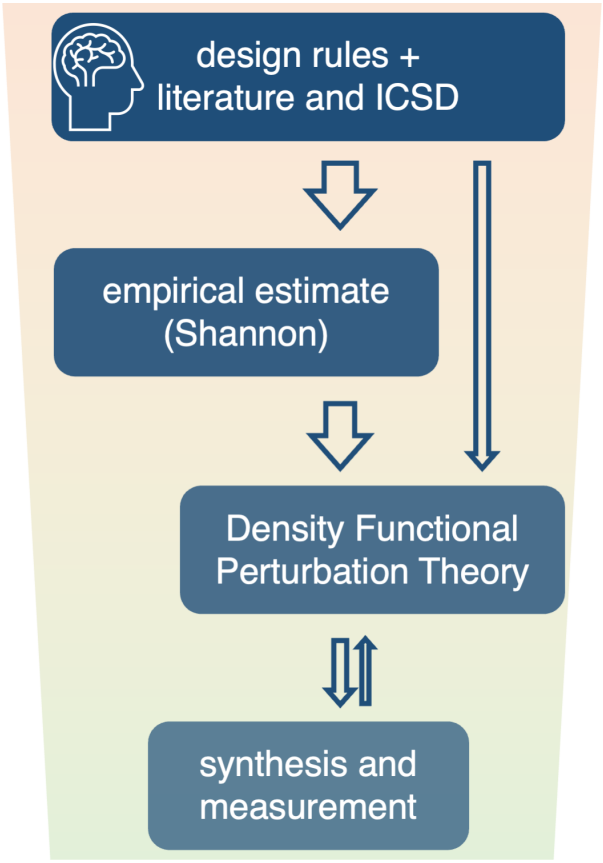

Figure 5.1: Workflow for the identification of low-κ materials.

(diamond for example) would not be suitable targets. A class of compounds that meets many of the above criteria are the aluminosilicate zeolites, due to their porous nature and low-atomic-number components. However, many zeolites are hydrophilic or are otherwise prone to incorporating small molecules in their cages, making many of them unsuitable as stabe low-κ dielectrics. We have separately attempted to screen for low-κ materials using the Materials Project. [170, 180] However, among experimentally-observed materials reported in the Materials Project, the materials with low dielectric constants were either already known to us, molecular structures, or materials whose calculated dielectric constants seemed unlikely to be accurate due to the presence of small band gaps or unpaired electrons.

The second step, after identifying a number of inorganic compounds is to empirically predict the dielectric constants. The estimate used here is based upon the Clausius-Mosotti equation for the dielectric constant, where each element is assigned an empirically-determined value for its dielectric polarizability α_i, for ion i estimated and tabulated by Shannon. [165] The equation, presented in Equation 5.4, only requires the contents of the unit cell (number and type of each atom) and its volume as inputs.

$$\kappa_{emp.} = \frac{\tilde{V} + 2\alpha(4\pi/3)}{\tilde{V} - \alpha(4\pi/3)} \tag{5.4}$$

Here, $\alpha = \Sigma_i \nu_i \alpha_i$ with ν_i being the stoichiometry coefficient of component i, and $\tilde{V}$ is the molar volume from the associated ICSD crystallographic information files (CIF) file. A Python script was written to parse CIFs files and calculate the expected dielectric constants. A disadvantage of this equation is that it can only be applied to conventional oxide and fluoride crystal structures, so it is not suitable for all materi-

als. Additionally, this equation is not accurate in cases of "unusual" dielectric properties, such as ferroelectrics or conductive materials, and it does not account for the frequency-dependence of the dielectric constant. [165] Given that we had already selected compounds with low atomic number element compositions, the estimated $\kappa_{emp.}$ were all fairly low ($<$10). However, this step was still important to confirm our selection criteria and provide a preliminary ranking for which materials should be further investigated.

After calculating $\kappa_{emp.}$, DPFT calculations were performed to provide a potentially more accurate estimate of the dielectric constant κ_{DFT}. This step was particularly important in order to validate the results of the empirical estimation and to estimate the dielectric constant for compounds where the additive formula could not be applied because of an absence of the requisite parametrization. Here, we have focused on calculating the static dielectric constant, which is the sum of the electronic and ionic contributions to polarization. A full frequency dependence was not calculated because of the greater computational expense and because the static constant was expected to be similar to what would be predicted for the GHz regime in a frequency-dependent calculation. We additionally note that these DFT calculations were performed on CIFs obtained from the ICSD and literature without performing geometry optimizations.

The results of some of the DFT-calculated dielectric constants plotted against their associated empirical values are shown in Figure 5.2. The calculated values are also shown in Table 5.1. The compounds represented in this plot are those identified by our screening criteria or those reported in the literature as potential low-κ materials, such as SiO_2. In nearly all cases, the dielectric constant estimated by DFT is larger than that estimated by the Shannon constant. This is consistent with other work on DFT calculations, which has found that DFT tends to overestimate the dielectric constant.

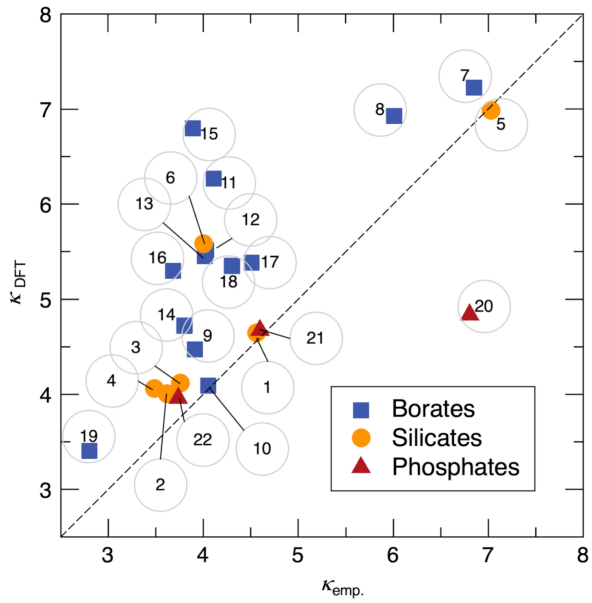

Figure 5.2: Plot of the DFT-calculated dielectric constant versus the associated empirical estimates using the Shannon parametrization. The samples identities corresponding to the numbering numbers are listed in Table 5.1.

Material	$\kappa_{emp.}$	κ_{DFT}	Material	$\kappa_{emp.}$	κ_{DFT}
1. SiO_2 (quartz)	4.56	4.65	13. $Na_2B_6O_{10}$	4.02	5.45
2. SiO_2 (tridymite)	3.62	4.01	14. NaB_4O_6F	3.80	4.72
3. SiO_2 (α-cristobalite)	3.76	4.12	15. $Na_3Al_2B_7O_{15}$	3.89	6.80
4. SiO_2 (β-cristobalite)	3.48	4.06	16. $Na_3AlB_8O_{15}$	3.68	5.30
5. Mg_2SiO_4	7.03	6.99	17. $Na_3B_7O_{12}$	4.51	5.38
6. $Mg_2Al_4Si_5O_{18}$	4.00	5.59	18. $Na_2B_8O_{13}$	4.30	5.35
MgF_2	5.25	5.13	19. H_3BO_3	2.80	3.40
$NaSbF_6$	N.A.	4.45	20. BPO_4	6.80	4.84
7. $Mg_3B_2O_6$	6.85	7.23	21. $AlPO_4$ (hex.)	4.60	4.67
8. $Mg_2B_2O_5$	6.01	6.93	22 $AlPO_4$ (ortho.)	3.74	3.96
9. $Li_2B_3O_4F_3$	3.91	4.47	α-$Al(H_2PO_2)_3$	N.A.	3.96
10. LiB_6O_9F	4.05	4.09	γ-$Al(H_2PO_2)_3$	N.A.	4.05
11. $Na_2B_4O_7$	4.11	6.27	$Al(HCOO)_3$	N.A.	3.14
12. $Na_2B_6O_9F_2$	4.03	5.51	$Al(OH)(COOH)_2$	N.A.	3.91

Table 5.1: Estimated dielectric constants for crystalline compounds of interest using the empirical formula ($\kappa_{emp.}$) based on the Shannon parametrization (when possible) and density functional perturbation theory calculations (κ_{DFT}). The numbers refer to the labeling in Figure 5.2.

[170] A notable exception to this trend is BPO_4, whose Shannon constant is 6.8, while the estimated constant from DFT is 4.8. Furthermore, other boron-based materials on this plot also show significant differences between the empirical value and DFT prediction. Based on the additive formula, many are predicted to have $\kappa < 4.5$, but their predicted constants based on DFT are significantly higher. These differences most likely arise from the empirical nature of the additive formula and the fact that the method assumes the polarizability value for B^{3+} to be 0.05. Therefore, while boron-based materials may still be promising for low-κ applications, we find that the additive formula with the values of α_i provided by Shannon may not yield the most accurate prediction of the dielectric constant for boron-rich compositions. Overall, we find that in most cases, the DFT-calculated value can be considered an upper limit for the estimate of the dielectric constant, while the Shannon value can be considered a lower limit.

Considering the results of the DFT calculations, we found that only a few materials had predicted dielectric constants that were comparable to that of SiO_2. These were $AlPO_4$ (κ_{DFT} = 3.96), $Al(H_2PO_2)_3$ (κ_{DFT} = 3.96), and $Al(HCOO)_3$ (κ_{DFT} = 3.14). In the case of $AlPO_4$, the constant estimated from the additive formula was slightly lower, at 3.73. For the other materials, which are hybrid organic-inorganic structures, it was not possible to calculate the empirical value, as no polarizability values are available for the organic components. To validate our predictions, we chose to focus on the dielectric constants of $AlPO_4$ and $Al(HCOO)_3$. These compounds were selected because $AlPO_4$ has been previously reported as a potential low-κ material, while $Al(HCOO)_3$ has the lowest DFT-estimated constant of any material that we investigated and has not been previously considered as a low-κ material.

In order to investigate the dielectric properties of $AlPO_4$ and $Al(HCOO)_3$, it was important to obtain phase-pure samples of these materials. $Al(HCOO)_3$ can be synthesized

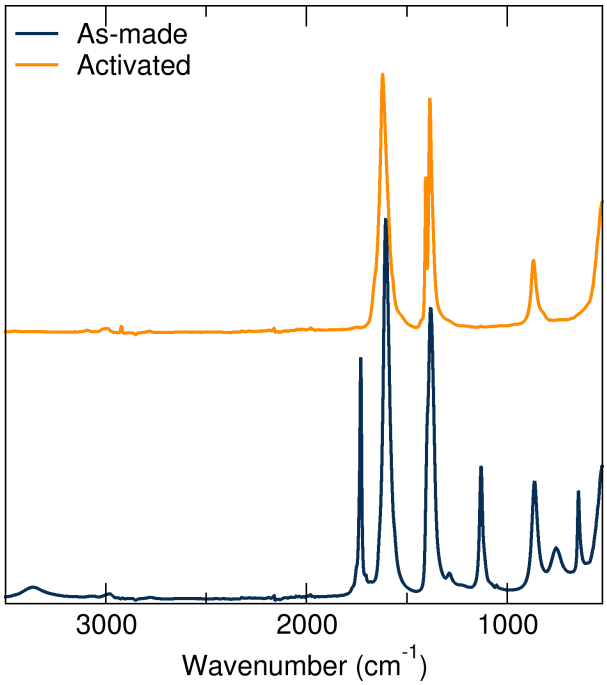

Figure 5.3: FTIR of $Al(HCOO)_3$ before and after heating to 180 °C overnight.

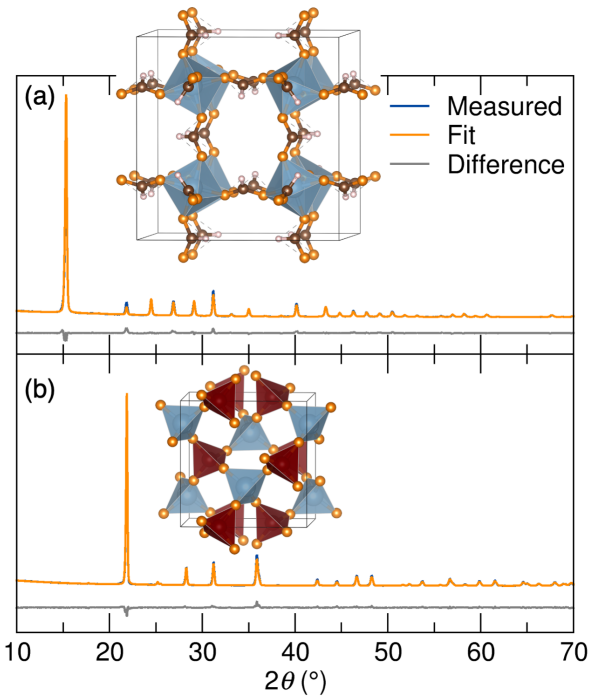

Figure 5.4: Powder X-ray diffraction patterns and Rietveld refinements for (a) $Al(HCOO)_3$ and (b) $AlPO_4$. Insets show the crystal structures of the two compounds.

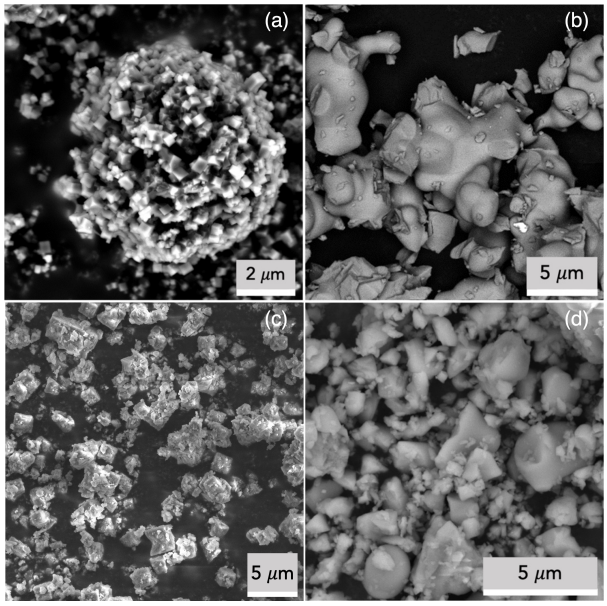

Figure 5.5: SEM images of (a) $Al(HCOO)_3$ and (b) $AlPO_4$ before and (c) $Al(HCOO)_3$ and (d) $AlPO_4$ after ball-milling.

on the gram scale using hydrothermal synthesis, as reported in the literature. [172] During the synthesis, CO_2 molecules template the formation of the structure and should be removed from the cavities by heating the material to 180 °C for 24 hours. [166] The removal of CO_2 was confirmed using FTIR spectroscopy, shown in Figure 5.3. The PXRD pattern and Rietveld refinement for $Al(HCOO)_3$ confirming phase-purity after heating are shown in Figure 5.4(a). In the case of $AlPO_4$, the material is purchased from commercial vendors. However, we have observed that the powder is often received as a mix of polymorphs. In order to obtain the pure orthorhombic phase, which was estimated to have the lowest dielectric constant, the powder required heat-treatment. The powder was heated to 1300 °C, held at that temperature for one hour, and then the crucible was removed from the furnace to cool in air. The PXRD patterns and Rietveld refinements shown in Figure 5.4(b) confirm that the material is single-phase following this procedure.

After confirming phase purity using XRD, SEM was used to demonstrate that the

samples were homogeneous and that no amorphous phases were present. SEM images of $Al(COOH)_3$ and $AlPO_4$ particles are shown in Figure 5.5. In the case of $Al(HCOO)_3$, the as-synthesized particles are cube-shaped with a typical edge length ranging from 100 nm to 500 nm. These small cubes tend to form spherical aggregates which are 5 μm to 10 μm in diameter. For the $AlPO_4$, we observed globule-shaped particles whose size was also on the order of 10 μm. These larger aggregates and particles are not necessarily a problem for the measurement of dielectric properties. However, in practical applications, the particle size would need to be reduced to $< 1\mu$m in order to produce homogeneous films. We therefore ball-milled samples to reduce particle size. In $Al(HCOO)_3$, the small cube-shaped particles remain after 30 minutes of ball-milling, but the larger spherical aggregates are not observed. For $AlPO_4$, SEM images show that ball-milling effectively breaks the larger particles into smaller fragments. In both cases, XRD confirms that the underlying crystal structure remains intact. This observation is in agreement with previous reports which demonstrate that, unlike other metal-organic frameworks, $Al(HCOO)_3$ is mechanically robust. [166] In summary, with proper post-synthetic modification, both materials could potentially be incorporated into epoxy substrates for PCB applications.

After confirming the structure and composition of our materials, we sought to determine their dielectric constants at high frequencies (10 GHz). A split post dielectric resonator (SPDR) device connected to a vector network analyzer (VNA) was employed, as described in the Methods section. This allowed us to quickly and reliably measure many samples because it does not require contact deposition or customized hardware. The SPDR is primarily designed for measuring composite films similar to PCB materials; therefore, powders must be embedded in an organic matrix to form a thin film with a diameter larger than 22 mm. For each inorganic material, the dielectric constant can

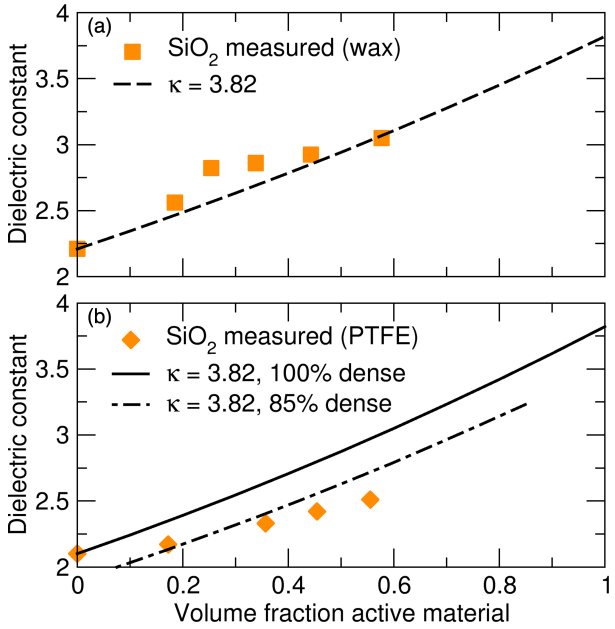

Figure 5.6: (a) Measured dielectric constants for SiO_2 and paraffin wax pellets and fit to Looyenga model with $\kappa = 3.82$. (b) Measured dielectric constants for SiO_2 and PTFE pellets and fits to Looyenga model with $\kappa = 3.82$ accounting for different levels of densification.

be evaluated by making samples with different ratios of inorganic particles to organic matrix material. The dielectric constants of these samples are subsequently measured, and the results fit to the Looyenga mixing model. [175] This model takes into account the dielectric constants of the pure components and their volumetric fraction in the mixture.

As discussed in the Methods section, two types of samples were prepared in order to measure the dielectric constants of inorganic powders. Each of these methods has its own benefits and drawbacks. In the case of the paraffin pellets, the main advantage is that it is easier to control the precise composition of the mixture, which makes the data most suitable for modeling with the Looyenga mixing model. However, the drawback to this method is that the drop-cast mixture must be flattened into a thin film as the mixture cools, which often leads to inhomogeneity in the thickness of the

films. Additionally, it is difficult to produce films that have larger volume fractions of the inorganic material, as the solidified mixtures become very brittle. For these reasons, we also produced a second set of samples which were mixtures of PTFE and the inorganic particles. These samples were prepared by grinding the materials in a mortar and pestle and pressing them together using a pellet die and hydraulic press. This method is effective because grinding the PTFE beads forms sheets which can encapsulate the inorganic powder, and the samples can be pressed to a very uniform thickness. However, the disadvantage of this method is that it was not possible to achieve 100% densification of the pellets. Therefore, in order to interpret the dielectric data, the role of air must be accounted for in the mixing model, which adds additional uncertainty to the interpretation of the data for these samples. In order to evaluate the effectiveness of both sample-preparation methods, we used fumed silica powder as a test material, which is known to have a dielectric constant of 3.82. The results for both sets of measurements are shown in Figure 5.6.

First considering the results for the silica and paraffin wax pellets, we find that the data fits fairly well to the Looyenga mixing model when the dielectric constant of the pure wax is assumed to be 2.2 and the constant of pure silica is 3.82. However, for some of the intermediate compositions there is a discrepancy between the measured data and the model, which is likely due to variation in the thicknesses of some of the samples. Next, considering the PTFE data, we find that the measured dielectric constants for the pellets are much lower than would be expected if the pellets were 100% dense. Here, the dielectric constant of PTFE is assumed to be 2.1, and silica again is 3.82. Therefore, in this case we needed to add air as an additional “component" in the Looyenga model and adjust the volume fractions of the silica and PTFE accordingly. Using this method, we find that the best match to our data corresponds to a densifica-

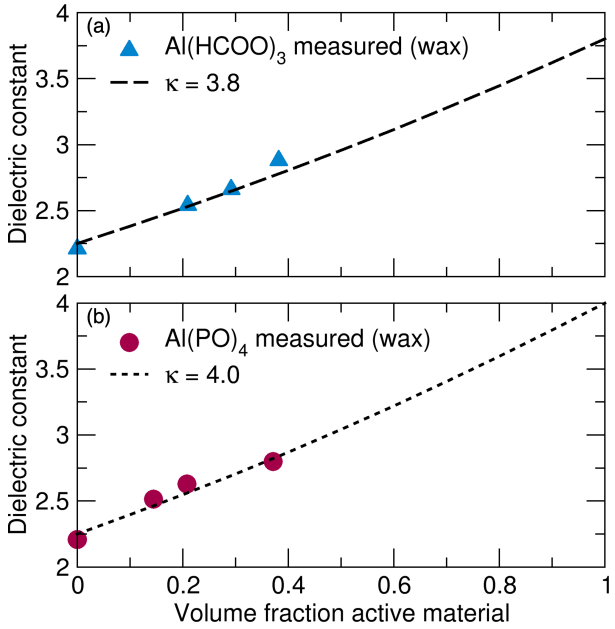

Figure 5.7: Measured dielectric constants for (a) $Al(HCOO)_3$ and paraffin wax pellets (b) $AlPO_4$ and paraffin wax pellets.

tion of approximately 85%. This is in good agreement with pycnometry measurements of the pellets, which indicated a densification of approximately 90%. We find that the fit is not as good for larger volume fractions of silica, which can be attributed to the fact that the densification may be dependent on the composition of the pellet. Overall, we find that the paraffin wax method provides a more reliable measurement of the dielectric constant, but that PTFE pellets can be used to corroborate the results.

Given the results of the dielectric measurements for the silica pellets, we have used paraffin wax pellets to estimate the dielectric constants of our two candidate materials. The measurements and data fitting for paraffin pellets of $Al(HCOO)_3$ and $AlPO_4$ are shown in Figure 5.7. Again using the Looyenga mixing model, the dielectric constants were determined to be 3.8 for $Al(HCOO)_3$ and 4.0 for $AlPO_4$. Just as in the case of the silica pellets, we have also confirmed these values by measuring mixtures of our candidate materials with PTFE., as shown in Figure 5.8. The loss values for all materials

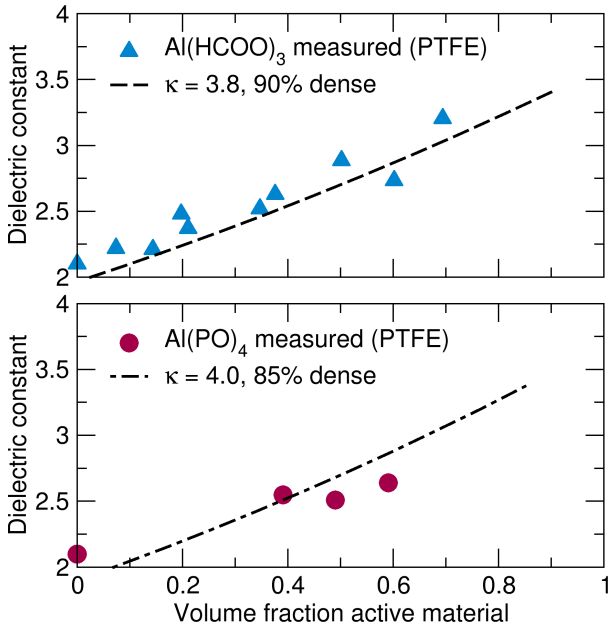

Figure 5.8: Measured dielectric constants for (a) $Al(HCOO)_3$ and PTFE pellets (b) $AlPO_4$ and PTFE pellets.

in the paraffin wax pellets are shown in Table 5.2. In the case of $AlPO_4$, the measured value is very close to the value of 3.96 predicted by DFT. However, for $Al(HCOO)_3$, there is a significant difference between the measured value of 3.8 and the value of 3.14 predicted by DFT. This finding is also somewhat unusual in that it represents a case in which the experimental dielectric constant is higher than the DFT prediction.

We hypothesized that the discrepancy between theory and experiment for $Al(HCOO)_3$ may be due to finite temperature effects which were not accounted for in the DFT calculation, or inaccuracies in the position of the organic linkers in our structural model. Therefore, we have further investigated how changes to the $Al(HCOO)_3$ structure may influence the calculated dielectric constant. In Figure 5.9, we show the crystal structure of $Al(HCOO)_3$ determined from Rietveld refinements of neutron diffraction data superimposed with the structure that results from relaxing the atomic positions in DFT using the PBE functional. The first crystal structure was used in our original DFT cal-

SiO_2	
Volume fraction	Average loss
0	4.12×10^{-4}
0.185	5.59×10^{-4}
0.254	6.53×10^{-4}
0.338	7.18×10^{-4}
0.443	7.03×10^{-4}
0.577	7.84×10^{-4}
$Al(HCOO)_3$	
Volume fraction	Average loss
0.209	3.48×10^{-3}
0.292	7.29×10^{-3}
0.382	1.00×10^{-2}
$AlPO_4$	
Volume fraction	Average loss
0.144	1.11×10^{-3}
0.208	1.18×10^{-3}
0.371	1.67×10^{-3}

Table 5.2: Average dielectric loss values associated with the measurements of materials in paraffin wax.

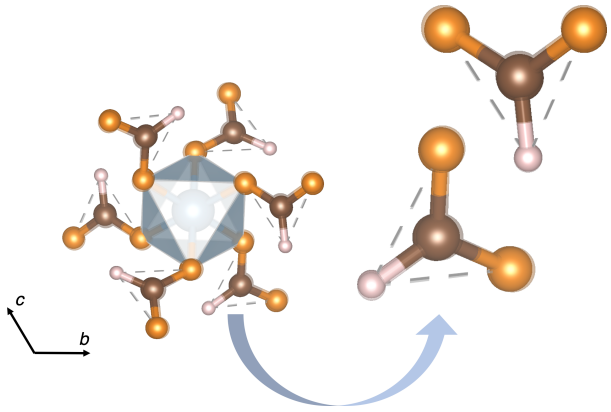

Figure 5.9: Crystal structure fragment of $Al(HCOO)_3$ at 300 K determined from neutron diffraction superimposed with the structure obtained by relaxing the atomic positions in DFT.

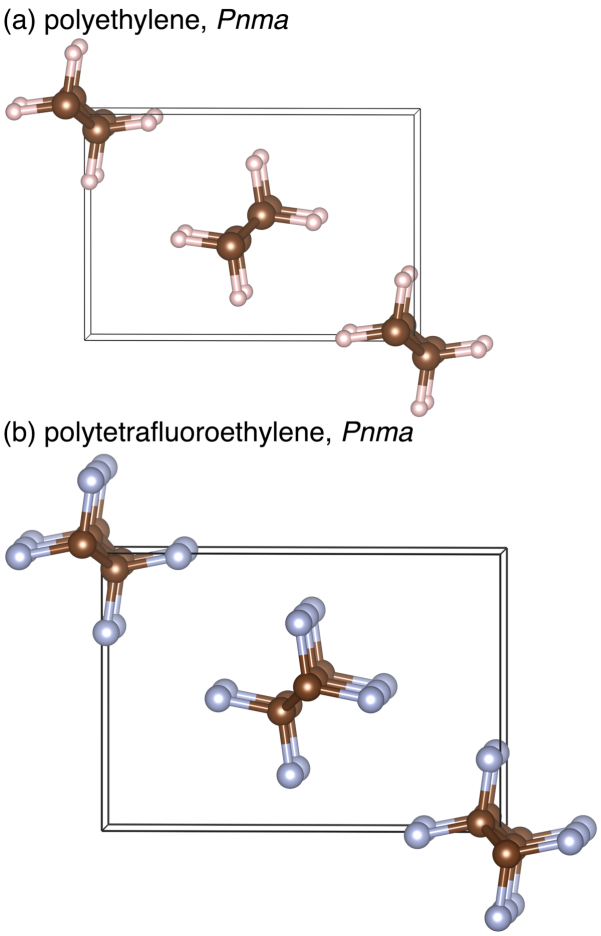

Figure 5.10: DFT-relaxed crystal structures of (a) polyethylene and (b) polytetrafluoroethylene (PTFE). Both relaxations used the PBE functional and a D3 dispersion correction. [181, 182]

culations and gives the predicted dielectric constant of 3.14. We also calculated the constant for the relaxed structure and obtained a value of 4.14. The main difference between the two calculated values lies in a change in the ionic contribution to the dielectric constant, where the original structure has an ionic component of 1.15, while in the relaxed structure the value is 2.12. This result is somewhat surprising, as the changes to the crystal structure are extremely small, indicating that the ionic component of the calculated dielectric constant is strongly dependent on the atomic positions in this structure.

In order to determine whether the sensitivity of κ_{DFT} to structure is common to different types of compounds, we also investigated the effects of DFT relaxation on other compositions studied in this work. For example, in $ALPO_4$, we found that the value of κ_{DFT} changed from 3.96 (experimental structure) to 3.98 (atomic positions relaxed with PBE-DFT). The more significant change for $Al(HCOO)_3$ was consistent with our idea that the presence of the organic linker may contribute significantly to the dielectric constant for this compound. For this reason, we also used DFT to predict the dielectric constants of polyethylene and PTFE. In the case of polyethylene, the calculated value of κ_{DFT} is 2.52, while for the relaxed structure κ_{DFT} is 2.64. For PTFE, there is no crystal structure available for ambient conditions, so a structure was generated by changing the polyethylene structure such that all H atoms were replaced with F, and the atomic positions and cell parameters were allowed to relax to their lowest energy positions in DFT. The relaxed structures are shown in Figure 5.10 and we confirmed that the bond distances and angles for the relaxed polyethylene and PTFE were realistic by comparison with literature reports. The calculated κ_{DFT} for PTFE was 2.38. As discussed previously, the measured dielectric constants at 10 GHz for paraffin wax (expected to be similar to polyethylene) and PTFE are 2.2 and 2.1, respectively. These observations demonstrate that DFT-calculated values of the dielectric constant for organic molecules are not especially prone to under-estimation or sensitive to small changes in structure, as the predicted dielectric constants for the polymers and the relaxed structure of $Al(HCOO)_3$ show similar levels of accuracy when compared to experimental data. This suggests that there is something unique about the structure of $Al(HCOO)_3$ determined by neutron diffraction which makes its calculated dielectric constant especially sensitive to structural changes.

5.4 Conclusion

In this work we have identified the key characteristics of low-κ materials and suggest an effective workflow for searching for these compounds. Additionally, we highlight both the advantages and drawbacks of empirical and DFT estimates of the dielectric constant. Our results demonstrate that empirical methods are useful for sorting through large databases of candidate low-κ materials, while DFT calculations are better-suited for determining which materials to prioritize. Although it remains challenging to identify materials with dielectric constants lower than that of silica ($\kappa < 3.82$ at 10 GHz), we have found that certain aluminum-based materials are close to achieving these low values. We believe that this is due to the high charge on aluminum and its ability to form open, 3D-connected, networks. In the case of $AlPO_4$, the predicted dielectric constant from DFT calculations was nearly identical to the constant determined from measurements using paraffin pellets and the SPDR. In contrast, for $Al(HCOO)_3$, there was a significant discrepancy between the predicted constant and experiment. This is because even minor changes in the crystal structure seem to contribute to a significantly higher dielectric constant, which is highlighted by calculating the dielectric constant of a DFT-relaxed structure. The relaxed structure shows that even small changes in the O – C – O bonds can result in a much larger dielectric constant.

Chapter 6

Summary and Outlook

In this work, I have shown how the structural and chemical diversity of perovskite-derived crystal structures make them important materials for a number of potential applications. Additionally, I have shown that by making small changes in the composition of these compounds, their properties can be systematically tuned. For example, in Chapter 2, a number of experimental and computational tools were used to show that the incorporation of even small amounts of iodine in the crystal structure of $Cs_3Bi_2Cl_9$ results in a significant change in the crystal structure as well as the optical properties. Similarly, in Chapters 3 and 4, the incorporation of oxygen into the vacancy-ordered perovskite structures of Cs_2WCl_6 and Cs_2MoX_6 causes these materials to exhibit strong near-IR emission. Additionally, the addition of oxygen and resulting change in oxidation state for the W and Mo ions makes the oxyhalide compounds stable under ambient conditions, while the pure halide materials are highly air- and moisture-sensitive. Finally, in Chapter 4, $Al(HCOO)_3$ is shown to have many of the ideal characteristics of a low-dielectric constant material, as it is easy to synthesize, stable, and predicted to have good dielectric properties. However, due to the flexibility of this structure, it is

prone to small distortions which significantly increase the dielectric constant. In the following sections, I will discuss some potential areas for future research based on the results presented here.

6.1 Further exploration of the optical properties of the transition metal oxyhalides

As discussed in Chapter 4, there are still a number of open questions regarding the optical properties of the transition metal oxyhalides. For example, further studies will be required to understand why there are two emission processes active at intermediate temperatures in these materials and whether these processes are related to the change in the trends of the Raman shifts. In addition to resolving mechanistic questions, it will also be of interest to determine the effect of compositional tuning in these compounds. From literature reports, it is clear that it should be possible to form oxyhalide compounds with a range of transition metal ions that are stable in a 5+ oxidation state, but the emission properties of these compounds have not been studied in detail. From the results on the Mo and W compounds, it seems that the identity of the metal has the strongest influence on the emission energy, while the halide ligand determines the energy of the absorption. Therefore, it will be of interest to observe whether this trend holds for other compounds. Furthermore, the role of the *A*-site cation has not yet been determined. Some preliminary work on the compound Rb_2MoOBr_5 has shown that the smaller *A*-site cation causes the oxygen to order as the octahedra become closer together. This yields an orthorhombic unit cell with the space group $Pnma$. Therefore, in the future, the effect of oxygen ordering on the optical emission should be investigated. To conclude, while a number of compositions of oxyhalide compounds

are already known, their optical properties remain relatively underexplored. Exploring emission mechanisms and structure-property relationships in these compounds will lay the foundation for an understanding of an important new class of near-IR emitters.

6.2 Continuing the search for low-κ materials

Although the dielectric properties of $Al(HCOO)_3$ were not as promising as originally expected, our study of this material has revealed some important considerations for the future identification of low-κ materials. For example, in our original screening criteria, we did not consider the importance of surface functionalization. In industrially-relevant materials such as silica particles, the size of the particles is chosen in order to produce homogeneous films and the surface of the particles is modified with small organic chains to enhance compatibility with the polymer epoxy. By producing a suitable interface between the organic and inorganic components, this allows for casting of smooth and homogeneous films. In our work, we found that although ball-milling can be used to obtain particles of the correct size for film-incorporation, a lack of surface-functionalization results in films which are mechanically weak and crack upon curing. Although $Al(HCOO)_3$ contains organic linkers which should facilitate functionalization and film incorporation, it proved challenging to identify synthetic conditions that modified the surface while leaving the bulk structure intact. Therefore, for any new low-κ materials, the ease of surface modification must be considered.

An additional parameter that will be included in future evaluations of low-κ materials is the flexibility of the structure. As demonstrated by the Shannon formula for the prediction of the dielectric constant, some amount of porosity in the crystal structure is desirable for minimizing the dielectric constant, as this lowers the density of the

structure. However, it is simultaneously important for the structure to be mechanically robust so that it can withstand the processing conditions. Additionally, as in the case of $Al(HCOO)_3$, if the structure is too porous or has very limited connectivity, then vibrational motion in the structure may enhance the dielectric constant. This suggests that structures with very large pores, such as many MOF or zeolite materials, may not be suitable as low-κ materials, despite the fact that they seem to fulfill many of the criteria. In summary, future low-κ materials will require both open framework structures and strong bonding within those structures, which is a challenging requirement to meet. These considerations demonstrate why amorphous silica particles remain the material of choice in industrial applications.

6.3 Incorporation of temperature effects in DFT predictions

The final future area of research discussed here will be DFT calculations which go beyond traditional "0 K" DFT calculations in order to more accurately describe the behavior of materials in experiments. While standard DFT calculations are a useful tool for material property prediction and interpretation of experimental data, the results in Chapter 5 and Appendix A highlight that these calculations fall short in cases where dynamics are important. Fortunately, there are a number of possible options in order to include temperature-effects in DFT. In most cases, these calculations involve sampling different structural configurations using Monte Carlo methods, molecular dynamics, or phonon mode calculations and performing the appropriate averaging over these configurations. However, the disadvantage of these methods is that they greatly increase the computational expense for these calculations, even for relatively simple crystal struc-

tures. Additionally, these methods usually rely on harmonic approximations for the atomic motions. Therefore, even calculations which account for temperature effects are prone to a certain amount of error. It remains an open challenge and important area of research to identify efficient ways to predict the temperature-dependence of experimental properties, especially for materials where anharmonicity is significant.

Appendix A

Lattice Dynamics in the NASICON $NaZr_2(PO_4)_3$ Solid Electrolyte from Temperature-Dependent Neutron Diffraction, NMR, and Ab Initio Computational Studies

Natrium super ionic conductor (NASICON) compounds form a rich and highly chemically-tunable family of crystalline materials that are of widespread interest because they include exemplars with high ionic conductivity, low thermal expansion, and redox tunability. This makes them suitable candidates for applications ranging from solid-state

The contents of this chapter have substantially appeared in Reference [183]. Reproduced from: E. E. Morgan, H. A. Evans, K. Pilar, C. M. Brown, R. J. Clément, R. Maezono, R. Seshadri, B. Monserrat, and A. K. Cheetham, Lattice Dynamics in the NASICON $NaZr_2(PO_4)_3$ Solid Electrolyte from Temperature-Dependent Neutron Diffraction, NMR, and Ab Initio Computational Studies *Chem. Mater.* 34, 9 (2022) 4029–4038. This work is open access and uses a Creative Commons public use license.

batteries to nuclear waste storage materials. The key to an understanding of these properties, including the origins of effective cation transport and low, anisotropic (and sometimes negative) thermal expansion, lies in the lattice dynamics associated with specific details of the crystal structure. Here, we closely examine the prototypical NASICON compound, $NaZr_2(PO_4)_3$, and obtain detailed insights into such behavior via variable-temperature neutron diffraction and ^{23}Na and ^{31}P solid-state NMR studies, coupled with comprehensive density functional theory-based calculations of NMR parameters. Temperature-dependent NMR studies yield some surprising trends in the chemical shifts and the quadrupolar coupling constants that are not captured by computation unless the underlying vibrational modes of the crystal are explicitly taken into account. Furthermore, the trajectories of the sodium, zirconium, and oxygen atoms in our dynamical simulations show good qualitative agreement with the anisotropic thermal parameters obtained at higher temperatures by neutron diffraction. The work presented here widens the utility of NMR crystallography to include thermal effects as a unique probe of interesting lattice dynamics in functional materials.

A.1 Introduction

The crystal structure of $NaZr_2(PO_4)_3$ was first reported in 1968 [184] and attracted renewed interest beginning in 1976, as $NaZr_2(PO_4)_3$ displayed exceptional ionic conductivity [185, 186] and low coefficients of thermal expansion. [187] These NASICONs — from natrium super ionic conductors — have been established as promising materials for a variety of applications, most notably in the field of energy storage. [188–190] The original family of NASICON materials have the general formula $Na_{1+x}Zr_2P_{3-x}Si_xO_{12}$, where the two end-member crystal structures are shown in Fig-

ure A.1. These structures are both comprised of a network of corner-sharing MO_6 octahedra and XO_4 tetrahedra, in which the combination of two MO_6 octahedra joined by three XO_4 tetrahedra forms the characteristic "lantern" subunits. The compounds adopt the spacegroup $R\bar{3}c$ (or lower symmetry sub-groups thereof), with the lantern subunits stacked parallel to the [001] direction in the hexagonal setting. These subunits form an open structure such that up to four Na^+ cations can be accommodated in the interstitial spaces. The stoichiometry of the compound can be used to tune the mobility of these ions, and many substitutions are possible on the atomic positions, following the overall formula $A_xMM'(XO_4)_3$. In turn, these substitutions enable the precise tuning of properties such as ionic and electronic conductivity and thermal expansion, making these ideal materials for solid-state electrolytes, electrodes, [188–190] and nuclear waste storage. [191] Many compositions of the NASICON structure have been synthesized and characterized since its discovery, and computational studies continue to highlight new phases for use in these applications, [192–194] illustrating the thriving interest in this class of compounds.

The most well-known application for NASICON compounds is for use in batteries, where the versatility of the crystal structure makes it suitable as both an electrolyte and electrode material for lithium- and sodium-ion batteries. In addition to the zirconium-based family of materials, some other common compositions include NASICONs containing iron, vanadium, and titanium. [188–190] For example, $Na_3MnZr(PO_4)_3$ has been recently reported as a potential high-voltage cathode material for sodium-ion batteries [196], while $Na_3Ti_2(PO_4)_3$ has been proposed for low-voltage anode applications. [197] Similarly, $LiZr_2(PO_4)_3$ [198] and $Li_{1.3}Al_{0.3}Ti_{1.7}(PO_4)_3$ [199] are promising electrolytes for all-solid-state lithium batteries. The flexibility of the NASICON structure has also allowed for the development of battery materials containing mobile divalent

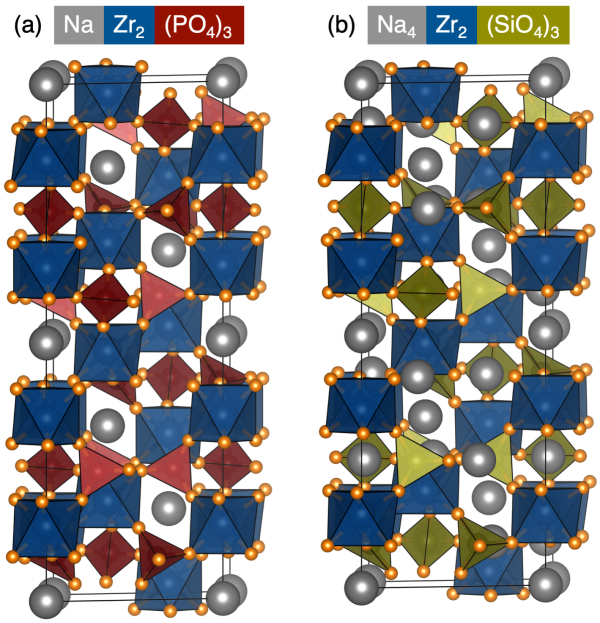

Figure A.1: The two end members of the $Na_{1+x}Zr_2P_{3-x}Si_xO_{12}$ family of compounds: (a) $NaZr_2(PO_4)_3$. [186] (b) $Na_4Zr_2(SiO_4)_3$. [195]

cations, such as calcium [200] or zinc. [201] Finally, in some recent studies, NASICON compounds have also been examined for applications in unconventional battery architectures, such as seawater [202] or redox-flow batteries. [203]

In addition to their tunable ionic and electronic conductivity, one of the key characteristics that makes NASICON compounds desirable for energy storage is their low thermal expansion. In NASICON-type materials, systematic lattice substitutions, diffraction, and dilatometry experiments have been used to construct a model for the thermal expansion behavior. [187, 204–210] These studies have shown that when temperature is increased, the Na^+ sites become larger and the Na-O bond distances increase, driving an expansion along the *c* axis. In order to minimize distortions of the ZrO_6 octahedra and PO_4 tetrahedra, the polyhedra undergo coordinated rotations with respect to one another, resulting in a decrease in the *a* lattice parameter. Depending on the specific composition of the NASICON material, the relative magnitudes of the changes in the

a and *c* lattice parameters can vary, causing the thermal expansion to be negative, positive, or nearly zero. [205]

While static models have been successful in explaining the low thermal expansion of NASICON materials, understanding local dynamics in the crystal structure is essential to explaining the mechanisms of ion conduction. As discussed in a recent review, [211] phonon mode calculations may provide a promising route for the discovery of new solid-state electrolytes. For example, it has been shown that there is good correlation between the frequency or amplitude of certain phonon modes and activation energies for diffusion or migration barriers in systems such as cubic metals, [212] metal halides, [213] and Ruddlesden-Popper phases. [214] While these parameters are computationally accessible, they can be more difficult to observe directly in experiment, generally requiring the use of inelastic neutron or X-ray scattering. [211] In NASICON materials, dynamics have successfully been used to understand the diffusion of Na^+ ions in the compounds $Na_3Sc_xZr_{2-x}(SiO_4)_{2-x}(PO_4)_{1+x}$ and $Na_2Sc_yZr_{2-y}(SiO_4)_{1-y}(PO_4)_{2+y}$. [215] In these materials it was shown that higher concentrations of Sc^{3+} increase the activation energy for ion diffusion, resulting in a lower ionic conductivity. Furthermore, while long-range Na^+ diffusion occurs via three-dimensional pathways, diffraction data and NMR relaxation measurements show that local motion of the Na^+ ions is two-dimensional, which is important in modeling the hopping of the Na^+ ions between sites. These studies illustrate the value of connecting local structural dynamics with bulk material properties such as conductivity.

Both the exciting ionic conductivity and low thermal expansion of NASICON materials, as well as past work on their structure-property relationships, have motivated us to examine the structure of the parent compound, $NaZr_2(PO_4)_3$, more closely, using a combination of powder neutron diffraction, solid-state NMR, and DFT calculations.

These techniques can be used to gain insight into how local dynamics describe ionic conductivity and thermal expansion in this class of materials. Overall, the results of the neutron diffraction study are consistent with previous models of thermal expansion in $NaZr_2(PO_4)_3$, with the *a* lattice parameter decreasing as the temperature is increased from 25 K to 400 K, while the *c* lattice parameter increases over this same temperature range. Additionally, the atomic displacement parameters (ADPs) for each site were determined for each temperature, and the values were compared with the results of DFT phonon mode calculations. Variable temperature ^{23}Na and ^{31}P NMR experiments from 100 K to 300 K revealed a systematic increase in the ^{31}P chemical shift and ^{23}Na C_Q parameter (which describes the asymmetry of the charge distribution around the ^{23}Na site) that reflects changes in the dynamics of this material over this temperature range. In light of these results, static DFT calculations were performed to predict NMR parameters for the neutron structures obtained at various temperatures. These calculations, which did not account for thermal motion, did not reproduce the experimental trends, providing evidence that the trend in the NMR parameters is not exclusively due to the thermal expansion of the lattice, but instead reflects the effects of vibrational motion on local atomic environments. Additional calculations were therefore performed which incorporated both the thermal expansion of the lattice and phonon modes into the prediction of NMR parameters. In this case, the experimental trends were reproduced qualitatively.

A.2 Experimental Methods

A.2.1 Synthesis of $NaZr_2(PO_4)_3$

Solid-state synthesis of $NaZr_2(PO_4)_3$ was based on the original synthesis reported by Hong [186]. 2.34 mmol (0.2484 g) Na_2CO_3, 8.16 mmol (1.0056 g) ZrO_2, and 12.23 mmol (1.6156 g) $(NH_4)_2HPO_4$ were combined and ground in a mortar and pestle for 20 minutes. The powder was placed in an alumina crucible and heated to 1273 K (1000 °C) at a rate of 4 K per min. The temperature was held at 1273 K (1000 °C) for 16 hours before cooling to room temperature. Synthesis was performed by Dr. Kartik Pilar.

A.2.2 Powder neutron diffraction and Rietveld refinements

Measurements were performed on 1.7 g $NaZr_2(PO_4)_3$ by Dr. Hayden Evans at the National Institute of Standards and Technology Center for Neutron Research (NCNR). Data were collected at the high-resolution neutron powder diffractometer, BT-1, utilizing a Cu(311) monochromator with an in-pile 60' collimator, corresponding to a neutron wavelength of 1.540 Å. The sample was loaded into a vanadium sample can in a He-environment glovebox and sealed with an indium o-ring onto a copper heating block. After mounting the sample onto a bottom-loaded closed cycle refrigerator (CCR), the sample was cooled and then measured upon heating upwards from 25 K to 400 K. Data were collected for at least 4 hours for each temperature point.

The powder neutron diffraction data were analyzed using the GSAS software suite. [39] Initial Le Bail refinements were conducted to determine lattice parameters and peak shapes. [34] Background, zero-point error, atomic positions, and isotropic ADPs

were refined for all Rietveld refinements in space group $R\bar{3}c$ (167). For the 100 K through 400 K data sets, anisotropic ADPs were refined for the sodium site. Additionally, for the 325 K and 400 K data sets anisotropic ADPs were also refined for the oxygen and zirconium sites. Isotropic ADPs were used for all other temperatures and sites not specified here. All refinements were performed by Dr. Hayden Evans. Crystal structures were visualized using the VESTA software package. [99]

A.2.3 NMR measurements

NMR spectra were acquired in the temperature range of 100 K to 300 K using a Bruker 400 MHz (9.4 T) Ascend DNP-NMR spectrometer equipped with a 3.2 mm MAS DNP-NMR triple resonance broadband X/Y/H magic angle spinning (MAS) probe while spinning at a rate of 8 kHz. At each temperature point, the sample temperature was calibrated using the T_1 of ^{79}Br in KBr. [216] For the ^{23}Na measurements, the probe was tuned to 105.9 MHz and a zg experiment with a $\pi/2$ pulse of 6 μs at 10 W was used to selectively excite the central transition. The recycle delay was set to 40 seconds. ^{23}Na spectra are reported with respect to the chemical shift of a 1.0 M solution of NaCl in water set to 0 ppm. For ^{31}P spectra, the probe was tuned to 162.0 MHz and a zg experiment with a $\pi/6$ pulse of 1 μs at 160 W was used. The recycle delay was set to 200 seconds. All ^{31}P spectra are reported with respect to the chemical shift of solid triphenylphosphine set to -9 ppm. Spectra were simulated using the SOLA module in the TopSpin software package.

A.2.4 DFT calculations

For both the standard and finite temperature NMR calculations, chemical shifts and quadrupolar coupling constants were determined using density functional theory [55, 56], the PBE functional [58], and the GIPAW formalism [74, 217] as implemented in the CASTEP package, [218] using an energy cutoff of 800 eV, a $\mathbf{k}$-point grid spacing of $2\pi \times 0.025\,\text{Å}^{-1}$ [169], and ultrasoft pseudopotentials[64]. For structure relaxations, the cell parameters were fixed to the experimentally measured values at each considered temperature, and the internal coordinates of the atoms were relaxed until all forces were smaller than 10^{-4} eV/Å.

Phonon calculations were performed using the finite displacement method [219] in conjunction with nondiagonal supercells. [220] The calculations revealed the presence of imaginary modes at a few $\mathbf{q}$-points located at the Brillouin zone boundary. A mapping of the energy as a function of the amplitude of the imaginary modes showed a shallow quartic double-well potential. The self-consistent harmonic approximation was then applied to the individual imaginary modes, [221, 222] and as a result the imaginary frequencies became real at all finite temperatures considered in this work. These results indicate that anharmonic lattice dynamics are necessary to stabilize the structure.

In the finite temperature calculations, the calculated phonon modes were then used to stochastically generate atomic positions distributed according to the vibrational density at the corresponding temperature, [77] and accelerated using thermal lines. [223, 224] The finite temperature NMR parameters were calculated with appropriate averages over configurations. All phonon calculations and finite temperature NMR calculations were performed by Dr. Bartomeu Monserrat at Cambridge University. The

atomic positions generated in this process were visualized using the OVITO software package. [225] For the finite temperature calculations, the chemical shielding was converted to chemical shift using the formula: $\delta = \sigma^{\mathrm{ref}} - \sigma$, where σ^{ref} was chosen such that the calculated shift for the 100 K structure would correspond to that observed experimentally near 100 K. For the standard DFT calculations, in order to convert from the calculated chemical shielding to an experimental chemical shift, calibration curves were constructed by plotting the calculated shielding for several relevant phosphates and sodium-containing compounds against their experimental chemical shift values from the literature. [226–231]

A.2.5 Chemical shift calibration curves for Model 1 and Model 2

In order to construct the chemical shift calibration curves for Models 1 and 2 shown in Figures A.2 and A.3, crystal structures were obtained from the Inorganic Crystal Structure Database. [184, 232–261] For Model 1, structures were downloaded and converted to the .cell file format using the CIF2Cell python package. [262] For Model 2, the same structures were first relaxed in the Vienna Ab initio Simulation Package [51–53] using the recommended PAW potentials, [66, 100] an energy cutoff of 600 eV, and a k-point grid with length parameter of 40. [169] The lattice parameters were held fixed at the experimentally-determined values and the internal coordinates of the atoms were relaxed until all forces were smaller than 10^{-4} eV/Å. Following relaxation, each structure was converted to the .cell file format in order to perform the NMR calculations. Chemical shifts calculations were then performed in the CASTEP package in the same way as described above.

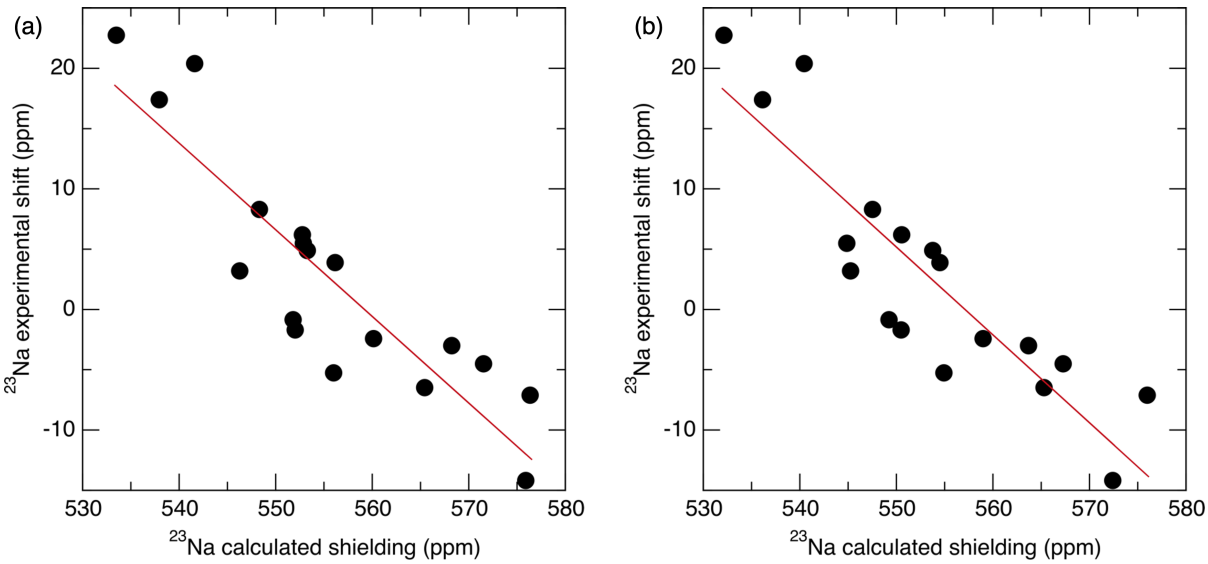

Figure A.2: ^{23}Na chemical shift calibration curves used in (a) Model 1 (unrelaxed structures). The regression line has a slope of -0.71842, an intercept of 401.74 ppm, and a correlation coefficient of -0.8919. (b) Model 2 (relaxed structures). The regression line has a slope of -0.72852, an intercept of 405.86 ppm, and a correlation coefficient of -0.8891.

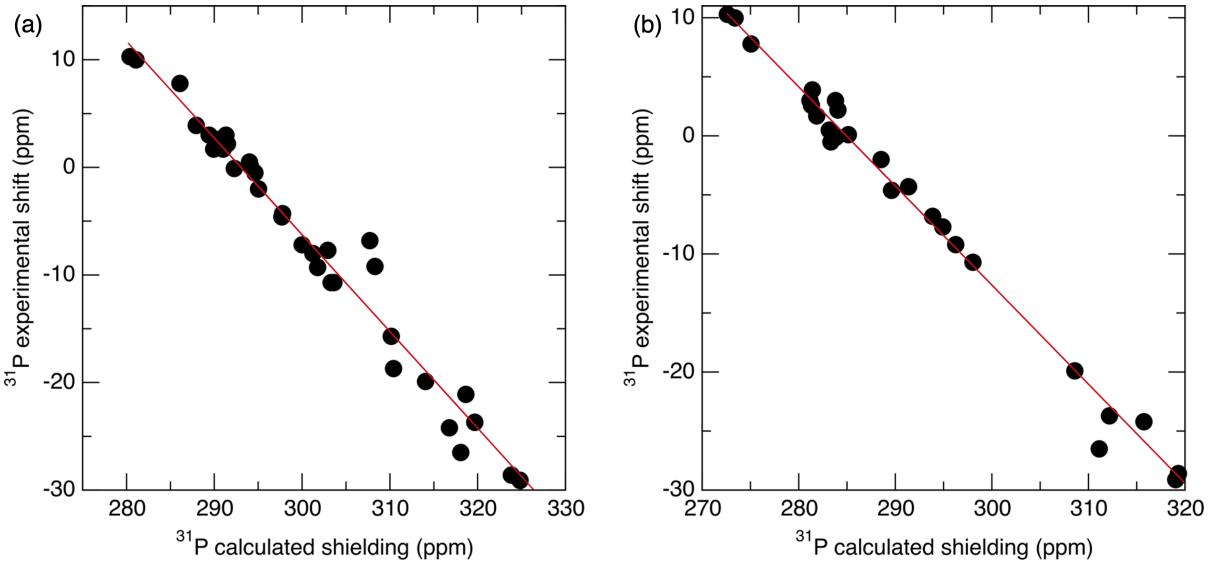

Figure A.3: ^{31}P chemical shift calibration curves used in (a) Model 1 (unrelaxed structures). The regression line has a slope of -0.89933, an intercept of 263.54 ppm, and a correlation coefficient of -0.9885475. (b) Model 2 (relaxed structures). The regression line has a slope of -0.83908, an intercept of 239.09 ppm, and a correlation coefficient of -0.9954.

A.3 Results and Discussion

As shown in Figure A.4, powder neutron diffraction data were collected for $NaZr_2(PO_4)_3$ between 25 K and 400 K. Rietveld refinements were performed for each data set in order to determine the lattice parameters, atomic positions, and atomic displacement parameters for the structure as a function of temperature. The calculated differences between the experimental data and the Rietveld refinements illustrate the high quality of both the data and the fits.

The structures determined from the Rietveld refinements are in good agreement with previous studies of the NASICON family. The structure is comprised of chains of corner-sharing ZrO_6 octahedra and PO_4 tetrahedra which form an open network, with Na^+ localized in octahedral sites at $(0, 0, 0)$, as shown in Figure A.5 (a). In Si-substituted members of the NASICON family, the Na^+ ions occupy a second site in the structure in order to balance the added charge from the Si^{4+}; however, in $NaZr_2(PO_4)_3$ there was no evidence for Na^+ occupation of this second site, even at high temperatures. Additionally, the thermal expansion behavior of this material is consistent with earlier reports. [187] Upon heating from 25 K to 400 K, the *a* lattice parameter decreases from 8.81101(11) Å to 8.79945(18) Å, while the *c* lattice parameter increases from 22.6859(5) Å to 22.8199(7) Å. As a result, the volume of the unit cell increases by only 0.33% over this temperature range, as illustrated in Figure A.5 (b).

Figure A.6 shows representative fragments of the structure at 100 K and 325 K, where these temperatures were selected because this is the range of temperatures that were later accessible in the NMR studies. These fragments illustrate several important features of the structure and its thermal expansion behavior. First, the sodium sites expand with increasing temperature, with the sodium-oxygen bond distance in-

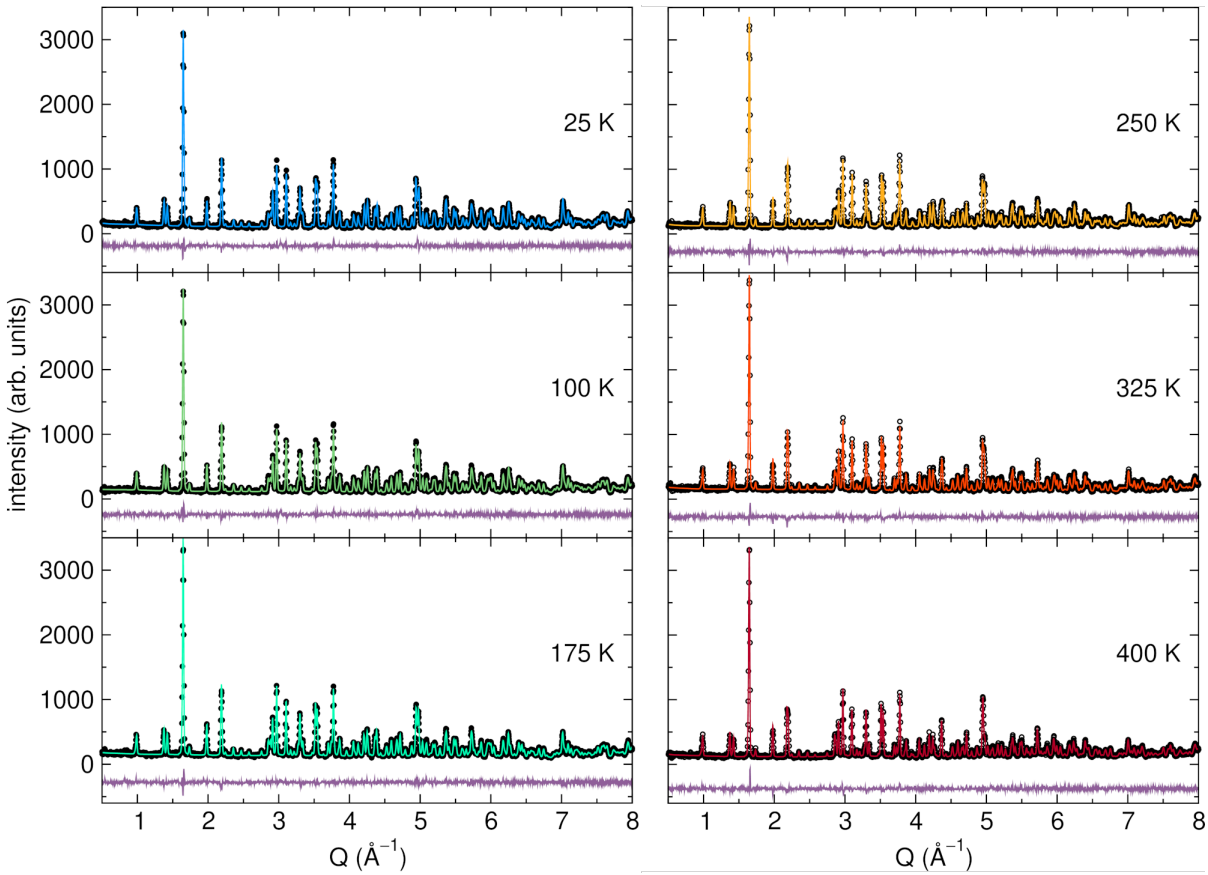

Figure A.4: Neutron diffraction data (BT-1, NCNR, wavelength = 1.540 Å) as a function of Q (defined as $2\pi/\lambda$) and Rietveld refinements at temperatures from 25 K to 400 K. Black circles represent the experimental data while colored lines represent the Rietveld refinement fits. The purple line below shows the difference between experimental data and Rietveld refinement fits. The Rietveld refinement statistics for each fit are 25 K: R_{wp} = 7.18%, R_p = 5.82%; 100 K: R_{wp} = 6.91%, R_p = 5.63%; 175 K: R_{wp} = 6.76%, R_p = 5.56%; 250 K: R_{wp} = 6.99%, R_p = 5.77%; 325 K: R_{wp} = 6.66%, R_p = 5.42%; 400 K: R_{wp} = 6.80%, R_p = 5.56%. Neutron diffraction and Rietveld refinements performed by Dr. Hayden Evans.

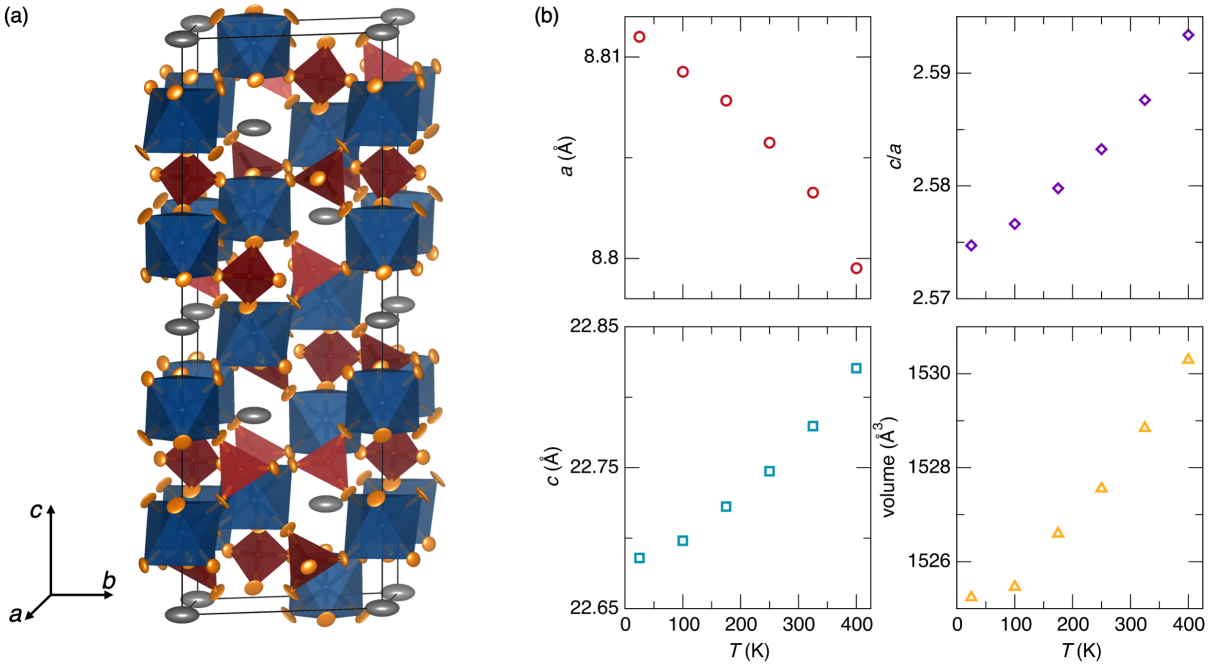

Figure A.5: (a) Representative crystal structure for $NaZr_2(PO_4)_3$ at 325 K with atomic displacement parameters shown at 95%. Anisotropic parameters were refined for the sodium, oxygen, and zirconium sites, while isotropic parameters were used for the phosphorous site. (b) Lattice parameters and cell volumes for $NaZr_2(PO_4)_3$ at temperatures from 25 K to 400 K. Error bars representing one standard deviation are commensurate with symbol size.

creasing from 2.5345(13) Å at 100 K to 2.5643(18) Å at 325 K (+0.0298 Å, +1.18%). Further details of the changes in the bond lengths with temperature can be found in Appendix B Furthermore, the ADPs indicate that as the temperature increases, the Na atom spends a greater amount of time away from the high-symmetry $(0, 0, 0)$ position. The U value for sodium increases from 0.0133 $Å^2$ at 100 K to 0.0450 $Å^2$ at 325 K. Furthermore, the sodium site becomes more anisotropic, with the ratio U_{11}/U_{33} increasing from 2.31 to 4.00. In contrast, the phosphorous and zirconium sites show only small changes. At 100 K the two unique P-O bond distances in the structure are 1.5262(18) Å and 1.5289(16) Å, while at 325 K the bond distances are 1.526(3) Å and 1.525(3) Å (changes of -0.0002 Å , -0.01% and -0.0039 Å, -0.26%, respectively). Similarly, the zirconium-oxygen bond distances remain constant or decrease slightly with temperature. At 100 K the two unique Zr-O bond distances are 2.040(2) Å and 2.0937(18) Å, and at 325 K they are 2.041(3) Å and 2.085(3) Å (changes of +0.001 Å, +0.05% and -0.0087 Å, -0.4%, respectively). In both the PO_4 and ZrO_6 polyhedra, the bond angles change only slightly over this temperature range. This confirms earlier assumptions in the literature that, based on average bond distances, the PO_4 tetrahedra and ZrO_6 octahedra undergo only very small distortions over the range of temperatures studied.

In order to further investigate the changes in atomic motion and local distortions with temperature, the DFT phonon mode calculations were used as a starting point to generate 1000 structures at each temperature in which the atomic positions are distributed according to the harmonic density. The resulting structures are overlaid in order to visualize the thermal motion, as shown in Figure A.6.

This figure illustrates the good agreement between the neutron and computational data, particularly for the sodium site, where the configurations generated from DFT also show a significant increase in the size and anisotropy of the sodium site. For this

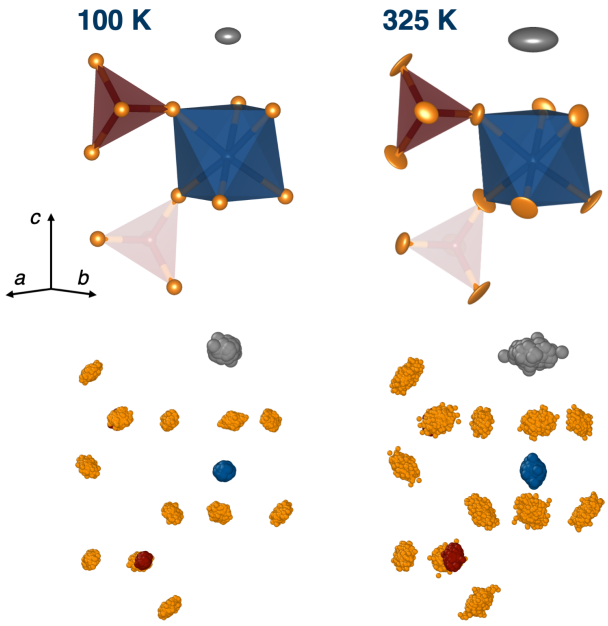

Figure A.6: Representative sections of the crystal structure for $NaZr_2(PO_4)_3$ at 100 K and 325 K. The top portion of the figure shows the structure determined from the neutron refinements, with atomic displacement parameters shown at 95%. In the 100 K structure, anisotropic ADPs were refined only for the sodium site, and isotropic ADPs were used for all other sites. At 325 K, anisotropic parameters were refined for the sodium, oxygen, and zirconium sites, while isotropic parameters were refined for phosphorous. The bottom portion of the figure shows images composed of 1000 structures which were stochastically generated following the atomic distribution as determined by the DFT phonon calculations. These phonon calculations were performed by Dr. Bartomeu Monserrat In these structures each individual atom is shown at 10% of its default radius in order to clearly visualize the shape of each cluster.

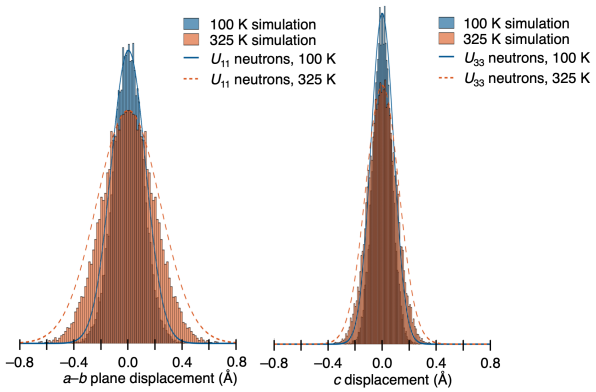

Figure A.7: Histograms depicting the distribution of displacements away from the equilibrium position for the sodium site in the *a*-*b* plane and *c* direction at 100 K and 325 K. The overlaid curves represent the expected distribution of positions based on the U_{11} and U_{33} values from the neutron refinements at 100 K and 325 K.

site, it was also possible to perform a more detailed quantitative comparison between the U values from the neutron structures and the displacements of the atoms in the computational results, as shown in Figure A.7. The histograms clearly show the similarity between the computational distribution of sodium positions and the distribution that would be expected based on the U_{11} and U_{33} values determined from the neutron refinements. There are some minor discrepancies between the two, with the computational mean squared displacements tending to be smaller than the corresponding experimental U values. The best agreement between the two is found at lower temperatures, indicating that anharmonic thermal motion becomes important at the higher temperature range. Additional information about the ADPs at various temperatures and comparison with the mean-squared displacements from DFT can be found in Appendix B

The computational positions for the phosphorous and zirconium sites agree qualitatively with the neutron data, although the mean squared displacements from the computational data are significantly larger than the U_{iso} values obtained from the neutron refinements. In both data sets, the phosphorous and zirconium sites have smaller

mean squared displacements which increase a small amount with temperature in comparison with the sodium and oxygen sites. Additionally, in the case of the zirconium site which displays some anisotropy at higher temperatures, both the neutron ADPs and the computational mean squared displacements show a greater degree of motion along the *c* axis than in the *a*-*b* plane. Finally, computational and neutron results for the oxygen positions are qualitatively similar, although comparison with the neutron ADPs is slightly complicated by the fact that oxygen anisotropic ADPs could only be refined for the 325 K and 400 K data sets. For the lower temperature data sets the anisotropic ADPs became physically unrealistic, and therefore isotropic ADPs were determined to be more appropriate. In the computational data, the average mean-squared displacement from the equilibrium positions increases by a factor of three between 100 K and 325 K, and the distribution becomes more anisotropic as the temperature increases. In the neutron refinements, the U values are much smaller than the mean-squared displacements in the computational data, but the U_{iso} values do increase by a factor of two between 100 K and 325 K. Additionally, the orientations of the neutron ADPs in the 325 K data set appear to be qualitatively similar to the distributions predicted by computation.

Variable-temperature NMR experiments provide an effective way to probe the influence of temperature on local structure and dynamics in a material. The spectra for ^{31}P and ^{23}Na taken between approximately 100 K and 300 K are shown in Figure A.8. These spectra display several interesting trends over the range of temperatures measured. First, because ^{23}Na has a nuclear spin of $I = 3/2$, it is a quadrupolar nucleus and therefore is described in terms of both its chemical shift tensor and electric field gradient tensor. Simulations of the spectra indicate that the isotropic chemical shift increases slightly from -14.23 ppm to -14.18 ppm between 100 K and 300 K. For quadrupolar

nuclei, the observed chemical shift is the sum of the isotropic chemical shift and the second-order quadrupolar shift; however for simplicity we focus on the isotropic shift here. Additionally, the quadrupolar coupling constant, C_Q, which describes the width of the line shape, increases from 1.96 MHz to 2.24 MHz. Initially, the trends in NMR parameters were compared with the structures from the neutron diffraction data and trends in NMR parameters from previous studies of similar materials. While some of the trends could be rationalized using this strategy, the cause of others remained unclear. For example, given the significant increase in the Na-O bond distances between 100 K and 300 K, a larger change in the chemical shift was anticipated. Additionally, previous studies of the NMR parameters of sodium silicates found that the chemical shift decreases with increasing Na-O bond length, [227] so it was unexpected that the chemical shift increased slightly instead. The C_Q parameter reflects the asymmetry of the charge distribution around the ^{23}Na site, where lower values of the coupling constant indicate a more symmetrical site. The increase in C_Q is consistent with the results of the neutron diffraction, which show the Na vibrations becoming more anisotropic at higher temperatures (Figure A.6).

In the ^{31}P spectra there is a significant increase in the isotropic chemical shift, from -24.19 ppm to -23.66 ppm. In this case, the chemical shift was not expected to change significantly with temperature, as neutron diffraction data indicated that the PO_4 tetrahedra are fairly rigid. There have been several investigations of strategies for interpreting and predicting the ^{31}P chemical shifts in phosphates; however, they cannot completely explain the trends observed for $NaZr_2(PO_4)_3$. [228, 263–266] For example, Cheetham *et. al.* [226] found that weaker P-O bonds are associated with larger chemical shifts, but given the fact that there is no strong trend in the average bond distances, it is unlikely that this is the correct explanation for our $NaZr_2(PO_4)_3$ results.

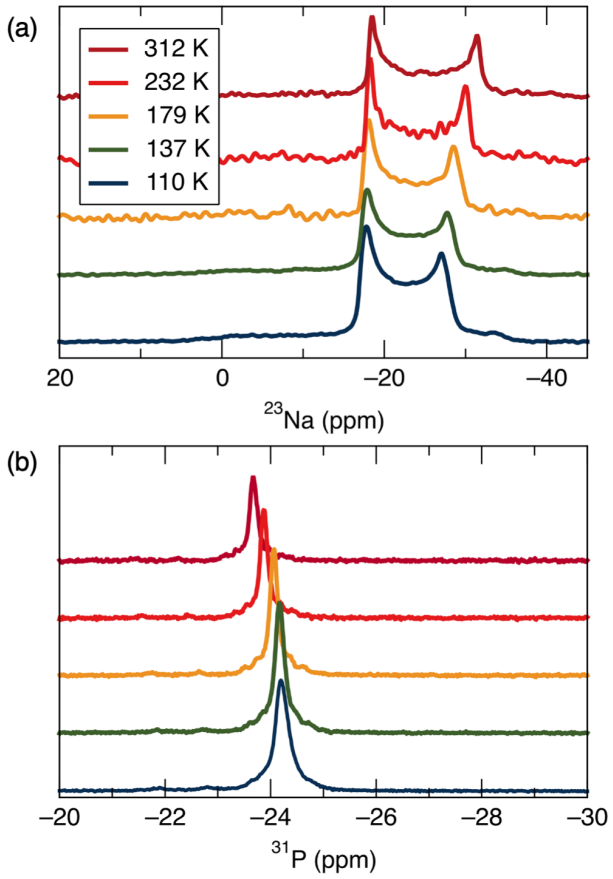

Figure A.8: (a) Variable temperature ^{23}Na spectra. (b) Variable temperature ^{31}P spectra.

Given that the trends in the NMR data could not be completely explained by the neutron diffraction structures, DFT calculations were performed to predict the NMR parameters at each temperature. Three different strategies for calculating the NMR parameters were attempted. For Model 1, the NMR parameters were directly calculated from the neutron structures, which should capture any trends in the chemical shift or C_Q values due to the thermal expansion of the lattice. In Model 2, a DFT structural relaxation was performed for each neutron structure where the lattice parameters were fixed at each temperature and the atomic positions allowed to relax, followed by the NMR calculation. This technique was chosen because several studies on performing DFT calculations of NMR parameters have shown that the agreement between theory and experiment can be improved significantly by using relaxed structures. [263, 267] Finally, in Model 3, the NMR parameters were determined by averaging over the stochastic positions generated by the previously-discussed phonon mode calculations, in order to incorporate the effects of both the thermal expansion of the lattice and atomic vibrations.

The results of these three sets of calculations and comparison with the experimental results are shown in Figure A.9. Beginning with Model 1, it is clear that these results do not correspond well with what is observed experimentally, but they are similar to what might be predicted exclusively based on the thermal expansion of the lattice. For example, the ^{23}Na chemical shift decreases significantly with temperature and increasing Na-O bond length, which is similar to what has been observed experimentally in other systems. Additionally, there is not a strong trend in the C_Q parameter, which makes sense because this type of DFT calculation cannot incorporate the information communicated by the atomic displacement parameters. The ^{31}P chemical shift does not change with temperature, which is also what could be predicted from the neutron

structures. These results further illustrate the point that the observed NMR trends do not simply originate from the thermal expansion of the lattice. We note here that trends in calculated chemical shifts can depend somewhat on the method used to convert between chemical shielding and chemical shift. In this work we use the calibration curves discussed in the Methods section and have confirmed that the general trends observed in Models 1 and 2 do not change significantly when other re-scaling methods are used. More detail can be found in the Supporting Information.

Considering Model 2, the trends seem to be slightly closer to those observed experimentally, but there remains a significant difference between the two. The relaxed results show a very small increase in both the ^{23}Na C_Q and the ^{31}P chemical shift. These trends qualitatively match experimental results, but in both cases the magnitude of the increase is much less than that found in experiment. In the case of the sodium, the Na-O bonds in the relaxed structures are shorter than in the neutron structures and do not increase as much with temperature (relaxed distances are 2.4879 Å and 2.4965 Å at 100 K and 325 K). This is consistent with the fact that the ^{23}Na chemical shift shows a smaller decrease than is found in Model 1, but is still far from matching the experimental results. Similarly, the P-O distances distances were both 1.5408 Å at 100 K and 1.5410 Å and 1.5409 Å at 325 K, which may account for the small increase in ^{31}P chemical shift. Overall, however, due to the subtle changes in the structure upon relaxation, it is difficult to conclusively determine which aspects of the structural relaxation contribute to the differences in the NMR parameters between Models 1 and 2. This is similar to the findings of other DFT studies of phosphates, where structural relaxations significantly improve the correlation between experimental and predicted chemical shifts, despite the fact that the NMR chemical shifts are measured at ambient temperature while these DFT calculations do not explicitly account for thermal effects

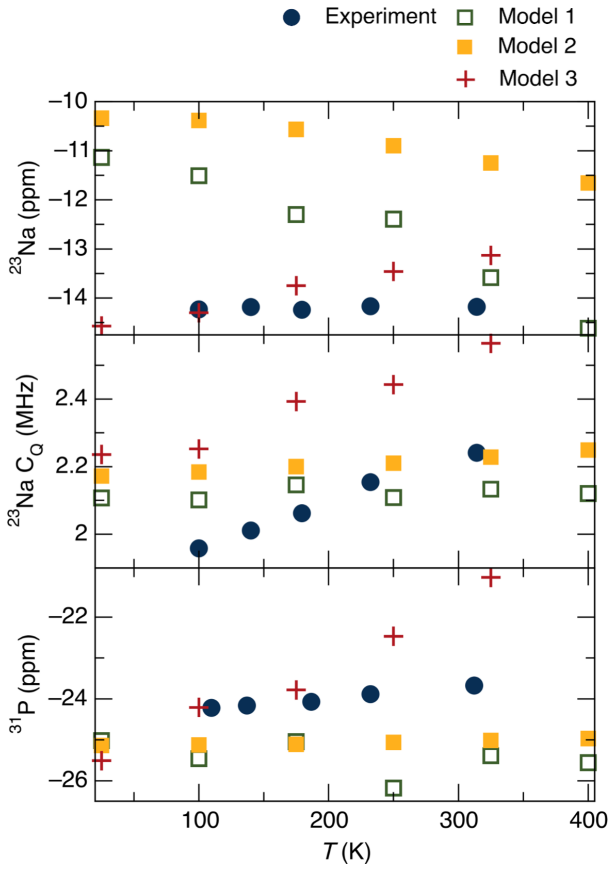

Figure A.9: Comparison of experimental NMR parameters with those predicted by DFT at different levels of theory. DFT calculations for Model 3 were performed by Dr. Bartomeu Monserrat.

associated with atomic vibrations. [263]

While NMR calculations from relaxed structures show slightly better performance than those from diffraction-based structures, these calculations do not provide a satisfactory explanation for the experimental NMR trends. Therefore, in Model 3, NMR parameters were calculated as thermal averages over the atomic vibrational motion for each of the relaxed neutron structures, as described in the Methods section. As shown in Figure A.9, the results of Model 3, which explicitly account for thermal motion in the structures, show better qualitative agreement with our experimental trends. For the chemical shifts, the magnitudes of the calculated shifts are less meaningful in some

ways because the value of σ^{ref} was chosen somewhat arbitrarily, as described in the Methods. This differs from Models 1 and 2, where a calibration curve was used to determine this value. However, more significant is the fact that the finite temperature calculations predict an increase in both chemical shifts, as well as the C_Q value. Although it is difficult to directly link aspects of the computationally-generated structures to the calculated chemical shifts, the distributions of positions in Figure A.6 suggests that the chemical shift trends could be influenced by the larger and more anisotropic range of displacements observed in the computationally-generated oxygen positions. The clusters of oxygen positions imply that the dominant motion for these atoms is vibration nearly perpendicular to the P-O bond direction. Although the average bond lengths remain nearly constant in the neutron data, in the computational data this motion results in increasing P-O bond lengths with increasing temperature. For example, at 100 K the distance from the computational positions was 1.5456 Å, and at 325 K the average distance was 1.5527 Å (+0.0071 Å, +0.459%). This increase in the effective bond length is consistent with the increase in chemical shift observed in Model 3 and the experimental NMR data. In the case of the Na-O bond lengths, at 100 K the average distance was 2.4941 Å and at 325 K the distance was 2.5134 Å (+0.0193 Å, +0.774%). Although these bond distances don't account for the fact that the sodium chemical shift increases with temperature, it does indicate one potential reason why the change in chemical shift in experiment is smaller than what would be expected from the average bond distances in the neutron structures. Finally, while the values of C_Q are larger in the calculated results, the overall increase with temperature is nearly the same as in the experimental results. Therefore, while none of the NMR DFT calculations provide an exact match between theory and experiment, the Model 3 calculations are the most consistent with experiment and demonstrate that the experimental trends in the NMR parameters between 100 K and 300 K are mainly the result of changes in

dynamics. One potential reason why the trends in the calculated NMR parameters are larger than what is observed experimentally is that Model 3 relies on harmonic or self-consistent harmonic approximations. A more rigorous treatment of anharmonicity would lead to smaller changes in the NMR parameters, as Model 3 likely overestimates the atomic displacements, as evidenced by the fact that the mean squared displacements are larger than the neutron U values for most sites. One way to accomplish this would be to run molecular dynamics (MD) simulations at each desired temperature and subsequently perform NMR calculations on each of the configurations generated. Unfortunately this approach also has two disadvantages: first, MD does not account for quantum zero-point fluctuations unless path-integral MD is used, and second, the use of MD followed by NMR calculations would be extremely computationally expensive. As discussed above, we predict that the inclusion of anharmonicity would lead to improved agreement between experiment and computation, but the computational cost of the calculations would be too large for inclusion in this work.

A.4 Conclusion

In this work we have used variable temperature neutron diffraction, NMR spectroscopy, and three sets of DFT calculations to improve our understanding of the thermal behavior of $NaZr_2(PO_4)_3$. The structures determined from variable temperature neutron diffraction are similar to earlier models of thermal expansion in NASICON materials, where an increase in the Na-O bond distances with increasing temperature leads to an increase in the c lattice parameter, and rotations of rigid PO_4 and ZrO_6 polyhedra cause a decrease in the a lattice parameter. In order to understand the role of atomic vibrations in this model, we performed solid-state NMR experiments and attempted

to use the atomic positions and thermal displacement ellipsoids calculated from the neutron data to interpret our results. Using empirically-derived predictions for NMR parameters based on the neutron data was not successful in explaining the trends in the chemical shifts, so several DFT approaches were used instead. Model 1 matched the previously discussed empirical predictions based on the thermal expansion of the lattice, but did not match the experimental trends. Similarly, Model 2 showed slightly better results after relaxing atomic positions, but did not allow us to identify the specific cause of the trends in the NMR spectra. Finally, the finite temperature calculations in Model 3 produced values for the NMR parameters that matched all trends, at least qualitatively. Additionally, an analysis of the distribution of positions used in these calculations showed that they were consistent with the atomic displacement parameters obtained from the neutron refinements and provided some insight into the superior performance of Model 3. In addition to providing a more complete model for the thermal expansion of $NaZr_2(PO_4)_3$, these results illustrate several important concepts. The first is the sensitivity of solid-state NMR to changes in local dynamics with temperature. Second, these results suggest that first-principles phonon calculations can be useful in the prediction and interpretation of atomic displacement parameters from diffraction experiments. Finally, this work demonstrates the importance of properly accounting for finite temperature effects in DFT calculations of NMR parameters.

Appendix B

Variable-Temperature Rietveld Refinements of $NaZr_2(PO_4)_3$ and Comparison with DFT-Calculated Structures

T (K)	P1-O1 (Å)	P1-O2 (Å)	Zr1-O1 (Å)	Zr1-O2 (Å)	Na1-O2 (Å)
25	1.5272(19)	1.5322(16)	2.045(3)	2.0856(19)	2.5286(13)
100	1.5262(18)	1.5289(16)	2.040(2)	2.0937(18)	2.5345(13)
175	1.522(3)	1.536(2)	2.041(3)	2.092(3)	2.5381(16)
250	1.520(3)	1.530(2)	2.046(3)	2.091(3)	2.5467(16)
325	1.526(3)	1.525(3)	2.041(3)	2.085(3)	2.5643(18)
400	1.526(3)	1.522(3)	2.044(4)	2.083(3)	2.574(2)

Table B.1: Selected bond lengths in the $NaZr_2(PO_4)_3$ crystal structure from 25 K to 400 K. Values in parentheses represent one standard deviation.

T (K)	O1-P1-O1	O1-P1-O2	O2-P1-O2	O1-Zr1-O1	O1-Zr1-O2	O2-Zr1-O2
25	109.98(18)	110.34(8)	109.72(18)	92.19(10)	93.71(7)	83.46(9)
100	109.98(17)	108.13(9)	109.58(18)	92.43(9)	90.47(6)	83.31(9)
175	110.8(3)	110.57(9)	109.3(3)	92.60(11)	90.57(8)	83.21(10)
250	110.4(3)	107.90(12)	109.5(3)	92.30(12)	93.24(9)	83.50(11)
325	110.1(3)	108.30(13)	109.6(3)	92.12(13)	90.59(9)	84.10(12)
400	109.9(3)	108.02(14)	110.2(3)	91.82(13)	90.75(9)	84.32(12)

Table B.2: Selected bond angles in the $NaZr_2(PO_4)_3$ crystal structure from 25 K to 400 K. Values in parentheses represent one standard deviation.

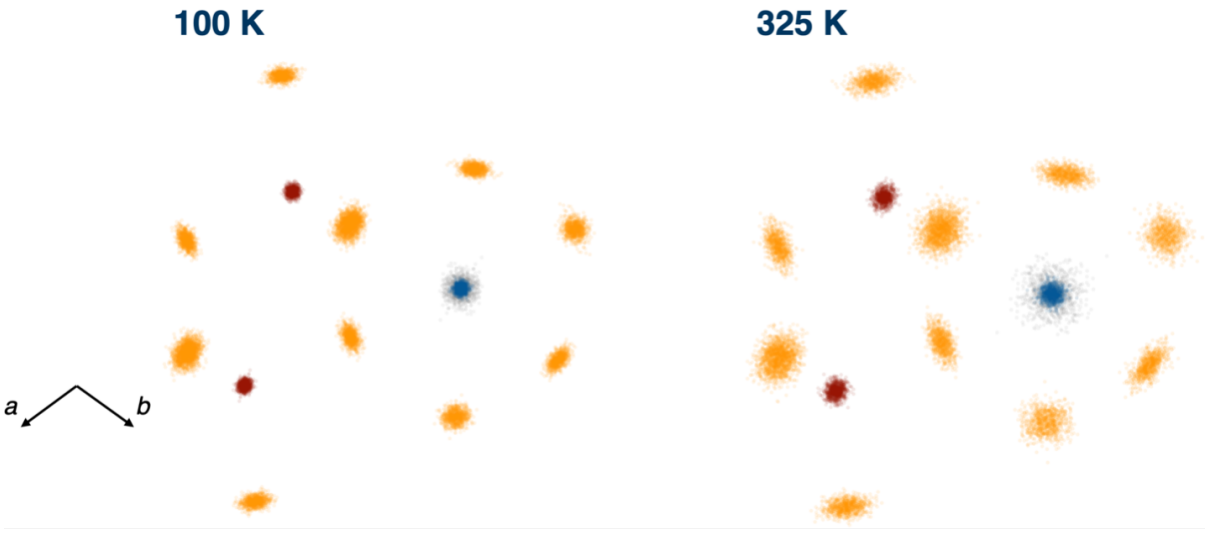

Figure B.1: 2D distribution of computationally-generated atomic positions projected onto the *a*-*b* plane (looking down the *c* axis) at 100 K and 325 K.

T (K)	$<a,b^2>$ (Å^2)	$<c^2>$ (Å^2)	Average mean square displacement (Å^2)	U_{iso} (Å^2)
25	0.0535	0.0541	0.0537	0.0057 0.00575
100	0.0779	0.0747	0.0766	0.006 0.00598
175	0.116	0.132	0.122	0.0072 0.0059
250	0.155	0.174	0.161	0.0102 0.0072
325	0.197	0.218	0.204	0.0135 0.0105
400	0.238	0.267	0.248	0.0161 0.0134

Table B.3: Comparison of mean squared displacements calculated for O with experimental isotropic atomic displacement parameters from neutron refinements.

T(K)	$<a,b^2>$ (Å^2)	$<c^2>$ (Å^2)	U_{11} (Å^2)	U_{22} (Å^2)	U_{33} (Å^2)	U_{12} (Å^2)	U_{13} (Å^2)	U_{23} (Å^2)
325	0.197	0.218	0.0122 0.0056	0.0177 0.0092	0.0129 0.0122	0.0091 0.0003	–0.0071 0.0025	0.0031 –0.0003
400	0.238	0.267	0.0177 0.0073	0.0206 0.0104	0.0125 0.0159	0.0114 –0.0006	–0.0086 0.0029	0.0038 0.0017

Table B.4: Comparison of mean squared displacements calculated for O with experimental anisotropic atomic displacement parameters from neutron refinements.

T (K)	$<a,b^2>$ (Å^2)	$<c^2>$ (Å^2)	$<a,b^2>/<c^2>$	U_{11} (Å^2)	U_{33} (Å^2)	U_{11}/U_{33}
25	0.00747	0.00363	2.06	0.0085	0.0085	1.0
100	0.0121	0.00450	2.69	0.0164	0.0071	2.31
175	0.0195	0.00618	3.16	0.0234	0.0110	2.13
250	0.0273	0.00818	3.34	0.0333	0.0040	8.33
325	0.0362	0.0106	3.42	0.0600	0.0150	4.00
400	0.0453	0.0125	3.62	0.0740	0.0140	5.28

Table B.5: Comparison of mean squared displacements calculated for Na with experimental atomic displacement parameters from neutron refinements.

T (K)	$<a,b^2>$ (Å^2)	$<c^2>$ (Å^2)	Average mean square displacement (Å^2)	U_{iso} (Å^2)
25	0.00498	0.00655	0.00547	0.0039
100	0.00664	0.00870	0.00730	0.0042
175	0.00990	0.0189	0.0129	0.0032
250	0.0126	0.0245	0.0166	0.0047
325	0.0155	0.0302	0.0204	0.0031
400	0.0188	0.0377	0.0251	0.0048

Table B.6: Comparison of mean squared displacements calculated for P with experimental atomic displacement parameters from neutron refinements.

T (K)	$<a,b^2>$ (Å^2)	$<c^2>$ (Å^2)	Average mean square displacement (Å^2)	U_{iso} (Å^2)
25	0.00292	0.00350	0.00311	0.00582
100	0.00455	0.00433	0.00446	0.00458
175	0.00760	0.0122	0.00908	0.0032
250	0.0101	0.0157	0.0119	0.003
325	0.0125	0.0198	0.0148	0.00506
400	0.0148	0.0246	0.0182	0.00548

Table B.7: Comparison of mean squared displacements calculated for Zr with experimental atomic displacement parameters from neutron refinements.

T (K)	$<a,b^2>$ (Å^2)	$<c^2>$ (Å^2)	U_{11} (Å^2)	U_{22} (Å^2)	U_{33} (Å^2)	U_{12} (Å^2)	U_{13} (Å^2)	U_{23} (Å^2)
325	0.0125	0.0198	0.0038	0.0038	0.0076	0.00192	0	0
400	0.0148	0.0246	0.0054	0.0054	0.0056	0.0027	0	0

Table B.8: Comparison of mean squared displacements calculated for Zr with experimental anisotropic atomic displacement parameters from neutron refinements.

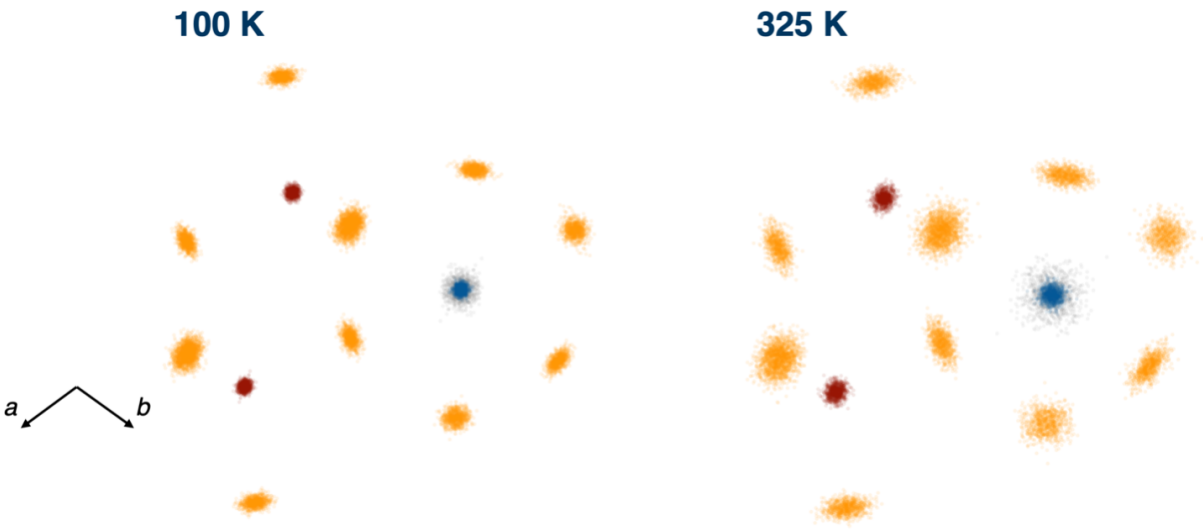

Figure B.2: 2D distribution of computationally-generated atomic positions projected onto the *c* axis (looking along the axis which bisects the *a* and *b* axes) at 100 K and 325 K.

Appendix C

Crystallographic details for $Cs_3Bi_2(Cl_{1-x}I_x)_9$ compounds

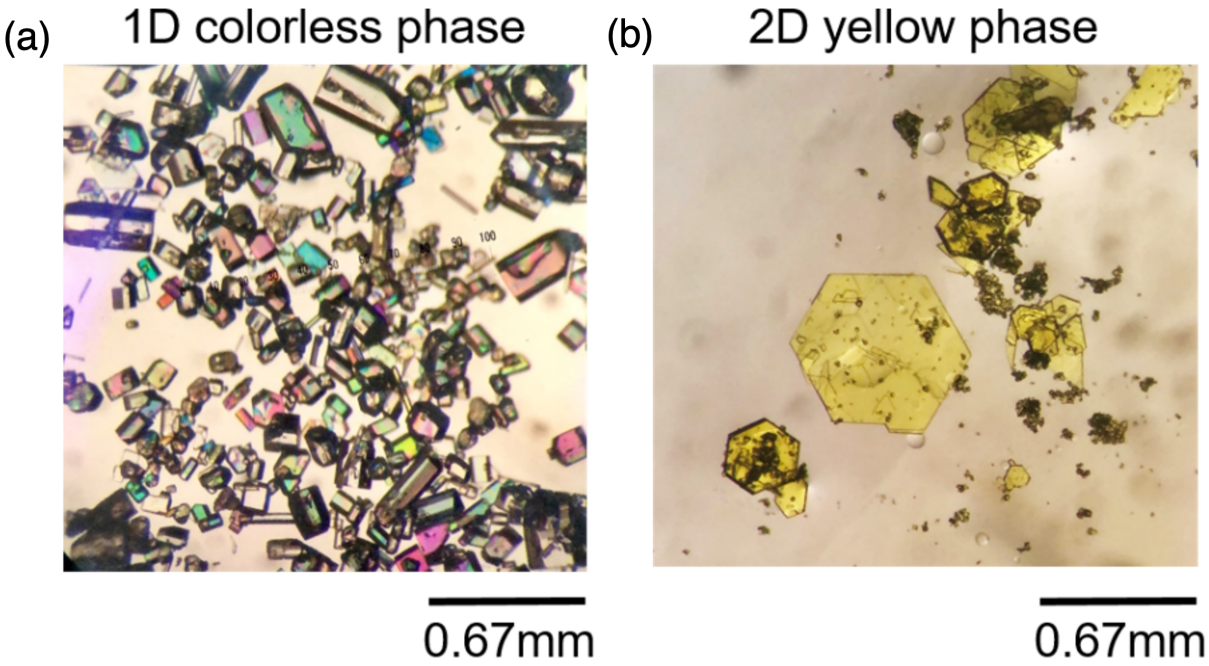

Figure C.1: Optical microscopic images of the (a) 1D colorless phase $Cs_3Bi_2Cl_9$ and (b) 2D yellow phase $Cs_3Bi_2Cl_{8.16}I_{0.84}$.

Label	x	y	z	Occupancy	U_{iso} (Å^2)
Bi(01)	0.6833(1)	3/4	0.4179(1)	1	0.018(1)
Bi(02)	0.4988(1)	1/4	0.2363(1)	1	0.019(1)
Cs(03)	0.9112(1)	1/8	0.5811(1)	1	0.040(1)
Cs(04)	0.7518(1)	1/4	0.2521(1)	1	0.042(1)
Cs(05)	0.9135(1)	3/4	0.892(1)	1	0.044(1)
Cl(06)	0.4200(1)	0.0077(2)	0.1633(2)	1	0.043(1)
Cl(07)	0.5885(2)	0.5032(2)	0.3321(2)	1	0.053(1)
Cl(08)	0.5797(2)	1/4	0.0820(2)	1	0.045(1)
Cl(09)	0.7511(1)	1.0043(2)	0.5037(2)	1	0.041(1)
Cl(0A)	0.7539(2)	3/4	0.2503(2)	1	0.042(1)
Cl(0B)	0.5873(2)	3/4	0.5833(2)	1	0.050(1)

Table C.1: Atomic coordinates and isotropic displacement parameters for $Cs_3Bi_2Cl_9$. Values in parentheses represent one standard deviation.

Label	x	y	z	Occupancy	U_{iso} (Å^2)
Bi	2/3	1/3	0.8161(1)	1	0.023(1)
Cs(1)	1/3	2/3	0.6661(2)	1	0.058(1)
Cs(2)	0	0	0	1	0.071(1)
Cl(1)	0.3327(3)	0.1664(2)	0.6626(2)	0.861(5)	0.064(1)
I(1)	0.3327(3)	0.1664(2)	0.6626(2)	0.139(5)	0.064(1)
Cl(2)	1/2	1/2	0	1	0.071(2)

Table C.2: Atomic coordinates and isotropic displacement parameters for $Cs_3Bi_2Cl_{8.16}I_{0.84}$. Values in parentheses represent one standard deviation.

Label	U_{11} (Å^2)	U_{22} (Å^2)	U_{33} (Å^2)	U_{12} (Å^2)	U_{13} (Å^2)	U_{23} (Å^2)
Bi(01)	0.019(1)	0.019(1)	0.015(1)	0	0	0
Bi(02)	0.018(1)	0.021(1)	0.018(1)	0	0	0
Cs(03)	0.045(1)	0.044(1)	0.032(1)	0	0.001(1)	0
Cs(04)	0.038(1)	0.046(1)	0.043(1)	0	0.008(1)	0
Cs(05)	0.045(1)	0.040(1)	0.046(1)	0	–0.001(1)	0
Cl(06)	0.047(1)	0.039(1)	0.044(1)	–0.017(1)	–0.009(1)	–0.008(1)
Cl(07)	0.052(2)	0.046(1)	0.060(2)	–0.021(1)	–0.013(2)	–0.015(1)
Cl(08)	0.046(2)	0.058(2)	32(2)	0	0.020(2)	0
Cl(09)	0.040(1)	0.036(1)	0.046(1)	–0.011(1)	–0.007(1)	–0.012(1)
Cl(0A)	0.040(2)	0.057(2)	0.027(2)	0	0.017(1)	0
Cl(0B)	0.050(2)	0.066(2)	0.034(2)	0	0.023(2)	0

Table C.3: Anisotropic displacement parameters for $Cs_3Bi_2Cl_9$ with estimated standard deviations in parentheses.

Label	U_{11} (Å^2)	U_{22} (Å^2)	U_{33} (Å^2)	U_{12} (Å^2)	U_{13} (Å^2)	U_{23} (Å^2)
Bi	0.025(1)	0.025(1)	0.019(1)	0.013(1)	0	0
Cs(1)	0.064(1)	0.064(1)	0.046(1)	0.032(1)	0	0
Cs(2)	0.057(1)	0.057(1)	0.099(2)	0.028(1)	0	0
Cl(1)	0.070(2)	0.069(1)	0.053(1)	0.035(1)	-0.012(1)	-0.006(1)
I(1)	0.070(2)	0.069(1)	0.053(1)	0.035(1)	-0.012(1)	-0.006(1)
Cl(2)	0.084(2)	0.084(2)	0.069(2)	0.060(2)	0.018(1)	-0.018(1)

Table C.4: Anisotropic displacement parameters for $Cs_3Bi_2Cl_{8.16}I_{0.84}$ with estimated standard deviations in parentheses.

Label	Distance (Å)
Bi(01)-Cl(07)	2.8180(17)
Bi(01)-Cl(07)	2.8181(17)
Bi(01)-Cl(09)	2.5748(17)
Bi(01)-Cl(09)	2.5748(17)
Bi(01)-Cl(0A)	2.572(2)
Bi(01)-Cl(0B)	2.823(3)
Bi(02)-Cl(06)	2.5475(16)
Bi(02)-Cl(06)	2.5475(16)
Bi(02)-Cl(07)	2.8487(17)
Bi(02)-Cl(07)	2.8487(17)
Bi(02)-Cl(08)	2.532(2)
Bi(02)-Cl(0B)	2.870(3)

Table C.5: Selected bond lengths for $Cs_3Bi_2Cl_9$.

Label	Distance (Å)
Bi(01)-Cl(1)	2.6772(19)
Bi(01)-Cl(2)	2.8428(2)

Table C.6: Selected bond lengths for $Cs_3Bi_2Cl_{8.16}I_{0.84}$.

Appendix D

Additional characterization details for A_2WCl_6 compounds

Empirical formula	$(CH_3NH_3)_2WCl_6$	Cs_2WCl_6	Rb_2WCl_6	$Cs_2WO_{1.08}Cl_{4.92}$
Formula weight (g/mol)	460.70	662.38	567.50	641.37
Temperature (K)	298	300	300	101
Crystal system	Trigonal	Cubic	Cubic	Cubic
Space group	$R\bar{3}m$	$Fm\bar{3}m$	$Fm\bar{3}m$	$Fm\bar{3}m$
Lattice parameters (Å)	$a = b =$ 7.1125(14) $c =$21.975(6)	$a = b = c =$ 10.326451(55)	$a = b = c =$ 10.023918(349)	$a = b = c =$ 10.23(2)
Unit cell angles (°)	$\alpha = \beta = 90$ $\gamma = 120$	$\alpha = \beta = \gamma =$ 90	$\alpha = \beta = \gamma = 90$	$\alpha = \beta = \gamma =$ 90
Volume (Å^3)	962.7(4)	1101.167(17)	1007.193(105)	1072(6)

Table D.1: Unit cell details for MA_2WCl_6, Cs_2WCl_6, Rb_2WCl_6, and $Cs_2WO_{1.08}Cl_{4.92}$.

Label	*x*	*y*	*z*	Occupancy	U_{iso} (Å^2)
W(1)	1/3	2/3	2/3	1	0.038
Cl(1)	0.17509	0.35020	0.60467	1	0.047
C(1)	2/3	1/3	0.54010	1	0.064
H(1A)	0.78024	0.30937	0.52550	1/6	0.096
H(1B)	0.69063	0.47087	0.52550	1/6	0.096
H(1C)	0.52913	0.21976	0.52550	1/6	0.096
N(1)	2/3	1/3	0.60630	1	0.051
H(1D)	0.78921	0.34308	0.61976	1/6	0.077
H(1E)	0.55387	0.21079	0.61976	1/6	0.077
H(1F)	0.65692	0.44613	0.61976	1/6	0.077

Table D.2: Atomic coordinates and isotropic displacement parameters for MA_2WCl_6.

Label	*x*	*y*	*z*	Occupancy	U_{iso} (Å^2)
W(1)	0	0	0	1	0.024
Cs(1)	1/4	1/4	1/4	1	0.039
Cl(1)	–0.23026	0	0	1	0.037

Table D.3: Atomic coordinates and isotropic displacement parameters for Cs_2WCl_6.

Label	x	y	z	Occupancy	U_{iso} (Å^2)
W(1)	0	0	0	1	0.025
Rb(1)	1/4	1/4	1/4	1	0.040
Cl(1)	–0.2374	0	0	1	0.042

Table D.4: Atomic coordinates and isotropic displacement parameters for Rb_2WCl_6.

Label	x	y	z	Occupancy	U_{iso} (Å^2)
W(1)	1/2	1/2	1/2	1	0.051
Cs(1)	1/4	1/4	1/4	1	0.033
Cl(1)	0.2684	1/2	1/2	0.82	0.032
O(1)	0.314	1/2	1/2	0.18	0.032

Table D.5: Atomic coordinates and isotropic displacement parameters for $Cs_2WO_{1.08}Cl_{4.92}$.

Formula	$(CH_3NH_3)_2WCl_6$	$Cs_2WO_{1.08}Cl_{4.92}$
Absorption coeff. (mm^{-1})	10.202	18.648
θ range for data collection (°)	2.78 to 24.712	3.448 to 30.370
Reflections collected	372	1803
Independent reflections	236	115
Completeness (%)	100	101.8
Refinement method	Full-matrix least-squares on F^2	Full-matrix least-squares on F^2
Data/restraints/parameters	236/0/17	115/0/8
Goodness-of-fit	1.014	1.133
Final R indices [I>2sigma(I)]	R=0.0233, wR=0.0478	R= 0.0254, wR= 0.0495
R indices (all data)	R=0.0258, wR=0.0482	R= 0.0300, wR= 0.0532
Largest diff. peak and hole	0.458 and -0.572	1.680 and -1.559

Table D.6: Single-crystal XRD details for $(CH_3NH_3)_2WCl_6$ and $Cs_2WO_{1.08}Cl_{4.92}$.

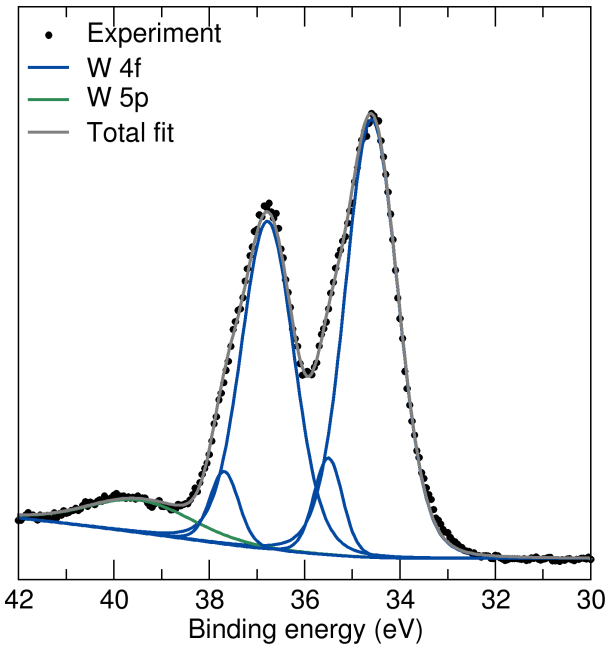

Figure D.1: Tungsten $4f$ high-resolution region of the XPS spectrum for MA_2WCl_6.

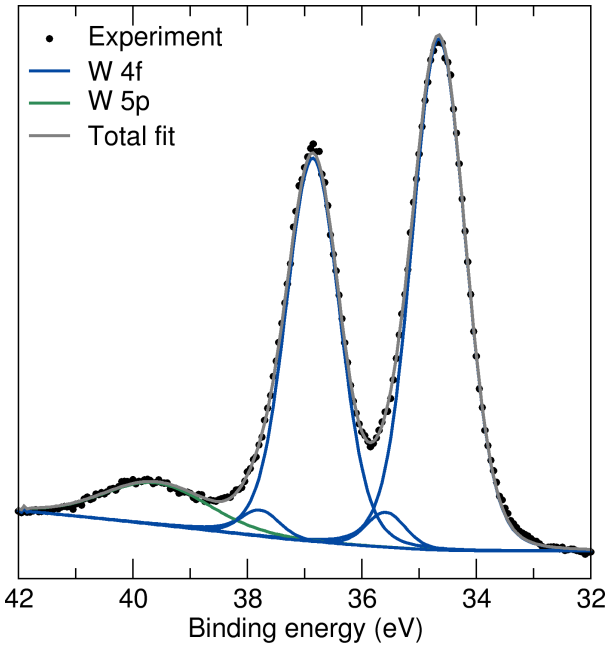

Figure D.2: Tungsten $4f$ high-resolution region of the XPS spectrum for Rb_2WCl_6.

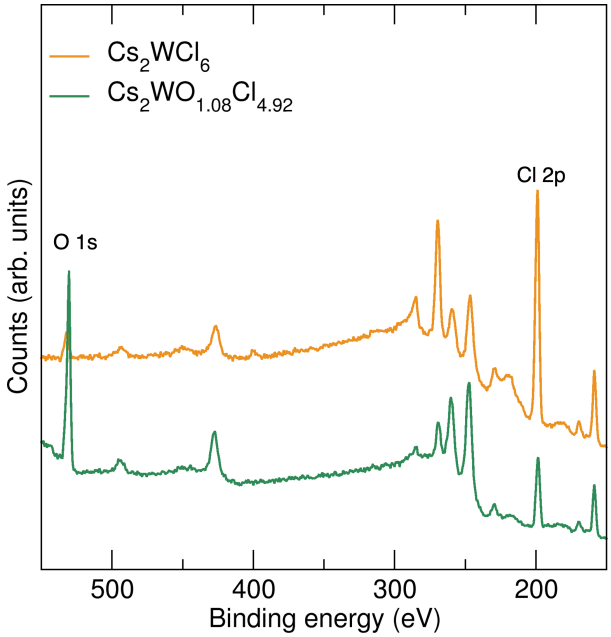

Figure D.3: XPS survey scans for Cs_2WCl_6 and $Cs_2WO_{1.08}Cl_{4.92}$ showing the O $1s$ and Cl $2p$ peaks.

Appendix E

Crystallographic details for $Cs_2MO_xX_{6-x}$ compounds

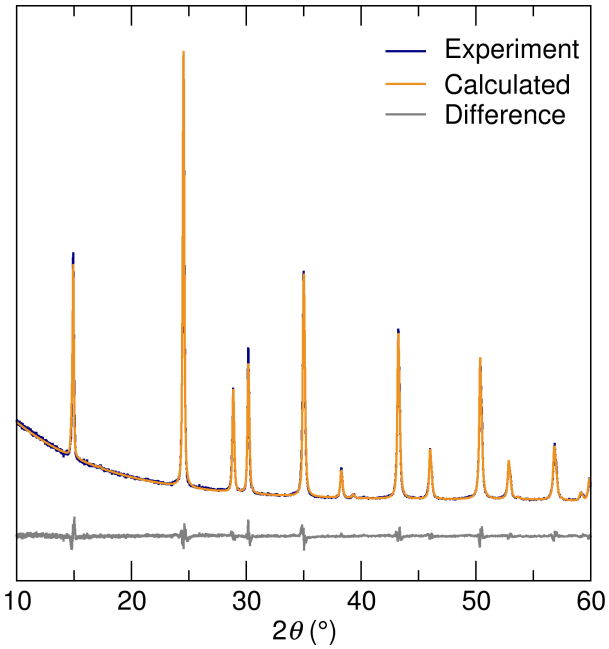

Figure E.1: Powder X-ray diffraction pattern and Pawley refinement for $Cs_2WO_{1.32}Cl_{4.68}$ with a calculated lattice parameter of 10.232 Å.

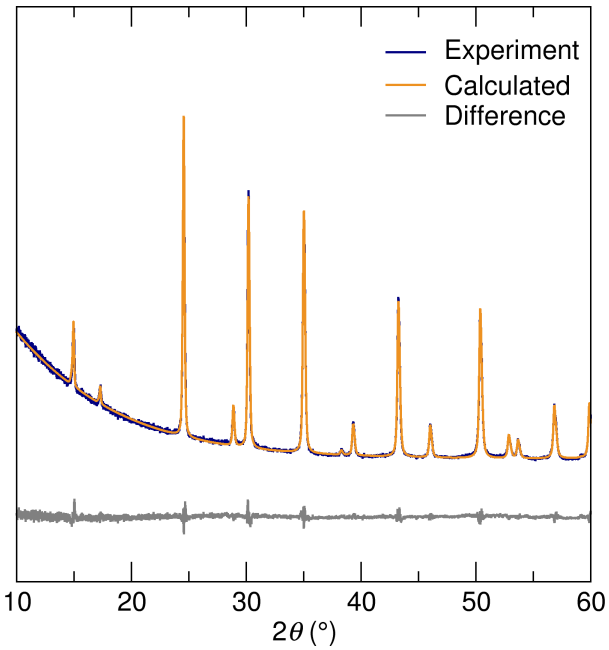

Figure E.2: Powder X-ray diffraction pattern and Pawley refinement for $Cs_2MoO_{1.20}Cl_{4.80}$ with a calculated lattice parameter of 10.235 Å.

Empirical formula	$Cs_2WO_{1.32}Cl_{4.68}$	$Cs_2MoO_{1.20}Cl_{4.80}$	$Cs_2MoO_{1.602}Br_{4.398}$
Formula weight (g/mol)	636.68	551.13	543.31
Temperature (K)	298	297	298
Crystal system	Cubic	Cubic	Cubic
Space group	$Fm\bar{3}m$	$Fm\bar{3}m$	$Fm\bar{3}m$
Lattice parameters (Å)	$a = b = c =$ 10.208(3)	$a = b = c =$ 10.216(5)	$a = b = c =$ 10.613(7)
Unit cell angles (°)	$\alpha = \beta = \gamma = 90$	$\alpha = \beta = \gamma = 90$	$\alpha = \beta = \gamma = 90$
Volume (Å^3)	1063.9(10)	1066.2(16)	1195(2)
Absorption coeff. (mm^{-1})	18.708	9.113	21.754
θ range for data collection (°)	3.457 to 29.492	3.454 to 29.468	3.325 to 29.704
Reflections collected	665	660	751
Independent reflections	106	106	120
Completeness (%)	102.9	100	99.2
Refinement method	Full-matrix least-squares on F^2	Full-matrix least-squares on F^2	Full-matrix least-squares on F^2
Data/restraints/parameters	106/9/0	106/9/0	120/9/0
Goodness-of-fit	1.117	1.176	1.112
Final R indices [I>2sigma(I)]	R= 0.0240, wR= 0.0456	R= 0.0220, wR= 0.0459	R= 0.0313, wR= 0.0599
R indices (all data)	R= 0.0271, wR= 0.0464	R= 0.0238, wR= 0.0470	R= 0.0393, wR= 0.0629
Largest diff. peak and hole	1.297 and -1.252	1.221 and -0.887	1.455 and -1.243

Table E.1: Unit cell details for $Cs_2WO_{1.32}Cl_{4.68}$, $Cs_2MoO_{1.20}Cl_{4.80}$, and $Cs_2MoO_{1.602}Br_{4.398}$.

Label	x	y	z	Occupancy	U_{iso} (Å^2)
W(1)	1/2	1/2	1/2	1	0.051
Cs(1)	3/4	3/4	3/4	1	0.033
Cl(1)	1/2	0.73210	1/2	0.780	0.031
O(1)	1/2	0.69700	1/2	0.220	0.031

Table E.2: Atomic coordinates and isotropic displacement parameters for $Cs_2WO_{1.32}Cl_{4.68}$.

Label	x	y	z	Occupancy	U_{iso} (Å^2)
Cs(1)	1/4	1/4	1/4	1	0.038
Mo(1)	1/2	1/2	1/2	1	0.063
Cl(1)	0.26830	1/2	1/2	0.800	0.036
O(1)	0.30700	1/2	1/2	0.200	0.036

Table E.3: Atomic coordinates and isotropic displacement parameters for $Cs_2MoO_{1.20}Cl_{4.80}$.

Label	x	y	z	Occupancy	U_{iso} (Å^2)
Cs(1)	1/4	1/4	1/4	1	0.046
Mo(1)	1/2	1/2	1/2	1	0.074
Br(1)	1/2	1/2	0.26297	0.733	0.038
O(1)	1/2	1/2	0.30600	0.267	0.038

Table E.4: Atomic coordinates and isotropic displacement parameters for $Cs_2MoO_{1.602}Br_{4.398}$.

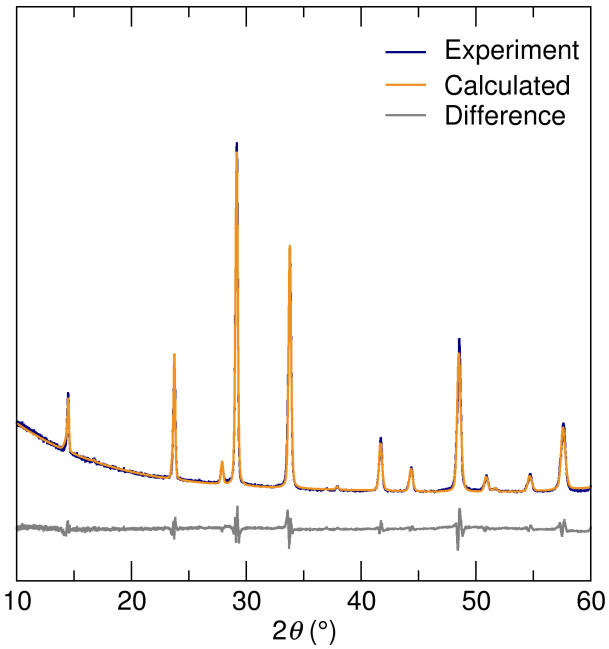

Figure E.3: Powder X-ray diffraction pattern and Pawley refinement for $Cs_2MoO_{1.602}Br_{4.398}$ with a calculated lattice parameter of 10.624 Å.

Bibliography

[1] V. M. Goldschmidt. Die Gesetze der Krystallochemie. *Naturwiss.* **14** (1926) 477–485. doi:10.1007/BF01507527

[2] D. Weber. $CH_3NH_3PbX_3$, ein Pb(II)-System mit kubischer Perowskitstruktur / $CH_3NH_3PbX_3$, a Pb(II)-System with Cubic Perovskite Structure. *Z. Naturforsch. B* **33** (1978) 1443–1445. doi:10.1515/znb-1978-1214

[3] R. E. Wasylishen, O. Knop, and J. B. Macdonald. Cation rotation in methylammonium lead halides. *Solid State Commun.* **56** (1985) 581–582. doi:10.1016/0038-1098(85)90959-7

[4] K. Yamada, H. Kawaguchi, T. Matsui, T. Okuda, and S. Ichiba. Structural Phase Transition and Electrical Conductivity of the Perovskite $CH_3NH_3Sn_{1-x}Pb_xBr_3$ and $CsSnBr_3$. *BCSJ* **63** (1990) 2521–2525. doi:10.1246/bcsj.63.2521

[5] A. Kojima, K. Teshima, Y. Shirai, and T. Miyasaka. Organometal Halide Perovskites as Visible-Light Sensitizers for Photovoltaic Cells. *J. Am. Chem. Soc.* **131** (2009) 6050–6051. doi:10.1021/ja809598r

[6] National Renewable Energy Laboratory. Best Research-Cell Efficiency Chart. https://www.nrel.gov/pv/cell-efficiency.html.

[7] W. Li, Z. Wang, F. Deschler, S. Gao, R. H. Friend, and A. K. Cheetham. Chemically diverse and multifunctional hybrid organic–inorganic perovskites. *Nat. Rev. Mater.* **2** (2017) 1–18. doi:10.1038/natrevmats.2016.99

[8] P. Vishnoi, J. Zuo, T. A. Strom, G. Wu, S. D. Wilson, R. Seshadri, and A. K. Cheetham. Structural Diversity and Magnetic Properties of Hybrid Ruthenium Halide Perovksites and Related Compounds. *Angew. Chem.* **59** (2020) 8974–8981. doi:10.1002/anie.202003095

[9] R. D. Shannon and C. T. Prewitt. Effective ionic radii in oxides and fluorides. *Acta Cryst. B* **25** (1969) 925–946. doi:10.1107/S0567740869003220

[10] R. D. Shannon. Revised effective ionic radii and systematic studies of interatomic distances in halides and chalcogenides. *Acta Cryst. A* **32** (1976) 751–767. doi:10.1107/S0567739476001551

[11] G. Kieslich, S. Sun, and A. K. Cheetham. An extended Tolerance Factor approach for organic–inorganic perovskites. *Chem. Sci.* **6** (2015) 3430–3433. doi:10.1039/C5SC00961H

[12] G. Kieslich, S. Sun, and A. K. Cheetham. Solid-state principles applied to organic–inorganic perovskites: new tricks for an old dog. *Chem. Sci.* **5** (2014) 4712–4715. doi:10.1039/C4SC02211D

[13] H. A. Evans, Y. Wu, R. Seshadri, and A. K. Cheetham. Perovskite-related ReO_3-type structures. *Nat. Rev. Mater.* **5** (2020) 196–213. doi:10.1038/s41578-019-0160-x

[14] N. R. Wolf, B. A. Connor, A. H. Slavney, and H. I. Karunadasa. Doubling the Stakes: The Promise of Halide Double Perovskites. *Angew. Chem. Int. Ed.* **60** (2021) 16264–16278. doi:10.1002/anie.202016185

[15] P. Vishnoi, R. Seshadri, and A. K. Cheetham. Why are Double Perovskite Iodides so Rare? *J. Phys. Chem. C* **125** (2021) 11756–11764. doi:10.1021/acs.jpcc.1c02870

[16] G. Kent, E. Morgan, K. R. Albanese, A. Kallistova, A. Brumberg, L. Kautzsch, G. Wu, P. Vishnoi, R. Seshadri, and A. K. Cheetham. Elusive Double Perovskite Iodides: Structural, Optical, and Magnetic Properties. *Angew. Chem. Int. Ed.* (2023) e202306000. doi:10.1002/anie.202306000

[17] L. A. Muscarella and E. M. Hutter. Halide Double-Perovskite Semiconductors beyond Photovoltaics. *ACS Energy Lett.* **7** (2022) 2128–2135. doi:10.1021/acsenergylett.2c00811

[18] A. E. Maughan, A. M. Ganose, D. O. Scanlon, and J. R. Neilson. Perspectives and Design Principles of Vacancy-Ordered Double Perovskite Halide Semiconductors. *Chem. Mater.* **31** (2019) 1184–1195. doi:10.1021/acs.chemmater.8b05036

[19] W. Rahim, A. Cheng, C. Lyu, T. Shi, Z. Wang, D. O. Scanlon, and R. G. Palgrave. Geometric Analysis and Formability of the Cubic A_2BX_6 Vacancy-Ordered Double Perovskite Structure. *Chem. Mater.* **32** (2020) 9573–9583. doi:10.1021/acs.chemmater.0c02806

[20] Z. Liu, X. Qin, Q. Chen, Q. Chen, Y. Jing, Z. Zhou, Y. S. Zhao, J. Chen, and X. Liu. Highly Stable Lead-Free Perovskite Single Crystals with NIR Emission Beyond 1100 nm. *Adv. Opt. Mater.* **10** (2022) 2201254. doi:10.1002/adom.202201254

[21] T. Zhang, D. Hara, and S. Murakami. Unique Surface-State Connection Between Weyl and Nodal Ring Fermions in Ferromagnetic Material Cs_2MoCl_6. *Phys. Rev. Research* **3** (2021) L042037. doi:10.1103/PhysRevResearch.3.L042037

[22] J. G. Bednorz and K. A. Müller. Possible high Tc superconductivity in the Ba-La-Cu-O system. *Z. Phys. B - Condens. Matter* **64** (1986) 189–193. doi:10.1007/BF01303701

[23] R. Mokhlisse, M. Couzi, N. B. Chanh, Y. Haget, C. Hauw, and A. Meresse. Raman scattering and X-ray diffraction study of structural phase transitions in the perovskite-type layer compound $(C_3H_7NH_3)_2CdCl_4$. *J. Phys. Chem. Solids* **46** (1985) 187–195. doi:10.1016/0022-3697(85)90033-2

[24] T. Ishihara, J. Takahashi, and T. Goto. Exciton state in two-dimensional perovskite semiconductor $(C_{10}H_{21}NH_3)_2PbI_4$. *Solid State Commun.* **69** (1989) 933–936. doi:10.1016/0038-1098(89)90935-6

[25] T. Nakajima, H. Yamauchi, T. Goto, M. Yoshizawa, T. Suzuki, and T. Fujimura. Magnetic and elastic properties of $(CH_3NH_3)_2FeCl_4$ and $(C_2H_5NH_3)_2FeCl_4$. *J. Magn. Magn. Mater.* **31-34** (1983) 1189–1190. doi:10.1016/0304-8853(83)90857-0

[26] D. B. Mitzi, C. A. Feild, W. T. A. Harrison, and A. M. Guloy. Conducting tin halides with a layered organic-based perovskite structure. *Nature* **369** (1994) 467–469. doi:10.1038/369467a0

[27] D. B. Mitzi, S. Wang, C. A. Feild, C. A. Chess, and A. M. Guloy. Conducting Layered Organic-inorganic Halides Containing $\langle 110 \rangle$ -Oriented Perovskite Sheets. *Science* **267** (1995) 1473–1476. doi:10.1126/science.267.5203.1473

[28] L. Mao, C. C. Stoumpos, and M. G. Kanatzidis. Two-Dimensional Hybrid Halide Perovskites: Principles and Promises. *J. Am. Chem. Soc.* **141** (2019) 1171–1190. doi:10.1021/jacs.8b10851

[29] H. A. Evans, L. Mao, R. Seshadri, and A. K. Cheetham. Layered Double Perovskites. *Annu. Rev. Mater. Res.* **51** (2021) 351–380. doi:10.1146/annurev-matsci-092320-102133

[30] R. M. Kennard, C. J. Dahlman, E. E. Morgan, J. Chung, B. L. Cotts, J. R. A. Kincaid, R. A. DeCrescent, K. H. Stone, S. Panuganti, Y. Mohtashami, L. Mao, R. D. Schaller, A. Salleo, M. G. Kanatzidis, J. A. Schuller, R. Seshadri, and M. L. Chabinyc. Enhancing and Extinguishing the Different Emission Features of 2D $(EA_{1-x}FA_x)_4Pb_3Br_{10}$ Perovskite Films. *Adv. Opt. Mater.* **10** (2022) 2200547. doi:10.1002/adom.202200547

[31] L. Mao, E. E. Morgan, A. Li, R. M. Kennard, M. J. Hong, Y. Liu, C. J. Dahlman, J. G. Labram, M. L. Chabinyc, and R. Seshadri. Layered Hybrid Lead Iodide Perovskites with Short Interlayer Distances. *ACS Energy Lett.* **7** (2022) 2801–2806. doi:10.1021/acsenergylett.2c01321

[32] C. Chen, E. E. Morgan, Y. Liu, J. Chen, R. Seshadri, and L. Mao. "Breathing" organic cation to stabilize multiple structures in low-dimensional Ge-, Sn-, and Pb-based hybrid iodide perovskites. *Inorg. Chem. Front.* **9** (2022) 4892–4898. doi:10.1039/D2QI01247B

[33] G. S. Pawley. Unit-Cell Refinement from Powder Diffraction Scans. *J. Appl. Cryst.* **14** (1981) 357–361. doi:10.1107/S0021889881009618

[34] A. Le Bail, H. Duroy, and J. L. Fourquet. Ab-Initio Structure Determination of $LiSbWO_6$ by X-ray Powder Diffraction. *Mater. Res. Bull.* **23** (1988) 447–452. doi:10.1016/0025-5408(88)90019-0

[35] H. M. Rietveld. Line profiles of neutron powder-diffraction peaks for structure refinement. *Acta. Cryst.* **22** (1967) 151–152. doi:10.1107/S0365110X67000234

[36] A. A. Coelho. TOPAS and TOPAS-Academic: An Optimization Program Integrating Computer Algebra and Crystallographic Objects Written in C++. *J. Appl. Crystallogr.* **51** (2018) 210–218. doi:10.1107/S1600576718000183

[37] L. B. McCusker, R. B. Von Dreele, D. E. Cox, D. Louër, and P. Scardi. Rietveld refinement guidelines. *J. Appl. Cryst.* **32** (1999) 36–50. doi:10.1107/S0021889898009856

[38] B. H. Toby. R factors in Rietveld analysis: How good is good enough? *Powder Diff.* **21** (2006) 67–70. doi:10.1154/1.2179804

[39] B. H. Toby and R. B. Von Dreele. GSAS-II: The Genesis of a Modern Open-Source All Purpose Crystallography Software Package. *J Appl Cryst* **46** (2013). doi:10.1107/S0021889813003531

[40] A. K. Cheetham and A. P. Wilkinson. Synchrotron X-ray and Neutron Diffraction Studies in Solid-State Chemistry. *Angew. Chem. Int. Ed.* **31** (1992) 1557–1570. doi:10.1002/anie.199215571

[41] M. I. Aroyo, J. M. Perez-Mato, C. Capillas, E. Kroumova, S. Ivantchev, G. Madariaga, A. Kirov, and H. Wondratschek. Bilbao Crystallographic Server: I. Databases and crystallographic computing programs. *Z. Kristallogr.* **221** (2006) 15–27. doi:10.1524/zkri.2006.221.1.15

[42] M. I. Aroyo, A. Kirov, C. Capillas, J. M. Perez-Mato, and H. Wondratschek. Bilbao Crystallographic Server. II. Representations of Crystallographic Point Groups and Space Groups. *Acta. Cryst. A* **62** (2006) 115–128. doi:10.1107/S0108767305040286

[43] E. Kroumova, M. I. Aroyo, J. M. Perez-Mato, A. Kirov, C. Capillas, S. Ivantchev, and H. Wondratschek. Bilbao Crystallographic Server: Useful Databases and Tools for Phase-Transition Studies. *Phase Trans.* **76** (2003) 155–170.

[44] P. Kubelka. Ein Beitrag zur Optik der Farbanstriche. *Z. Phys.* **12** (1931) 593–601.

[45] D. C. Apperley, R. K. Harris, and P. Hodgkinson. *Solid State NMR: Basic Principles & Practice*. Momentum Press (2012).

[46] H. Sun, S. Dwaraknath, H. Ling, X. Qu, P. Huck, K. A. Persson, and S. E. Hayes. Enabling materials informatics for ^{29}Si solid-state NMR of crystalline materials. *npj Comput. Mater.* **6** (2020) 1–7. doi:10.1038/s41524-020-0328-3

[47] C. Bonhomme, C. Gervais, F. Babonneau, C. Coelho, F. Pourpoint, T. Azais, S. E. Ashbrook, J. M. Griffin, J. R. Yates, F. Mauri, and C. J. Pickard. First-Principles Calculation of NMR Parameters Using the Gauge Including Projector Augmented Wave Method: A Chemist's Point of View. *Chem. Rev.* **112** (2012) 5733.

[48] M. McElfresh. *Fundamentals of Magnetism and Magnetic Measurements*. Quantum Design (1994).

[49] S. Mugiraneza and A. M. Hallas. Tutorial: a beginner's guide to interpreting magnetic susceptibility data with the Curie-Weiss law. *Commun. Phys.* **5** (2022) 1–12. doi:10.1038/s42005-022-00853-y

[50] M. Kotani. On the Magnetic Moment of Complex Ions. (I). *J. Phys. Soc. Jpn.* **4** (1949) 293–297. doi:10.1143/JPSJ.4.293

[51] G. Kresse and J. Hafner. *Ab Initio* Molecular-Dynamics Simulation of the Liquid-Metal–Amorphous-Semiconductor Transition in Germanium. *Phys. Rev. B* **49** (1994) 14251–14269. doi:10.1103/PhysRevB.49.14251

[52] G. Kresse and J. Furthmüller. Efficiency of Ab-Initio Total Energy Calculations for Metals and Semiconductors using a Plane-Wave Basis Set. *Comput. Mater. Sci.* **6** (1996) 15–50. doi:10.1016/0927-0256(96)00008-0

[53] G. Kresse and J. Furthmüller. Efficient Iterative Schemes for *Ab Initio* Total-Energy Calculations Using A Plane-Wave Basis Set. *Phys. Rev. B* **54** (1996) 11169–11186. doi:10.1103/PhysRevB.54.11169

[54] S. J. Clark, M. D. Segall, C. J. Pickard, P. J. Hasnip, M. I. J. Probert, K. Refson, and M. C. Payne. First Principles Methods Using CASTEP. *Z. Kristallogr.* **220** (2005). doi:10.1524/zkri.220.5.567.65075

[55] P. Hohenberg and W. Kohn. Inhomogeneous Electron Gas. *Phys. Rev.* **136** (1964) B864–B871.

[56] W. Kohn and L. J. Sham. Self-Consistent Equations Including Exchange and Correlation Effects. *Phys. Rev.* **140** (1965) A1133–A1138.

[57] T. Charpentier. The PAW/GIPAW Approach for Computing NMR Parameters: A New Dimension Added to NMR Study of Solids. *Solid State Nuc. Magn. Res.* **40** (2011) 1–20. doi:10.1016/j.ssnmr.2011.04.006

[58] J. P. Perdew, K. Burke, and M. Ernzerhof. Generalized Gradient Approximation Made Simple. *Phys. Rev. Lett.* **77** (1996) 3865–3868. doi:10.1103/PhysRevLett.77.3865

[59] J. C. Phillips and L. Kleinman. New Method for Calculating Wave Functions in Crystals and Molecules. *Phys. Rev.* **116** (1959) 287–294. doi:10.1103/PhysRev.116.287

[60] E. Antončík. Approximate formulation of the orthogonalized plane-wave method. *J. Phys. Chem. Sol.* **10** (1959) 314–320. doi:10.1016/0022-3697(59)90007-1

[61] I. V. Abarenkov and V. Heine. The model potential for positive ions. *Phil. Mag.* **12** (1965) 529–537. doi:10.1080/14786436508218898

[62] D. R. Hamann, M. Schlüter, and C. Chiang. Norm-Conserving Pseudopotentials. *Phys. Rev. Lett.* **43** (1979) 1494–1497. doi:10.1103/PhysRevLett.43.1494

[63] L. Kleinman and D. M. Bylander. Efficacious Form for Model Pseudopotentials. *Phys. Rev. Lett.* **48** (1982) 1425–1428. doi:10.1103/PhysRevLett.48.1425

[64] D. Vanderbilt. Soft Self-Consistent Pseudopotentials in a Generalized Eigenvalue Formalism. *Phys. Rev. B* **41** (1990) 7892–7895. doi:10.1103/PhysRevB.41.7892

[65] C. G. Van de Walle and P. E. Blöchl. First-Principles Calculations of Hyperfine Parameters. *Phys. Rev. B* **47** (1993) 4244–4255. doi:10.1103/PhysRevB.47.4244

[66] P. E. Blöchl. Projector Augmented-Wave Method. *Phys. Rev. B* **50** (1994) 17953–17979. doi:10.1103/PhysRevB.50.17953

[67] E. E. Morgan, L. Mao, S. M. L. Teicher, G. Wu, and R. Seshadri. Tunable Perovskite-Derived Bismuth Halides: $Cs_3Bi_2(Cl_{1-x}I_x)_9$. *Inorg. Chem.* **59** (2020) 3387–3393. doi:10.1021/acs.inorgchem.9b03415

[68] M. K. Y. Chan and G. Ceder. Efficient Band Gap Prediction for Solids. *Phys. Rev. Lett.* **105** (2010) 196403. doi:10.1103/PhysRevLett.105.196403

[69] S. Wang, E. E. Morgan, P. Vishnoi, L. Mao, S. M. L. Teicher, G. Wu, Q. Liu, A. K. Cheetham, and R. Seshadri. Tunable Luminescence in Hybrid Cu(I) and Ag(I) Iodides. *Inorg. Chem.* **59** (2020) 15487–15494. doi:10.1021/acs.inorgchem.0c02517

[70] R. Dronskowski and P. E. Bloechl. Crystal Orbital Hamilton populations (COHP): Energy-Resolved Visualization of Chemical Bonding in Solids Based on Density-Functional Calculations. *J. Phys. Chem.* **97** (1993) 8617. doi:10.1021/j100135a014

[71] V. L. Deringer, A. L. Tchougréeff, and R. Dronskowski. Crystal Orbital Hamilton Population (COHP) Analysis As Projected from Plane-Wave Basis Sets. *J. Phys. Chem. A* **115** (2011) 5461. doi:10.1021/jp202489s

[72] S. Maintz, V. L. Deringer, A. L. Tchougréeff, and R. Dronskowski. Analytic Projection from Plane-Wave and PAW Wavefunctions and Application to Chemical-Bonding Analysis in Solids. *J. Comput. Chem.* **34** (2013) 2557. doi:10.1002/jcc.23424

[73] S. Maintz, V. L. Deringer, A. L. Tchougréeff, and R. Dronskowski. LOBSTER: A Tool to Extract Chemical Bonding from Plane-Wave Based DFT. *J. Comput. Chem.* **37** (2016) 1030. doi:10.1002/jcc.24300

[74] C. Pickard and F. Mauri. All-Electron Magnetic Response with Pseudopotentials: NMR Chemical Shifts. *Phys. Rev. B* **63** (2001) 245101.

[75] S. Rossano, F. Mauri, C. J. Pickard, and I. Farnan. First-Principles Calculation of ^{17}O and ^{25}Mg NMR Shieldings in MgO at Finite Temperature: Rovibrational Effect in Solids. *J. Phys. Chem. B* **109** (2005) 7245–7250. doi:10.1021/jp044251w

[76] J. Schmidt and D. Sebastiani. Anomalous temperature dependence of nuclear quadrupole interactions in strongly hydrogen-bonded systems from first principles. *J. Chem. Phys.* **123** (2005) 074501. doi:10.1063/1.2000241

[77] B. Monserrat, R. J. Needs, and C. J. Pickard. Temperature Effects in First-Principles Solid State Calculations of the Chemical Shielding Tensor Made Simple. *J. Chem. Phys.* **141** (2014) 134113. doi:10.1063/1.4897261

[78] M. Gajdoš, K. Hummer, G. Kresse, J. Furthmüller, and F. Bechstedt. Linear Optical Properties in the Projector-Augmented Wave Methodology. *Phys. Rev. B* **73** (2006) 045112. doi:10.1103/PhysRevB.73.045112

[79] S. Baroni and R. Resta. Ab initio Calculation of the Macroscopic Dielectric Constant in Silicon. *Phys. Rev. B* **33** (1986) 7017–7021. doi:10.1103/PhysRevB.33.7017

[80] A. J. Morris and B. Monserrat. Optical absorption driven by dynamical symmetry breaking in indium oxide. *Phys. Rev. B* **98** (2018) 161203. doi:10.1103/PhysRevB.98.161203

[81] B. Monserrat, C. E. Dreyer, and K. M. Rabe. Phonon-assisted optical absorption in $BaSnO_3$ from first principles. *Phys. Rev. B* **97** (2018) 104310. doi:10.1103/PhysRevB.97.104310

[82] H. J. Snaith. Present Status and Future Prospects of Perovskite Photovoltaics. *Nat. Mater.* **17** (2018) 372–376. doi:10.1038/s41563-018-0071-z

[83] B. Saparov and D. B. Mitzi. Organic-Inorganic Perovskites: Structural Versatility for Functional Materials Design. *Chem. Rev.* **116** (2016) 4558–4596. doi:10.1021/acs.chemrev.5b00715

[84] H. Wang, H. Bian, Z. Jin, H. Zhang, L. Liang, J. Wen, Q. Wang, L. Ding, and S. F. Liu. Cesium Lead Mixed-Halide Perovskites for Low Energy Loss Solar Cells with Efficiency Beyond 17%. *Chem. Mater.* (2019). doi:10.1021/acs.chemmater.9b02248

[85] D. Fabini. Quantifying the Potential for Lead Pollution from Halide Perovskite Photovoltaics. *J. Phys. Chem. Lett.* **6** (2015) 3546–3548. doi:10.1021/acs.jpclett.5b01747

[86] A. Babayigit, A. Ethirajan, M. Muller, and B. Conings. Toxicity of Organometal Halide Perovskite Solar Cells. *Nat. Mater.* **15** (2016) 247–251. doi:10.1038/nmat4572

[87] Z. Shi, J. Guo, Y. Chen, Q. Li, Y. Pan, H. Zhang, Y. Xia, and W. Huang. Lead-Free Organic–Inorganic Hybrid Perovskites for Photovoltaic Applications: Recent Advances and Perspectives. *Adv. Mater.* **29** (2017) 1605005. doi:10.1002/adma.201605005

[88] B.-W. Park, B. Philippe, X. Zhang, H. Rensmo, G. Boschloo, and E. M. Johansson. Bismuth Based Hybrid Perovskites $A_3Bi_2I_9$ (*A*: Methylammonium or Cesium) for Solar Cell Application. *Adv. Mater.* **27** (2015) 6806–6813. doi:10.1002/adma.201501978

[89] M. Abulikemu, S. Ould-Chikh, X. Miao, E. Alarousu, B. Murali, G. O. N. Ndjawa, J. Barbé, A. El Labban, A. Amassian, and S. Del Gobbo. Optoelectronic and Photovoltaic Properties of the Air-Stable Organohalide Semiconductor $(CH_3NH_3)_3Bi_2I_9$. *J. Mater. Chem. A* **4** (2016) 12504–12515. doi:10.1039/C6TA04657F

[90] S. E. Creutz, H. Liu, M. E. Kaiser, X. Li, and D. R. Gamelin. Structural Diversity in Cesium-Bismuth-Halide Nanocrystals. *Chem. Mater.* **31** (2019) 4685–4697. doi:10.1021/acs.chemmater.9b00640

[91] A. J. Lehner, H. Wang, D. H. Fabini, C. D. Liman, C.-A. Hébert, E. E. Perry, M. Wang, G. C. Bazan, M. L. Chabinyc, and R. Seshadri. Electronic Structure and Photovoltaic Application of BiI_3. *Appl. Phys. Lett.* **107** (2015) 131109. doi:10.1063/1.4932129

[92] A. J. Lehner, D. H. Fabini, H. A. Evans, C.-A. Hébert, S. R. Smock, J. Hu, H. Wang, J. W. Zwanziger, M. L. Chabinyc, and R. Seshadri. Crystal and Electronic Structures of Complex Bismuth Iodides $A_3Bi_2I_9$ (A = K, Rb, Cs) Related to Perovskite: Aiding the Rational Design of Photovoltaics. *Chem. Mater.* **27** (2015) 7137–7148. doi:10.1021/acs.chemmater.5b03147

[93] Y. Lou, M. Fang, J. Chen, and Y. Zhao. Formation of Highly Luminescent Cesium Bismuth Halide Perovskite Quantum Dots Tuned by Anion Exchange. *Chem. Comm.* **54** (2018) 3779–3782. doi:10.1039/C8CC01110A

[94] M. Leng, Y. Yang, K. Zeng, Z. Chen, Z. Tan, S. Li, J. Li, B. Xu, D. Li, M. P. Hautzinger, Y. Fu, T. Zhai, L. Xu, G. Niu, S. Jin, and J. Tang. All-Inorganic Bismuth-Based Perovskite Quantum Dots with Bright Blue Photoluminescence and Excellent Stability. *Adv. Funct. Mater.* **28** (2018) 1704446. doi:10.1002/adfm.201704446

[95] S. M. Jain, D. Phuyal, M. L. Davies, M. Li, B. Philippe, C. De Castro, Z. Qiu, J. Kim, T. Watson, W. C. Tsoi, O. Karis, H. Rensmo, G. Boschloo, T. Edvinsson, and J. R. Durrant. An Effective Approach of Vapour Assisted Morphological Tailoring for Reducing Metal Defect Sites in Lead-Free, $(CH_3NH_3)_3Bi_2I_9$ Bismuth-Based Perovskite Solar Cells for Improved Performance and Long-Term Stability. *Nano Energy* **49** (2018) 614–624. doi:10.1016/j.nanoen.2018.05.003

[96] Z. Xiao, W. Meng, J. Wang, D. B. Mitzi, and Y. Yan. Searching for Promising New Perovskite-Based Photovoltaic Absorbers: the Importance of Electronic Dimensionality. *Mater. Horiz.* **4** (2017) 206–216. doi:10.1039/C6MH00519E

[97] K. M. McCall, C. C. Stoumpos, O. Y. Kontsevoi, G. C. Alexander, B. W. Wessels, and M. G. Kanatzidis. From 0D $Cs_3Bi_2I_9$ to 2D $Cs_3Bi_2I_6Cl_3$: Dimensional Expansion Induces a Direct Band Gap but Enhances Electron–Phonon Coupling. *Chem. Mater.* **31** (2019) 2644–2650. doi:10.1021/acs.chemmater.9b00636

[98] O. V. Dolomanov, L. J. Bourhis, R. J. Gildea, J. A. K. Howard, and H. Puschmann. OLEX2: A Complete Structure Solution, Refinement and Analysis Program. *J. Appl. Crystallogr.* **42** (2009) 339–341. doi:10.1107/S0021889808042726

[99] K. Momma and F. Izumi. VESTA 3 for Three-Dimensional Visualization of Crystal, Volumetric and Morphology Data. *J. Appl. Crystallogr.* **44** (2011) 1272–1276. doi:10.1107/S0021889811038970

[100] G. Kresse and D. Joubert. From Ultrasoft Pseudopotentials to the Projector Augmented-Wave Method. *Phys. Rev. B* **59** (1999) 1758–1775. doi:10.1103/PhysRevB.59.1758

[101] J. Heyd, G. E. Scuseria, and M. Ernzerhof. Erratum: "Hybrid functionals based on a screened Coulomb potential" [J. Chem. Phys. 118, 8207 (2003)]. *J. Chem. Phys.* **124** (2006) 219906. doi:10.1063/1.2204597

[102] G. Meyer and A. Schönemund. Zur Kenntnis der Hochtemperatur-Phasenumwandlug bei $Cs_3Bi_2Cl_9$. *Z. Anor. Allg. Chem.* **468** (1980) 185–192. doi:10.1002/zaac.19804680123

[103] F. Benachenhou, G. Mairesse, G. Nowogrocki, and D. Thomas. Structural Studies of Cs–K–Bi Mixed Chlorides Relation to the Crystal Structures of A_2BMX_6, A_3MX_6, and A_2MX_6. *J. Solid State Chem.* **65** (1986) 13–26.

[104] A. Arakcheeva, M. Novikova, A. Zaitsev, and G. Lubman. Perovskite-like Modification of $Cs_3Sb_2I_9$ as a Member of the OD family $A_3B_2X_9$. *J. Struct. Chem.* **40** (1999) 572–579.

[105] K. Dornberger-Schiff and H. Grell-Niemann. On the Theory of Order–Disorder (OD) Structures. *Acta Crystallogr.* **14** (1961) 167–177.

[106] L. Mao, S. M. L. Teicher, C. C. Stoumpos, R. M. Kennard, R. A. DeCrescent, G. Wu, J. A. Schuller, M. L. Chabinyc, A. K. Cheetham, and R. Seshadri. Chemical and Structural Diversity of Hybrid Layered Double Perovskite Halides. *J. Am. Chem. Soc.* (2019). doi:10.1021/jacs.9b09945

[107] E. E. Morgan, G. T. Kent, A. Zohar, A. O'Dea, G. Wu, A. K. Cheetham, and R. Seshadri. Hybrid and Inorganic Vacancy-Ordered Double Perovskites A_2WCl_6. *Chem. Mater.* (2023). doi:10.1021/acs.chemmater.3c01300

[108] J. J. Berzelius. Untersuchung über die Eigenschaften des Tellurs. *Ann. Phys. Chem* **108** (1834) 577.

[109] R. G. Dickinson. The Crystal Structures of Potassium Chloroplatinite and of Potassium and Ammonium Chloropalladites. *J. Am. Chem. Soc.* **44** (1922) 2404–2411.

[110] B. Lee, C. C. Stoumpos, N. Zhou, F. Hao, C. Malliakas, C.-Y. Yeh, T. J. Marks, M. G. Kanatzidis, and R. P. H. Chang. Air-Stable Molecular Semiconducting Iodosalts for Solar Cell Applications: Cs_2SnI_6 as a Hole Conductor. *J. Am. Chem. Soc.* **136** (2014) 15379–15385. doi:10.1021/ja508464w

[111] A. E. Maughan, A. M. Ganose, M. M. Bordelon, E. M. Miller, D. O. Scanlon, and J. R. Neilson. Defect Tolerance to Intolerance in the Vacancy-Ordered Double Perovskite Semiconductors Cs_2SnI_6 and Cs_2TeI_6. *J. Am. Chem. Soc.* **138** (2016) 8453–8464. doi:10.1021/jacs.6b03207

[112] H. A. Evans, D. H. Fabini, J. L. Andrews, M. Koerner, M. B. Preefer, G. Wu, F. Wudl, A. K. Cheetham, and R. Seshadri. Hydrogen Bonding Controls the Structural Evolution in Perovskite-Related Hybrid Platinum(IV) Iodides. *Inorg. Chem.* **57** (2018) 10375–10382.

[113] I. Vázquez-Fernández, S. Mariotti, O. S. Hutter, M. Birkett, T. D. Veal, T. D. C. Hobson, L. J. Phillips, L. Danos, P. K. Nayak, H. J. Snaith, W. Xie, M. P. Sherburne, M. Asta, and K. Durose. Vacancy-Ordered Double Perovskite Cs_2TeI_6 Thin Films for Optoelectronics. *Chem. Mater.* **32** (2020) 6676–6684. doi:10.1021/acs.chemmater.0c02150

[114] Y. Cai, W. Xie, H. Ding, Y. Chen, K. Thirumal, L. H. Wong, N. Mathews, S. G. Mhaisalkar, M. Sherburne, and M. Asta. Computational Study of Halide Perovskite-Derived A_2BX_6 Inorganic Compounds: Chemical Trends in Electronic Structure and Structural Stability. *Chem. Mater.* **29** (2017) 7740–7749. doi:10.1021/acs.chemmater.7b02013

[115] Z.-Y. Wang, Y. Chen, C. Zhang, D. Wang, P. Liang, H. Zhang, R.-J. Xie, and L. Wang. Electronic Structure and Optical Properties of Vacancy-Ordered Double Perovskites $Cs_2PdBr_xCl_{6-x}$ by First-Principles Calculation. *J. Phys. Chem. C* **124** (2020) 13310–13315. doi:10.1021/acs.jpcc.0c00137

[116] M. Faizan, S. H. Khan, G. Murtaza, A. Khan, and A. Laref. Electronic and Magnetic Properties of Alkali Metal Chlorides A_2MCl_6 (A = K, Rb, Cs; M = Mn, Mo): A Density Functional Theory Study. *Int. J. Mod. Phys. B* **33** (2019) 1950072. doi:10.1142/S0217979219500723

[117] M. Faizan, K. C. Bhamu, G. Murtaza, X. He, N. Kulhari, M. M. AL-Anazy, and S. H. Khan. Electronic and Optical Properties of Vacancy Ordered Double Perovskites A_2BX_6 (A = Rb, Cs; B = Sn, Pd, Pt; and X = Cl, Br, I): a First Principles Study. *Sci. Rep.* **11** (2021) 6965. doi:10.1038/s41598-021-86145-x

[118] J. K. Burdett and T. Hughbanks. Aspects of Metal-Metal Bonding in Early-Transition-Metal Dioxides. *Inorg. Chem.* **24** (1985) 1741–1750.

[119] H. Ishikawa, T. Yajima, A. Matsuo, and K. Kindo. Ligand Dependent Magnetism of the J_{eff} = 3/2 Mott Insulator Cs_2MX_6 (M = Ta, Nb, X = Br, Cl). *J. Phys.: Condens. Matter* **33** (2021) 125802. doi:10.1088/1361-648X/abd7b5

[120] H. Ishikawa, T. Takayama, R. K. Kremer, J. Nuss, R. Dinnebier, K. Kitagawa, K. Ishii, and H. Takagi. Ordering of hidden multipoles in spin-orbit entangled $5d^1$ Ta chlorides. *Phys. Rev. B* **100** (2019) 045142. doi:10.1103/PhysRevB.100.045142

[121] A. Mansouri Tehrani, J.-R. Soh, J. Pásztorová, M. E. Merkel, I. Živković, H. M. Rønnow, and N. A. Spaldin. Charge Multipole Correlations and Order in Cs_2TaCl_6. *Phys. Rev. Res.* **5** (2023) L012010. doi:10.1103/PhysRevResearch.5.L012010

[122] P. Vishnoi, J. L. Zuo, J. A. Cooley, L. Kautzsch, A. Gómez-Torres, J. Murillo, S. Fortier, S. D. Wilson, R. Seshadri, and A. K. Cheetham. Chemical Control of Spin-Orbit Coupling and Charge Transfer in Vacancy-Ordered Ruthenium(IV) Halide Perovskites. *Angew. Chem.* **133** (2021) 5244–5248. doi:https://doi.org/10.1002/ange.202013383

[123] C. Kennedy and R. Peacock. Complex Chlorides and Bromides of Quadrivalent Tungsten. *J. Chem. Soc.* (1963) 3392–3397. doi:10.1039/JR9630003392

[124] P. Wang, W. Xu, and Y.-Q. Zheng. Crystal Structure of Dicaesium Hexachlorotungstate(IV), $Cs_2[WCl_6]$. *Z. Kristallogr. NCS* **218** (2003) 25–25. doi:10.1524/ncrs.2003.218.1.25

[125] J. E. Fergusson, A. M. Greenaway, and B. R. Penfold. Preparative and structural studies of pentahalogeno-oxometallate(V) salts of the transition metals Cr, Mo, W, Tc, Re. *Inorg. Chim. Acta* **71** (1983) 29–34. doi:10.1016/S0020-1693(00)83634-8

[126] G. Parkin. Bond-Stretch Isomerism in Transition Metal Complexes: a Reevaluation of Crystallographic Data. *Chem. Rev.* **93** (1993) 887–911. doi:10.1021/cr00019a003

[127] H. B. Gray and C. R. Hare. The Electronic Structures and Spectra of Chromyl and Molybdenyl Ions. *Inorg. Chem.* **1** (1962) 363–368. doi:10.1021/ic50002a034

[128] C. R. Hare, I. Bernal, and H. B. Gray. The Electronic Structures and Magnetic Properties of the Chromyl and Molybdenyl Ions. *Inorg. Chem.* **1** (1962) 831–835. doi:10.1021/ic50004a023

[129] J. Bendix, M. Brorson, and C. E. Schaffer. Accurate Empirical Spin-Orbit Coupling Parameters ζ_{nd} for Gaseous nd^q Transition Metal Ions. The Parametrical Multiplet Term Model. *Inorg. Chem.* **32** (1993) 2838–2849. doi:10.1021/ic00065a010

[130] A. M. Greenaway. *Vibrational Studies of $(MLX_5)^{n-}$ Type Compounds*. Dissertation, University of Canterbury, Christchurch, New Zealand (1976).

[131] E. A. Allen, B. J. Brisdon, D. A. Edwards, G. W. A. Fowles, and R. G. Williams. 890. Halide and Oxyhalide Complexes of Molybdenum and Tungsten. *J. Chem. Soc.* (1963) 4649. doi:10.1039/jr9630004649

[132] D. Brown. 950. Some Oxychloro-Complexes of Quinquevalent Elements. *J. Chem. Soc.* (1964) 4944. doi:10.1039/jr9640004944

[133] A. M. Srivastava and J. F. Ackerman. Synthesis and Luminescence Properties of Cs_2NbOF_5 and Cs_2NbOCl_5 with Isolated $[NbOX_5]^{-2}$ (X = F^-, Cl^-) Octahedra. *Mater. Res. Bull.* **26** (1991) 443–448. doi:10.1016/0025-5408(91)90183-M

[134] D. R. Gamelin and H. U. Güdel. Spectroscopy and Dynamics of Re^{4+} Near-IR-to-Visible Luminescence Upconversion. *Inorg. Chem.* **38** (1999) 5154–5164. doi:10.1021/ic990556r

[135] J. Sun, W. Zheng, P. Huang, M. Zhang, W. Zhang, Z. Deng, S. Yu, M. Jin, and X. Chen. Efficient Near-Infrared Luminescence in Lanthanide-Doped Vacancy-Ordered Double Perovskite Cs_2ZrCl_6 Phosphors via Te^{4+} Sensitization. *Angew. Chem. Int. Ed.* **61** (2022) e202201993. doi:10.1002/anie.202201993

[136] Z. Tan, J. Li, C. Zhang, Z. Li, Q. Hu, Z. Xiao, T. Kamiya, H. Hosono, G. Niu, E. Lifshitz, Y. Cheng, and J. Tang. Highly Efficient Blue-Emitting Bi-Doped Cs_2SnCl_6 Perovskite Variant: Photoluminescence Induced by Impurity Doping. *Adv. Funct. Mater.* **28** (2018) 1801131. doi:10.1002/adfm.201801131

[137] W. Zhang, W. Zheng, L. Li, P. Huang, Z. Gong, Z. Zhou, J. Sun, Y. Yu, and X. Chen. Dual-Band-Tunable White-Light Emission from Bi^{3+}/Te^{4+} Emitters in Perovskite-Derivative Cs_2SnCl_6 Microcrystals. *Angew. Chem. Int. Ed.* **61** (2022) e202116085. doi:10.1002/anie.202116085

[138] Y. Wei, P. Dang, Z. Dai, G. Li, and J. Lin. Advances in Near-Infrared Luminescent Materials Without Cr^{3+}: Crystal Structure Design, Luminescence Properties, and Applications. *Chem. Mater.* **33** (2021) 5496–5526. doi:10.1021/acs.chemmater.1c01325

[139] M. Wojdyr. Fityk: A General-Purpose Peak Fitting Program. *J. Appl. Cryst.* **43** (2010) 1126–1128. doi:10.1107/S0021889810030499

[140] M. C. Folgueras, J. Jin, M. Gao, L. N. Quan, J. A. Steele, S. Srivastava, M. B. Ross, R. Zhang, F. Seeler, K. Schierle-Arndt, M. Asta, and P. Yang. Lattice Dynamics and Optoelectronic Properties of Vacancy-Ordered Double Perovskite Cs_2TeX_6 (X = Cl–, Br–, I–) Single Crystals. *J. Phys. Chem. C* **125** (2021) 25126–25139. doi:10.1021/acs.jpcc.1c08332

[141] W. P. Griffith. Oxy-complexes and their Vibrational Spectra. *J. Chem. Soc. A* (1969) 211–218. doi:10.1039/J19690000211

[142] R. Wernicke, H. Kupka, W. Ensslin, and H.-H. Schmidtke. Low temperature luminescence spectra of the $d^{10}s^2$ complexes Cs_2MX_6 (M = Se, Te and X = Cl, Br). The Jahn—Teller effect in the Γ_4^- ($^3T_{1u}$) excited state. *Chem. Phys.* **47** (1980) 235–244. doi:10.1016/0301-0104(80)85009-9

[143] M. D. Hill, D. B. Cruickshank, and I. A. MacFarlane. Perspective on Ceramic Materials for 5G wireless Communication Systems. *Appl. Phys. Lett.* **118** (2021) 120501. doi:10.1063/5.0036058

[144] Y. Zhou. Material Foundation for Future 5G Technology. *Acc. Mater. Res.* **2** (2021) 306–310. doi:10.1021/accountsmr.0c00087

[145] D. Shamiryan, T. Abell, F. Iacopi, and K. Maex. Low-k Dielectric Materials. *Mater. Today* **7** (2004) 34–39. doi:10.1016/S1369-7021(04)00053-7

[146] H. J. Wang, X. Q. Sun, and J. J. Bian. Preparation, Phase Assemblage and Microwave Dielectric Properties of $AlPO_4$-BPO_4-SiO_2 Ternaries. *J. Eur. Ceram. Soc.* **41** (2021) 3438–3444. doi:10.1016/j.jeurceramsoc.2021.01.034

[147] M. Morgen, E. T. Ryan, J.-H. Zhao, C. Hu, T. Cho, and P. S. Ho. Low Dielectric Constant Materials for ULSI Interconnects. *Annu. Rev. Mater. Sci.* **30** (2000) 645–680. doi:10.1146/annurev.matsci.30.1.645

[148] P. A. Kohl. Low–Dielectric Constant Insulators for Future Integrated Circuits and Packages. *Annu. Rev. Chem. Biomol. Eng.* **2** (2011) 379–401. doi:10.1146/annurev-chembioeng-061010-114137

[149] W. Volksen, R. D. Miller, and G. Dubois. Low Dielectric Constant Materials. *Chem. Rev.* **110** (2010) 56–110. doi:10.1021/cr9002819

[150] W. Lou, M. Mao, K. Song, K. Xu, B. Liu, W. Li, B. Yang, Z. Qi, J. Zhao, S. Sun, H. Lin, Y. Hu, D. Zhou, D. Wang, and I. M. Reaney. Low Permittivity Cordierite-Based Microwave Dielectric Ceramics for 5G/6G Telecommunications. *J. Eur. Ceram. Soc.* **42** (2022) 2820–2826. doi:10.1016/j.jeurceramsoc.2022.01.050

[151] H. Ohsato, I. Kagomiya, M. Terada, and K. Kakimoto. Origin of Improvement of Q Based on High Symmetry Accompanying Si–Al Disordering in Cordierite Millimeter-Wave Ceramics. *J. Eur. Ceram. Soc.* **30** (2010) 315–318. doi:10.1016/j.jeurceramsoc.2009.05.024

[152] H. Ohsato, J. Varghese, T. Vahera, J. S. Kim, M. T. Sebastian, H. Jantunen, M. Iwata, H. Ohsato, J. Varghese, T. Vahera, J. S. Kim, M. T. Sebastian, H. Janntunen, and M. Iwata. Micro/Millimeter-Wave Dielectric Indialite/Cordierite Glass-Ceramics Applied as LTCC and Direct Casting Substrates: Current Status and Prospects. *J. Korean Ceram. Soc* **56** (2019) 526–533. doi:10.4191/kcers.2019.56.6.01

[153] P. Kumari, P. Tripathi, O. Parkash, and D. Kumar. Low Temperature Sintering and Characterization of MgO-B_2O_3-SiO_2 Glass-Ceramics for LTCC Substrate Applications. *Trans. Indian Ceram. Soc.* **75** (2016) 229–233. doi:10.1080/0371750X.2016.1210025

[154] U. Došler, M. M. Kržmanc, and D. Suvorov. The Synthesis and Microwave Dielectric Properties of $Mg_3B_2O_6$ and $Mg_2B_2O_5$ Ceramics. *J. Eur. Ceram. Soc.* **30** (2010) 413–418. doi:10.1016/j.jeurceramsoc.2009.05.049

[155] W. B. Hong, L. Li, H. Yan, S. Y. Wu, H. S. Yang, and X. M. Chen. Room-Temperature-Densified H_3BO_3 Microwave Dielectric Ceramics With Ultra-Low Permittivity and Ultra-High Qf Value. *J. Materiomics* **6** (2020) 233–239. doi:10.1016/j.jmat.2020.02.006

[156] H. Ling, M. Acharya, L. W. Martin, and K. A. Persson. Theory-Guided Exploration of the $Sr_2Nb_2O_7$ System for Increased Dielectric and Piezoelectric Properties and Synthesis of Vanadium-Alloyed $Sr_2Nb_2O_7$. *Chem. Mater.* **34** (2022) 8536–8543.

[157] F. Wu, D. Zhou, C. Du, D.-M. Xu, R.-T. Li, Z.-Q. Shi, M. A. Darwish, T. Zhou, and H. Jantunen. Design and Fabrication of a Satellite Communication Dielectric Resonator Antenna with Novel Low Loss and Temperature-Stabilized $(Sm_{1-x}Ca_x)(Nbi_{1-x}Mo_x)O_4$ ($x = 0.15 – 0.7$) Microwave Ceramics. *Chem. Mater.* **35** (2022) 104–115.

[158] J. Ma, J. Zhang, J. Guo, X. Li, S. Guo, Y. Huan, J. Wang, S.-T. Zhang, and Y. Wang. Achieving Ultrahigh Energy Storage Density in Lead-Free Sodium Niobate-Based Ceramics by Modulating the Antiferroelectric Phase. *Chem. Mater.* **34** (2022) 7313–7322.

[159] M. Acharya, H. Ling, D. Lou, M. Ramesh, B. Hanrahan, G. Velarde, M. Asta, K. Persson, and L. W. Martin. Exploring the Morphotropic Phase Boundary in Epitaxial $PbHf_{1-x}Ti_xO_3$ Thin Films. *Chem. Mater.* **34** (2022) 9613–9623.

[160] S. Li, Y. Wang, M. Yang, S. Xu, M. Liu, Q. Li, J. Miao, E.-J. Guo, K. Jin, L. Gu, Q. Zhang, J. Deng, X. Chen, and X. Xing. Ferroelectricity in Low-Permittivity $SrZrO_3$ Epitaxial Films. *Chem. Mater.* **35** (2023) 2967–2974.

[161] Y. Lee, K. Kim, Z. Lee, H.-S. Lee, H.-B.-R. Lee, W.-H. Kim, I.-K. Oh, and H. Kim. Dysprosium Incorporation for Phase Stabilization of Atomic-Layer-Deposited HfO_2 Thin Films. *Chem. Mater.* **35** (2023) 2312–2320.

[162] I. B. Bersuker. Jahn–Teller and Pseudo-Jahn–Teller Effects: From Particular Features to General Tools in Exploring Molecular and Solid State Properties. *Chem. Rev.* **121** (2020) 1463–1512.

[163] G. Laurita and R. Seshadri. Chemistry, Structure, and Function of Lone Pairs in Extended Solids. *Acc. Chem. Res.* **55** (2022) 1004–1014.

[164] P. M. Woodward, P. Karen, J. S. Evans, and T. Vogt. *Solid State Materials Chemistry*. Cambridge University Press (2021).

[165] R. D. Shannon. Dielectric Polarizabilities of Ions in Oxides and Fluorides. *J. Appl. Phys.* **73** (1993) 348–366. doi:10.1063/1.353856

[166] H. A. Evans, D. Mullangi, Z. Deng, Y. Wang, S. B. Peh, F. Wei, J. Wang, C. M. Brown, D. Zhao, P. Canepa, and A. K. Cheetham. Aluminum Formate, $Al(HCOO)_3$: An Earth-Abundant, Scalable, and Highly Selective Material for CO_2 Capture. *Sci. Adv.* **8** (2022) eade1473. doi:10.1126/sciadv.ade1473

[167] D. Mullangi, H. A. Evans, T. Yildirim, Y. Wang, Z. Deng, Z. Zhang, T. T. Mai, F. Wei, J. Wang, A. R. Hight Walker, C. M. Brown, D. Zhao, P. Canepa, and A. K. Cheetham. Noncryogenic Air Separation Using Aluminum Formate $Al(HCOO)_3$ (ALF). *J. Am. Chem. Soc.* **145** (2023) 9850–9856. doi:10.1021/jacs.3c02100

[168] Z. Zhang, Z. Deng, H. A. Evans, D. Mullangi, C. Kang, S. B. Peh, Y. Wang, C. M. Brown, J. Wang, P. Canepa, A. K. Cheetham, and D. Zhao. Exclusive Recognition of CO_2 from Hydrocarbons by Aluminum Formate with Hydrogen-Confined Pore Cavities. *J. Am. Chem. Soc.* **145** (2023) 11643–11649. doi:10.1021/jacs.3c01705

[169] H. J. Monkhorst and J. D. Pack. Special Points for Brillouin-zone Integrations. *Phys. Rev. B* **13** (1976) 5188–5192.

[170] I. Petousis, W. Chen, G. Hautier, T. Graf, T. D. Schladt, K. A. Persson, and F. B. Prinz. Benchmarking Density Functional Perturbation Theory to Enable High-Throughput Screening of Materials for Dielectric Constant and Refractive Index. *Phys. Rev. B* **93** (2016) 115151. doi:10.1103/PhysRevB.93.115151

[171] Z. Hashin and S. Shtrikman. Conductivity of Polycrystals. *Phys. Rev.* **130** (1963) 129–133. doi:10.1103/PhysRev.130.129

[172] Y.-Q. Tian, Y.-M. Zhao, H.-J. Xu, and C.-Y. Chi. CO_2 Template Synthesis of Metal Formates with a ReO_3 Net. *Inorg. Chem.* **46** (2007) 1612–1616. doi:10.1021/ic0617240

[173] R. Tempke, C. Wildfire, D. Shekhawat, and T. Musho. Dielectric Measurement of Powdery Materials Using a Coaxial Transmission Line. *IET Sci., Meas. Technol.* **14** (2020) 972–978. doi:10.1049/iet-smt.2020.0055

[174] J. Krupka, R. Clarke, O. Rochard, and A. Gregory. Split Post Dielectric Resonator Technique for Precise Measurements of Laminar Dielectric Specimens-Measurement Uncertainties. In *13th International Conference on Microwaves, Radar and Wireless Communications*, volume 1 (2000) pages 305–308.

[175] H. Looyenga. Dielectric Constants of Heterogeneous Mixtures. *Physica* **31** (1965) 401–406. doi:10.1016/0031-8914(65)90045-5

[176] C. Xie, A. R. Oganov, D. Dong, N. Liu, D. Li, and T. T. Debela. Rational Design of Inorganic Dielectric Materials with Expected Permittivity. *Sci. Rep.* **5** (2015) 16769. doi:10.1038/srep16769

[177] A. Takahashi, Y. Kumagai, J. Miyamoto, Y. Mochizuki, and F. Oba. Machine Learning Models for Predicting the Dielectric Constants of Oxides Based on High-Throughput First-Principles Calculations. *Phys. Rev. Mater.* **4** (2020) 103801. doi:10.1103/PhysRevMaterials.4.103801

[178] R. E. Newnham. *Properties of Materials: Anisotropy, Symmetry, Structure*. Oxford University Press (2005).

[179] M. Hellenbrandt. The Inorganic Crystal Structure Database (ICSD) – Present and Future. *Crystallogr. Rev.* **10** (2004) 17–22.

[180] A. Jain, S. P. Ong, G. Hautier, W. Chen, W. D. Richards, S. Dacek, S. Cholia, D. Gunter, D. Skinner, G. Ceder, and K. A. Persson. Commentary: The Materials Project: A Materials Genome Approach to Accelerating Materials Innovation. *APL Mater.* **1** (2013) 011002. doi:10.1063/1.4812323

[181] S. Grimme, J. Antony, S. Ehrlich, and H. Krieg. A Consistent and Accurate Ab Initio Parametrization of Density Functional Dispersion Correction (DFT-D) for the 94 elements H-Pu. *J. Chem. Phys.* **132** (2010) 154104. doi:10.1063/1.3382344

[182] S. Grimme, S. Ehrlich, and L. Goerigk. Effect of the Damping Function in Dispersion Corrected Density Functional Theory. *J. Comput. Chem.* **32** (2011) 1456–1465. doi:10.1002/jcc.21759

[183] E. E. Morgan, H. A. Evans, K. Pilar, C. M. Brown, R. Clément, R. Maezono, R. Seshadri, B. Monserrat, and A. K. Cheetham. Lattice Dynamics in the NASICON $NaZr_2(PO_4)_3$ Solid Electrolyte from Temperature-Dependent Neutron Diffraction, NMR, and Ab Initio Computational Studies. *Chem. Mater.* **34** (2022) 4029–4038. doi:10.1021/acs.chemmater.2c00212

[184] L.-O. Hagman and P. Kierkegaard. The Crystal Structure of $NaMe_2(PO_4)_3$; Me=Ge, Ti, Zr. *Acta Chem. Scand.* **22** (1968) 1822–1832. doi:10.3891/acta.chem.scand.22-1822

[185] J. B. Goodenough, H.-P. Hong, and J. Kafalas. Fast Na^+-Ion Transport in Skeleton Structures. *Mater. Res. Bull.* **11** (1976) 203–220. doi:10.1016/0025-5408(76)90077-5

[186] H.-P. Hong. Crystal Structures and Crystal Chemistry in the System $Na_{1+x}Zr_2Si_xP_{3-x}O_{12}$. *Mater. Res. Bull.* **11** (1976) 173–182. doi:10.1016/0025-5408(76)90073-8

[187] J. Alamo and R. Roy. Ultralow-Expansion Ceramics in the System Na_2O-$ZrO_2P_2O_5$-SiO_2. *J. Am. Ceram. Soc.* **67** (1984) c78–c80. doi:https://doi.org/10.1111/j.1151-2916.1984.tb19516.x

[188] C. Masquelier and L. Croguennec. Polyanionic (Phosphates, Silicates, Sulfates) Frameworks as Electrode Materials for Rechargeable Li (or Na) Batteries. *Chem. Rev.* **113** (2013) 6552–6591. doi:10.1021/cr3001862

[189] Z. Jian, Y.-S. Hu, X. Ji, and W. Chen. NASICON-Structured Materials for Energy Storage. *Adv. Mater.* **29** (2017) 1601925. doi:10.1002/adma.201601925

[190] S. Chen, C. Wu, L. Shen, C. Zhu, Y. Huang, K. Xi, J. Maier, and Y. Yu. Challenges and Perspectives for NASICON-Type Electrode Materials for Advanced Sodium-Ion Batteries. *Adv. Mater.* **29** (2017) 1700431. doi:10.1002/adma.201700431

[191] B. Scheetz, D. K. Agrawal, E. Breval, and R. Roy. Sodium Zirconium Phosphate (NZP) as a Host Structure for Nuclear Waste Immobilization: A Review. *Waste Managememt* **14** (1994) 489–505. doi:10.1016/0956-053X(94)90133-3

[192] Z. Deng, G. Sai Gautam, S. K. Kolli, J.-N. Chotard, A. K. Cheetham, C. Masquelier, and P. Canepa. Phase Behavior in Rhombohedral NASICON Electrolytes and Electrodes. *Chem. Mater.* **32** (2020) 7908–7920. doi:10.1021/acs.chemmater.0c02695

[193] B. Singh, Z. Wang, S. Park, G. Sai Gautam, J.-N. Chotard, L. Croguennec, D. Carlier, A. K. Cheetham, C. Masquelier, and P. Canepa. A Chemical Map of NASICON Electrode Materials for Sodium-Ion Batteries. *J. Mater. Chem. A* **9** (2021) 281–292. doi:10.1039/D0TA10688G

[194] X. Guo, Z. Wang, Z. Deng, B. Wang, X. Chen, and S. P. Ong. Design Principles for Aqueous Na-Ion Battery Cathodes. *Chem. Mater.* **32** (2020) 6875–6885. doi:10.1021/acs.chemmater.0c01582

[195] D. T. Qui, J. J. Capponi, J. C. Joubert, and R. D. Shannon. Crystal Structure and Ionic Conductivity in $Na_4Zr_2Si_3O_{12}$. *J. Solid State Chem.* **39** (1981) 219–229. doi:10.1016/0022-4596(81)90335-2

[196] H. Gao, I. D. Seymour, S. Xin, L. Xue, G. Henkelman, and J. B. Goodenough. $Na_3MnZr(PO_4)_3$: A High-Voltage Cathode for Sodium Batteries. *J. Am. Chem. Soc.* **140** (2018) 18192–18199. doi:10.1021/jacs.8b11388

[197] P. Senguttuvan, G. Rousse, M. E. Arroyo y de Dompablo, H. Vezin, J.-M. Tarascon, and M. R. Palacín. Low-Potential Sodium Insertion in a NASICON-Type Structure through the Ti(III)/Ti(II) Redox Couple. *J. Am. Chem. Soc.* **135** (2013) 3897–3903. doi:10.1021/ja311044t

[198] N. Wu, P.-H. Chien, Y. Li, A. Dolocan, H. Xu, B. Xu, N. S. Grundish, H. Jin, Y.-Y. Hu, and J. B. Goodenough. Fast Li^+ Conduction Mechanism and Interfacial Chemistry of a NASICON/Polymer Composite Electrolyte. *J. Am. Chem. Soc.* **142** (2020) 2497–2505. doi:10.1021/jacs.9b12233

[199] J. Zhu, J. Zhao, Y. Xiang, M. Lin, H. Wang, B. Zheng, H. He, Q. Wu, J. Y. Huang, and Y. Yang. Chemomechanical Failure Mechanism Study in NASICON-Type $Li_{1.3}Al_{0.3}Ti_{1.7}(PO_4)_3$ Solid-State Lithium Batteries. *Chem. Mater.* **32** (2020) 4998–5008. doi:10.1021/acs.chemmater.9b05295

[200] B. Jeon, J. W. Heo, J. Hyoung, H. H. Kwak, D. M. Lee, and S.-T. Hong. Reversible Calcium-Ion Insertion in NASICON-Type $NaV_2(PO_4)_3$. *Chem. Mater.* **32** (2020) 8772–8780.

[201] J. S. Ko, P. P. Paul, G. Wan, N. Seitzman, R. H. DeBlock, B. S. Dunn, M. F. Toney, and J. N. Weker. NASICON $Na_3V_2(PO_4)_3$ Enables Quasi-Two-Stage Na^+ and Zn^{2+} Intercalation for Multivalent Zinc Batteries. *Chem. Mater.* **32** (2020) 3028–3035. doi:10.1021/acs.chemmater.0c00004

[202] T.-U. Wi, C. Lee, M. F. Rahman, W. Go, S. H. Kim, D. Y. Hwang, S. K. Kwak, Y. Kim, and H.-W. Lee. Chemical Stability and Degradation Mechanism of Solid Electrolytes/Aqueous Media at a Steady State for Long-Lasting Sodium Batteries. *Chem. Mater.* **33** (2021) 126–135. doi:10.1021/acs.chemmater.0c03022

[203] M. A. Pogosova, I. V. Krasnikova, A. O. Sanin, S. A. Lipovskikh, A. A. Eliseev, A. V. Sergeev, and K. J. Stevenson. Complex Investigation of Water Impact on Li-Ion Conductivity of $Li_{1.3}Al_{0.3}Ti_{1.7}(PO_4)_3$—Electrochemical, Chemical, Structural, and Morphological Aspects. *Chem. Mater.* **32** (2020) 3723–3732. doi:10.1021/acs.chemmater.9b04419

[204] J. P. Boilot, J. P. Salanié, G. Desplanches, and D. Le Potier. Phase Transformation in $Na_{1+x}Si_xZr_2P_{3-x}O_{12}$ Compounds. *Mater. Res. Bull.* **14** (1979) 1469–1477. doi:10.1016/0025-5408(79)90091-6

[205] J. Alamo and R. Roy. Crystal Chemistry of the $NaZr_2(PO_4)_3$, NZP or CTP, Structure Family. *J. Mater. Sci.* **21** (1986) 444–450. doi:10.1007/BF01145507

[206] G. E. Lenain, H. A. McKinstry, J. Alamo, and D. K. Agrawal. Structural Model for Thermal Expansion in $MZr_2P_3O_{12}$ (M=Li, Na, K, Rb, Cs). *J. Mater. Sci.* **22** (1987) 17–22. doi:10.1007/BF01160546

[207] T. Oota and I. Yamai. Thermal Expansion Behavior of $NaZr_2(PO_4)_3$ Type Compounds. *J. Am. Ceram. Soc.* **69** (1986) 1–6. doi:https://doi.org/10.1111/j.1151-2916.1986.tb04682.x

[208] D. K. Agrawal, C.-Y. Huang, and H. A. McKinstry. NZP: A New Family of Low-Thermal Expansion Materials. *Int. J. Thermophys.* **12** (1991) 697–710. doi:10.1007/BF00534225

[209] R. M. Hazen and L. Finger. High-Temperature Crystal Chemistry of Sodium Zirconium Phosphate (NZP). *J. Mater. Res* **2** (1987) 329–337.

[210] K. G. Kutty, R. Asuvathraman, and R. Sridharan. Thermal Expansion Studies on the Sodium Zirconium Phosphate Family of Compounds $A_{1/2}M_2(PO_4)_3$: Effect of Interstitial and Framework Cations. *J. Mater. Sci.* **33** (1998) 4007–4013. doi:10.1023/A:1004661132398

[211] S. Muy, R. Schlem, Y. Shao-Horn, and W. G. Zeier. Phonon–Ion Interactions: Designing Ion Mobility Based on Lattice Dynamics. *Adv. Energy Mater.* **11** (2021) 2002787. doi:10.1002/aenm.202002787

[212] U. Köhler and C. Herzig. On the Correlation Between Self-diffusion and the Low-Frequency LA $2/3$ $\langle 111 \rangle$ Phonon Mode in B.C.C. Metals. *Philos. Mag. A* **58** (1988) 769–786. doi:10.1080/01418618808209952

[213] K. Wakamura. Roles of Phonon Amplitude and Low-Energy Optical Phonons on Superionic Conduction. *Phys. Rev. B* **56** (1997) 11593–11599. doi:10.1103/PhysRevB.56.11593

[214] X. Li and N. A. Benedek. Enhancement of Ionic Transport in Complex Oxides through Soft Lattice Modes and Epitaxial Strain. *Chem. Mater.* **27** (2015) 2647–2652. doi:10.1021/acs.chemmater.5b00445

[215] Y. Deng, C. Eames, L. H. B. Nguyen, O. Pecher, K. J. Griffith, M. Courty, B. Fleutot, J.-N. Chotard, C. P. Grey, M. S. Islam, and C. Masquelier. Crystal Structures, Local Atomic Environments, and Ion Diffusion Mechanisms of Scandium-Substituted Sodium Superionic Conductor (NASICON) Solid Electrolytes. *Chem. Mater.* **30** (2018) 2618–2630. doi:10.1021/acs.chemmater.7b05237

[216] K. R. Thurber and R. Tycko. Measurement of Sample Temperatures Under Magic-Angle Spinning from the Chemical Shift and Spin-Lattice Relaxation Rate of ^{79}Br in KBr Powder. *J. Magn. Reson.* **196** (2009) 84–87. doi:10.1016/j.jmr.2008.09.019

[217] M. Profeta, C. Pickard, and F. Mauri. Accurate First Principles Prediction of ^{17}O NMR Parameters in SiO_2: Assignment of the Zeolite Ferrierite Spectrum. *J. Am. Chem. Soc.* **125** (2003) 2541–548.

[218] S. J. Clark, M. D. Segall, C. J. Pickard, P. J. Hasnip, M. J. Probert, K. Refson, and M. Payne. First Principles Methods Using CASTEP. *Z. Kristall.* **220** (2005) 567–570.

[219] K. Kunc and R. M. Martin. Ab Initio Force Constants of GaAs: A New Approach to Calculation of Phonons and Dielectric Properties. *Phys. Rev. Lett.* **48** (1982) 406–409. doi:10.1103/PhysRevLett.48.406

[220] J. H. Lloyd-Williams and B. Monserrat. Lattice Dynamics and Electron-Phonon Coupling Calculations Using Nondiagonal Supercells. *Phys. Rev. B* **92** (2015) 184301. doi:10.1103/PhysRevB.92.184301

[221] D. J. Hooton. LI. A New Treatment of Anharmonicity in Lattice Thermodynamics: I. *Phil. Mag. Ser. 7* **46** (1955) 422–432.

[222] D. He, J. Thingna, J.-S. Wang, and B. Li. Quantum Thermal Transport through Anharmonic Systems: A Self-Consistent Approach. *Phys. Rev. B* **94** (2016) 155411. doi:10.1103/PhysRevB.94.155411

[223] B. Monserrat. Vibrational Averages Along Thermal Lines. *Phys. Rev. B* **93** (2016) 014302. doi:10.1103/PhysRevB.93.014302

[224] B. Monserrat. Electron–Phonon Coupling From Finite Differences. *J. Phys.: Condens. Matter* **30** (2018) 083001. doi:10.1088/1361-648X/aaa737

[225] A. Stukowski. Visualization and Analysis of Atomistic Simulation Data with OVITO – The Open Visualization Tool. *Modelling Simul. Mater. Sci. Eng.* **18** (2010). doi:10.1088/0965-0393/18/1/015012

[226] A. K. Cheetham, N. J. Clayden, C. M. Dobson, and R. J. Jakeman. Correlations Between ^{31}P NMR Chemical Shifts and Structural Parameters in Crystalline Inorganic Phosphates. *J. Chem. Soc., Chem. Commun.* (1986) 195–197. doi:10.1039/C39860000195

[227] T. Charpentier, S. Ispas, M. Profeta, F. Mauri, and C. J. Pickard. First-Principles Calculation of ^{17}O, ^{29} Si, and ^{23} Na NMR Spectra of Sodium Silicate Crystals and Glasses. *J. Phys. Chem. B* **108** (2004) 4147–4161. doi:10.1021/jp0367225

[228] F. Vasconcelos, S. Cristol, J.-F. Paul, L. Montagne, F. Mauri, and L. Delevoye. First-Principles Calculations of NMR Parameters for Phosphate Materials. *Magn. Reson. Chem.* **48** (2010) S142–S150. doi:10.1002/mrc.2667

[229] S. E. Ashbrook, L. Le Pollès, R. Gautier, C. J. Pickard, and R. I. Walton. ^{23}Na Multiple-Quantum MAS NMR of the Perovskites $NaNbO_3$ and $NaTaO_3$. *Phys. Chem. Chem. Phys.* **8** (2006) 3423–3431. doi:10.1039/b604520k

[230] F. A. Perras and D. L. Bryce. Multinuclear Magnetic Resonance Crystallographic Structure Refinement and Cross-Validation Using Experimental and Computed Electric Field Gradients: Application to $Na_2Al_2B_2O_7$. *J. Phys. Chem. C* **116** (2012) 19472–19482. doi:10.1021/jp308273h

[231] G. Engelhardt, A. P. M. Kentgens, H. Koller, and A. Samoson. Strategies for Extracting NMR Parameters from ^{23}Na MAS, DOR and MQMAS Spectra. A Case Study for $Na_4P_2O_7$. *Solid State Nucl. Magn. Reson.* **15** (1999) 171–180. doi:10.1016/S0926-2040(99)00054-5

[232] N. I. P. Ayu, E. Kartini, L. D. Prayogi, M. Faisal, and Supardi. Crystal Structure Analysis of Li_3PO_4 Powder Prepared by Wet Chemical Reaction and Solid-State Reaction by Using X-ray Diffraction (XRD). *Ionics* **22** (2016) 1051–1057. doi:10.1007/s11581-016-1643-z

[233] C. Calvo and P. K. L. Au. Crystal Structure of $Cd_2P_2O_7$. *Canadian J. Chem.* **47** (1969) 3409–3416. doi:10.1139/v69-565

[234] B. Dickens, E. Prince, L. W. Schroeder, and W. E. Brown. $Ca(H_2PO_4)_2$, A Crystal Structure Containing Unusual Hydrogen Bonding. *Acta Crystallogr. B* **29** (1973) 2057–2070. doi:10.1107/S0567740873006114

[235] C. Calvo. The Crystal Structure of α-$Zn_3(PO_4)_2$. *Canadian J. Chem.* **43** (1965) 436–445. doi:10.1139/v65-058

[236] K. Y. Leung and C. Calvo. The Structure of $Na_4P_2O_7$ at 22°C. *Canadian J. Chem.* **50** (1972) 2519–2526. doi:10.1139/v72-406

[237] R. J. B. Jakeman and A. K. Cheetham. Combined Single-Crystal X-Ray Diffraction and Magic Angle Spinning NMR Study of α-$CaZn_2(PO_4)_2$. *J. Am. Chem. Soc.* **110** (1988) 1140–1143. doi:10.1021/ja00212a023

[238] M. T. Averbuch-Pouchot and A. Durif. Structure du Monophosphate de Potassium–Zinc: $KZn_4(PO_4)_3$. *Acta Crystallogr. B* **35** (1979) 151–152. doi:10.1107/S0567740879006695

[239] J. S. Stephens and C. Calvo. Crystal Structure of β-$Zn_3(PO_4)_2$. *Canadian J. Chem.* **45** (1967) 2303–2316. doi:10.1139/v67-376

[240] L. W. Schroeder, E. Prince, and B. Dickens. Hydrogen Bonding in $Ca(H_2PO_4)_2.H_2O$ as Determined by Neutron Diffraction. *Acta Crystallogr. B* **31** (1975) 9–12. doi:10.1107/S0567740875002014

[241] N. A. Curry and D. W. Jones. Crystal Structure of Brushite, Calcium Hydrogen Orthophosphate Dihydrate: A Neutron-Diffraction Investigation. *J. Chem. Soc. A* (1971) 3725–3729. doi:10.1039/J19710003725

[242] A. G. Nord. The Cation Distribution in $Zn_2Mg(PO_4)_2$ Determined by X-Ray Profile-Fitting Refinements. *Mater. Res. Bull.* **12** (1977) 563–568.

[243] S. Boudin, A. Grandin, M. M. Borel, A. Leclaire, and B. Raveau. Redetermination of the β-$Ca_2P_2O_7$ Structure. *Acta Crystallogr.* **49** (1993) 2062–2064. doi:10.1107/S0108270193005608

[244] C. Calvo. The Crystal Structure of α-$Ca_2P_2O_7$. *Inorg. Chem.* **7** (1968) 1345–1351. doi:10.1021/ic50065a019

[245] A. G. Nord and P. Kierkegaard. The Crystal Structure of $Mg_3(PO_4)_2$. *Acta Chem. Scand. A* **22** (1968) 1466–1474.

[246] B. E. Robertson and C. Calvo. Crystal Structure of α-$Zn_2P_2O_7$. *J. Solid State Chem.* **1** (1970) 120–133. doi:10.1016/0022-4596(70)90002-2

[247] C. Calvo. The Crystal Structure of α-$Mg_2P_2O_7$. *Acta Crystallogr.* **23** (1967) 289–295. doi:10.1107/S0365110X67002610

[248] J. Alkemper, H. Paulus, and H. Fueß. Crystal Structure of Aluminum Sodium Pyrophosphate. *Z. Kristallogr.* **209** (1994) 616.

[249] K. N. Ng and C. Calvo. The Crystal Structure of $KAlP_2O_7$. *Canadian J. Chem.* **51** (1973) 2613–2620. doi:10.1139/v73-395

[250] L. O. Hagman, I. Jansson, and C. Magnéli. The Crystal Structure of α-$Sr_2P_2O_7$. *Acta Chem. Scand.* **22** (1968) 1419–1429.

[251] A. G. Nord and K. B. Lindberg. The Crystal Structure of Magnesium Tetrametaphosphate, $Mg_2P_4O_{12}$. *Acta Chem. Scand. A* **29** (1975) 1–6. doi:10.3891/acta.chem.scand.29a-0001

[252] B. P. Onac and H. S. Effenberger. Re-examination of Berlinite ($AlPO_4$) from the Cioclovina Cave, Romania. *Am. Mineral.* **92** (2007) 1998–2001. doi:10.2138/am.2007.2581

[253] M. He, X. L. Chen, T. Zhou, B. Q. Hu, Y. P. Xu, and T. Xu. Crystal Structure and Infrared Spectra of $Na_2Al_2B_2O_7$. *Jour. Alloys Compd.* **327** (2001) 210–214. doi:10.1016/S0925-8388(01)01561-4

[254] W. S. McDonald and D. W. J. Cruickshank. A Reinvestigation of the Structure of Sodium Metasilicate, Na_2SiO_3. *Acta Cryst* **22** (1967) 37–43. doi:10.1107/S0365110X67000076

[255] A. K. Pant and D. W. J. Cruickshank. The Crystal Structure of α-$Na_2Si_2O_5$. *Acta Cryst B* **24** (1968) 13–19. doi:10.1107/S0567740868001640

[256] A. K. Pant. A Reconsideration of the Crystal Structure of β-$Na_2Si_2O_5$. *Acta Cryst B* **24** (1968) 1077–1083. doi:10.1107/S0567740868003729

[257] M. Catti and G. Ferraris. Hydrogen Bonding in the Crystalline State. NaH_2PO_4, A Crystal Structure with a Short Symmetrical Hydrogen Bond. *Acta Cryst B* **30** (1974) 1–6. doi:10.1107/S0567740874002111

[258] M. Baldus, B. H. Meier, R. R. Ernst, A. P. M. Kentgens, H. Meyer zu Altenschildesche, and R. Nesper. Structure Investigation on Anhydrous Disodium Hydrogen Phosphate Using Solid-State NMR and X-ray Techniques. *J. Am. Chem. Soc.* **117** (1995) 5141–5147. doi:10.1021/ja00123a017

[259] R. H. Mitchell, P. C. Burns, K. S. Knight, C. J. Howard, and A. R. Chakhmouradian. Observations on the Crystal Structures of Lueshite. *Phys. Chem. Miner.* **41** (2014) 393–401. doi:10.1007/s00269-014-0657-1

[260] R. H. Mitchell and R. P. Liferovich. A Structural Study of the Perovskite Series $Ca_{1-x}Na_xTi_{1-x}Ta_xO_3$. *J. Solid State Chem.* **177** (2004) 4420–4427. doi:10.1016/j.jssc.2004.09.031

[261] K. Selevich, L. Ivashkevich, A. Selevich, and A. Lyakhov. Refinement of Crystal Structure of $Na_2H_2P_2O_7$ Using X-ray Powder Diffraction Data. *Zh. Neorg. Khim.* **47** (2002) 1672–1675.

[262] T. Björkman. CIF2Cell: Generating Geometries for Electronic Structure Programs. *Comput. Phys. Commun.* **182** (2011) 1183–1186. doi:10.1016/j.cpc.2011.01.013

[263] K. Pilar, Z. Deng, M. B. Preefer, J. A. Cooley, R. Clément, R. Seshadri, and A. K. Cheetham. Ab Initio Computation for Solid-State ^{31}P NMR of Inorganic Phosphates: Revisiting X-ray Structures. *Phys. Chem. Chem. Phys.* **21** (2019) 10070–10074. doi:10.1039/C9CP01420A

[264] P. J. Byrne, J. E. Warren, R. E. Morris, and S. E. Ashbrook. Structure and NMR Assignment in $AlPO_4$-15: A Combined Study by Diffraction, MAS NMR and First-Principles Calculations. *Solid State Sci.* **11** (2009) 1001–1006.

[265] S. E. Ashbrook, M. Cutajar, C. J. Pickard, R. I. Walton, and S. Wimperis. Structure and NMR Assignment in Calcined and As-Synthesized Forms of AlPO-14: A Combined Study by First-Principles Calculations and High-Resolution ^{27}Al–^{31}P MAS NMR Correlation. *Phys. Chem. Chem. Phys.* **10** (2008) 5754. doi:10.1039/b805681a

[266] D. M. Dawson, R. F. Moran, S. Sneddon, and S. E. Ashbrook. Is the ^{31}P Chemical Shift Anisotropy of Aluminophosphates a Useful Parameter for NMR Crystallography? *Magn. Reson. Chem.* **57** (2019) 176–190. doi:10.1002/mrc.4788

[267] S. E. Ashbrook and D. McKay. Combining Solid-State NMR Spectroscopy with First-Principles Calculations – A Guide to NMR Crystallography. *Chem. Commun.* **52** (2016) 7186–7204. doi:10.1039/C6CC02542K